

RtEstim: Time-varying reproduction number estimation with trend filtering

Jiapeng Liu^{1*}, Zhenglun Cai², Paul Gustafson¹, Daniel J. McDonald¹

1 Department of Statistics, The University of British Columbia, Vancouver, British Columbia, Canada

2 Centre for Health Evaluation and Outcome Sciences, The University of British Columbia, Vancouver, British Columbia, Canada

* jiapeng.liu@stat.ubc.ca

Abstract

To understand the transmissibility and spread of infectious diseases, epidemiologists turn to estimates of the instantaneous reproduction number. While many estimation approaches exist, their utility may be limited. Challenges of surveillance data collection, model assumptions that are unverifiable with data alone, and computationally inefficient frameworks are critical limitations for many existing approaches. We propose a discrete spline-based approach **RtEstim** that solves a convex optimization problem—Poisson trend filtering—using the proximal Newton method. It produces a locally adaptive estimator for instantaneous reproduction number estimation with heterogeneous smoothness. **RtEstim** remains accurate even under some process misspecifications and is computationally efficient, even for large-scale data. The implementation is easily accessible in a lightweight R package **rtestim**.

Author summary

Effective reproduction number estimation presents many challenges due to data collection, modelling assumptions, and computational burden. Such limitations hinder the accurate estimation of the instantaneous reproduction number. Our motivation is to

develop a model that produces accurate estimates, is robust to model misspecification, and is straightforward to use and computationally efficient, even for large counts and long time periods. We propose a convex optimization model with an ℓ_1 trend filtering penalty. It couples accurate estimation of the instantaneous reproduction number with desired smoothness. We solve the optimization using the proximal Newton method, which converges rapidly and is numerically stable. Our software, conveniently available in the R package `RtEstim`, can produce estimates in seconds for incidence sequences with hundreds of observations. These estimates are produced for a sequence of tuning parameters and can be selected using a built-in cross validation procedure.

1 Introduction

The effective reproduction number (or effective reproductive number) at time t is defined to be the expected number of secondary infections produced by a primary infection throughout the course of the entire infection if conditions remain the same at the specific time. Effective reproduction number is a key quantity for understanding infectious disease dynamics including the potential size of an outbreak and the required stringency of control measures [1, 2]. The instantaneous reproduction number is a type of effective reproduction number focusing on how past infection contribute to the transmission at a specific timepoint; while, the case reproduction number, which is another type of effective reproduction number, focuses on the transmission of the same cohort of individuals with the same date of infection or symptom onset [3]. Tracking the time series of this quantity is useful for understanding whether or not future infections are likely to increase or decrease from the current state [4]. Let $\mathcal{R}(t)$ denote the **instantaneous** reproduction number at time t . Practically, as long as $\mathcal{R}(t) < 1$, infections will decline gradually, eventually resulting in a disease-free equilibrium, whereas when $\mathcal{R}(t) > 1$, infections will continue to increase, resulting in endemic equilibrium. While $\mathcal{R}(t)$ is fundamentally a continuous time quantity, it can be related to data only at discrete points in time $t = 1, \dots, n$. This sequence of instantaneous reproduction numbers over time is not observable, but, nonetheless, is easily interpretable and retrospectively describes the course of an epidemic. Therefore, a number of procedures exist to estimate \mathcal{R}_t from different types of observed incidence

data such as cases, deaths, or hospitalizations, while relying on various domain-specific
assumptions, e.g., [5–8]. Importantly, accurate estimation of instantaneous reproduction
numbers relies heavily on the quality of the available data, and, due to the limitations of
data collection, such as underreporting and lack of standardization, estimation
methodologies rely on various assumptions to compensate. Because model assumptions
may not be easily verifiable from data alone, it is also critical for any estimation
procedure to be robust to model misspecification.

Many existing approaches for instantaneous reproduction number estimation are
Bayesian: they estimate the posterior distribution of \mathcal{R}_t conditional on the observations.
One of the first such approaches is the software **EpiEstim** [9], described by Cori et
al. [10]. This method is prospective, in that it uses only observations available up to
time t in order to estimate \mathcal{R}_t for each $i = 1, \dots, t$. An advantage of **EpiEstim** is its
straightforward statistical model: new incidence data follows the Poisson distribution
conditional on past incidence combined with the conjugate gamma prior distribution for
 \mathcal{R}_t with fixed hyperparameters. Additionally, the serial interval distribution, the
distribution of the period between onsets of primary and secondary infections in a
population, is fixed and known. For this reason, **EpiEstim** requires little domain
expertise for use, and it is computationally fast. Thompson et al. [11] modified this
method to distinguish imported cases from local transmission and simultaneously
estimate the serial interval distribution. Nash et al. [12] further extended **EpiEstim** by
using “reconstructed” daily incidence data to handle irregularly spaced observations.

Recently, Abbott et al. [13] proposed a Bayesian latent variable framework,
EpiNow2 [14], which leverages incident cases, deaths or other available streams
simultaneously along with allowing additional delay distributions (incubation period
and onset to reporting delays) in modelling. Lison et al. [15] proposed an extension that
handles missing data by imputation followed by a truncation adjustment. These
modifications are intended to increase accuracy at the most recent (but most uncertain)
timepoints, to aid policymakers. Parag et al. [16] also proposed a Bayesian approach,
EpiFilter, based on the (discretized) Kalman filter and smoother. **EpiFilter** also
estimates the posterior of \mathcal{R}_t given a Gamma prior and Poisson distributed incident
cases. Compared to **EpiEstim**, however, **EpiFilter** estimates \mathcal{R}_t retrospectively using
all available incidence data both before and after time t , with the goal of being more

robust in low-incidence periods. Gressani et al. [17] proposed a Bayesian P-splines
54 approach, *EpiLPS*, that assumes negative binomial distributed observations. Trevisin et
55 al. [18] also proposed a Bayesian model estimated with particle filtering to incorporate
56 spatial structures. Bayesian approaches estimate the posterior distribution of the
57 instantaneous reproduction numbers and possess the advantage that credible intervals
58 may be easily computed. They also can incorporate prior knowledge on parameters.
59 Another potential advantage is that a relatively large prior on the mean of \mathcal{R}_t can be
60 used to guard against erroneously concluding that an epidemic is shrinking [11].
61 However, a downside is that the induced bias can persist for long periods of time.
62 Bayesian approaches that do not use conjugate priors, or that incorporate multilevel
63 modelling, can be computationally expensive, especially when observed data sequences
64 are long or hierarchical structures are complex, e.g., [13].
65

There are also frequentist approaches for \mathcal{R}_t estimation. Abry et al. [19] proposed
66 regularizing the smoothness of \mathcal{R}_t through penalized regression with second-order
67 temporal regularization, additional spatial penalties, and with Poisson loss. Pascal et
68 al. [20] extended this procedure by introducing another penalty on outliers. Pircalabelu
69 et al. [21] proposed a spline-based model relying on the assumption of
70 exponential-family distributed incidence. Ho et al. [22] estimates \mathcal{R}_t while monitoring
71 the time-varying level of overdispersion. There are other spline-based approaches such
72 as [23, 24], autoregressive models with random effects [25] that are robust to low
73 incidence, and generalized autoregressive moving average models [26] that are robust to
74 measurement errors in incidence data.
75

We propose an instantaneous reproduction number estimator, called **RtEstim** that
76 requires only incidence data. Our model makes the conditional Poisson assumption,
77 similar to much of the prior work described above, but is empirically more robust to
78 misspecification. This estimator is defined by a convex optimization problem with
79 Poisson loss and ℓ_1 penalty on the temporal evolution of $\log(\mathcal{R}_t)$ to impose smoothness
80 over time. As a result, **RtEstim** generates discrete splines, and the estimated curves (in
81 logarithmic space) appear to be piecewise polynomials of an order selected by the user.
82 Importantly, the estimates are locally adaptive, meaning that different time ranges may
83 possess heterogeneous smoothness. Because we penalize the logarithm of \mathcal{R}_t , we
84 naturally accommodate the positivity requirement, in contrast to related
85

methods [19, 20], can handle large or small incidence measurements, and are automatically (reasonably) robust to outliers without additional constraints.

A small illustration using three years of Covid-19 case data in Canada [27] is shown in [Fig 1](#), where we consider a time-varying serial interval distribution. Specifically, we get the viral evolution and spread data from the [duotang](#) project [28] and compute the probabilities of having each variant at each timepoint using the multinomial logistic regression. The variant with the highest probability is deemed as the *dominant* variant at a specific timepoint. There are four dominant variants throughout the epidemic, Ancestral lineage, Alpha, Delta, and Omicron over time with means 5.1, 3.5, 3.5, 3.0 and standard deviations 4.0, 4.5, 2.9, 2.1 respectively, estimated by Xu et al. [29].

While our approach is straightforward and requires little domain knowledge for implementation, we also implement a number of refinements. We use a proximal Newton method to solve the convex optimization problem along with warm starts to produce estimates efficiently, typically in a matter of seconds, even for long sequences of data. In a number of simulation experiments, we show empirically that our approach is more *accurate* than existing methods at estimating the true instantaneous reproduction numbers and *robust* under multiple settings of the misspecification of incidence distribution, serial interval distribution, and the order of graphical curvature.

The manuscript proceeds as follows. We first introduce the methodology of [RtEstim](#) including the renewal equation and the development of Poisson trend filtering estimator. We explain how this method could be interpreted from the Bayesian perspective, connecting it to previous work in this context. We provide illustrative experiments comparing our estimator to other Bayesian alternatives. We then apply our [RtEstim](#) on the Covid-19 pandemic in Canada and the 1918 influenza pandemic in the United States. Finally, we conclude with a discussion of the advantages and limitations of our approach and describe practical considerations for instantaneous reproduction number estimation.

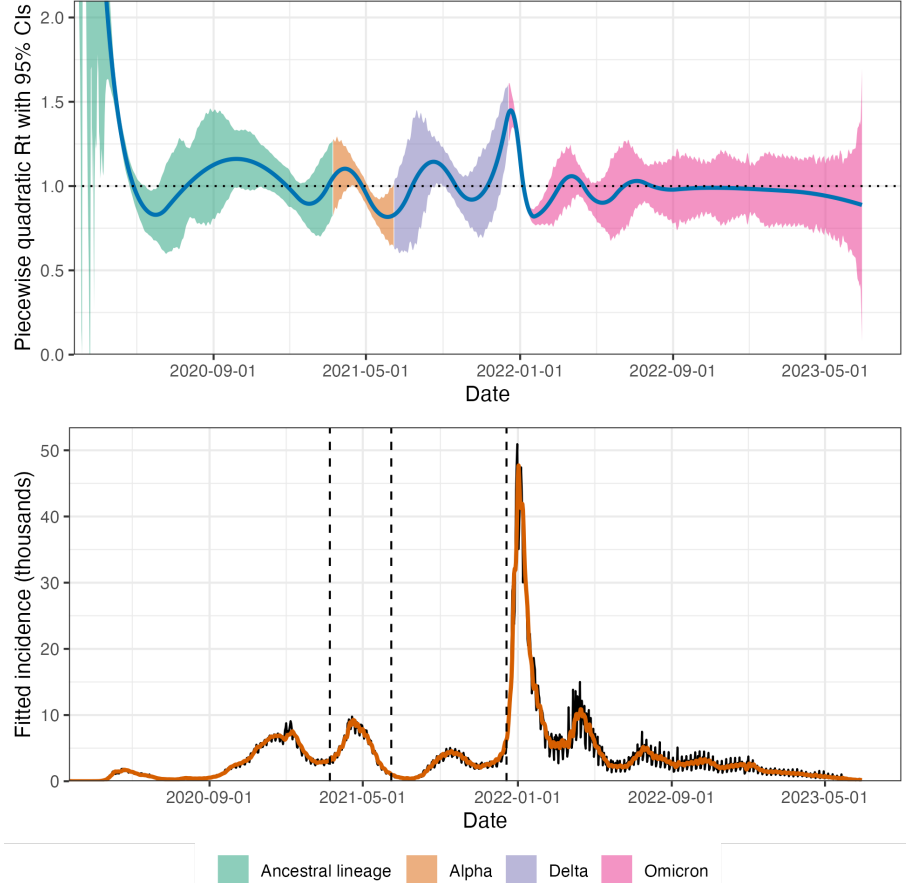


Fig 1. A demonstration of instantaneous reproduction number estimation by RtEstim and the corresponding predicted incident cases for the Covid-19 epidemic in Canada during the period from January 23, 2020 to June 28, 2023. In the top panel, the blue curve is the estimated piecewise quadratic \mathcal{R}_t and the colorful ribbon is the corresponding 95% confidence band. The ribbon is dyed by four colors representing the variants whose serial interval distributions are used to estimate \mathcal{R}_t . The y-axis is truncated for a better illustration; the estimated \mathcal{R}_t decreases from 10.77 to below 2 in the first 55 timepoints. In the bottom panel, the black curve is the observed Covid-19 daily confirmed cases, and the orange curve on top of it is the predicted incident cases corresponding to the estimated \mathcal{R}_t . The three vertical dashed lines represent the beginning of a new dominant variant.

2 Methods

2.1 Renewal model for incidence data

The instantaneous reproduction number $\mathcal{R}(t)$ is defined to be the expected number of secondary infections at time t produced by a primary infection sometime in the past. To make this precise, denote the number of new infections at time t as $y(t)$. Then the total primary infectiousness can be written as $\eta(t) := \int_0^\infty p(t, i)y(t - i)di$, where $p(t, i)$ is the

probability that a new secondary infection at time t is the result of a primary infection
 118 that occurred i time units in the past. The instantaneous reproduction number is then
 119 given as the value that equates
 120

$$\mathbb{E}[y(t) | y(j), j < t] = \mathcal{R}(t)\eta(t) = \mathcal{R}(t) \int_0^\infty p(t,i)y(t-i)di, \quad (1)$$

otherwise known as the renewal equation. The period between primary and secondary
 121 infections is exactly the generation time of the disease, but given real data, observed at
 122 discrete times (say, daily), this delay distribution must be discretized into contiguous
 123 time intervals, say, $(0, 1], (1, 2], \dots$. It results in the sequence $\{p_{t,i}\}_{i=0}^\infty$ corresponding to
 124 observations y_t for each t and yields the discretized version of Eq (1),
 125

$$\mathbb{E}[y_t | y_1, \dots, y_{t-1}] = \mathcal{R}_t\eta_t = \mathcal{R}_t \sum_{i=1}^{\infty} p_{t,i}y_{t-i}. \quad (2)$$

Many approaches to estimating \mathcal{R}_t rely on Eq (2) as motivation for their procedures,
 126 among them, **EpiEstim** [10] and **EpiFilter** [16].
 127

In most cases, it is safe to assume that infectiousness disappears beyond τ
 128 timepoints ($p(t, i) = 0$ for $i > \tau$), resulting in the truncated integral of the generation
 129 interval distribution $\int_0^\tau p(t,i)di = 1$ for each t . Generation time, however, is usually
 130 unobservable and tricky to estimate, so common practice is to approximate it by the
 131 serial interval: the period between the symptom onsets of primary and secondary
 132 infections. If the infectiousness profile after symptom onset is independent of the
 133 incubation period (the period from the time of infection to the time of symptom onset),
 134 then this approximation is justifiable: the serial interval distribution and the generation
 135 interval distribution share the same mean. However, other properties may not be
 136 similarly shared, and, in general, the generation interval distribution is a convolution of
 137 the serial interval distribution with the distribution of the difference between
 138 independent draws from the delay distribution from infection to symptom onset. See,
 139 for example, [3] for a fuller discussion of the dangers of this approximation. Nonetheless,
 140 treating these as interchangeable is common [10, 30] and doing otherwise is beyond the
 141 scope of this work. We will allow the delay distribution to be either constant over time
 142—the probability $p(i)$ depends only on the gap between primary and secondary
 143

infections and not on the time t when the secondary infection occurs—or to be
time-varying: $p(t, i)$ also depends on the time of the secondary infection. For our
methods, we assume that the serial interval can be accurately estimated from auxiliary
data (say by contact tracing, or previous epidemics) and we take it as fixed, as is
common in existing studies, [10, 19, 20].

The renewal equation in Eq (2) relates observable data streams (incident cases)
occurring at different timepoints to the instantaneous reproduction number given the
serial interval. The fact that it depends only on the observed incident counts makes it
reasonable to estimate \mathcal{R}_t . However, data collection idiosyncrasies can obscure this
relationship. Diagnostic testing targets symptomatic individuals, omitting
asymptomatic primary infections which can lead to future secondary infections. Testing
practices, availability, and uptake can vary across space and time [31, 32]. Finally,
incident cases as reported to public health are subject to delays due to laboratory
confirmation, test turnaround times, and eventual submission to public health [33]. For
these reasons, reported cases are lagging indicators of the course of the pandemic.
Furthermore, they do not represent the actual number of new infections that occur on a
given day, as indicated by exposure to the pathogen. The assumptions described above
(homogeneous mixing, similar susceptibility and social behaviours, etc.) are therefore
consequential. That said, Eq (2) also provides some comfort about deviations from
these assumptions. Under certain conditions, failing to account for the reporting
behaviours will minimally impact the accuracy of any \mathcal{R}_t estimator that is based on
Eq (2). We discuss three types of deviation here. First, if y_t is scaled by a constant a
describing the reporting ratio, then because it appears on both sides of Eq (2), \mathcal{R}_t will
be unchanged. Second, if such a scaling a_t varies in time, as long as it varies slowly
relative to p_i —that is, if $a_t / \sum_{i=1}^t a_i p_i \approx 1$ —then \mathcal{R}_t can still be estimated well from
reported incidence data. Finally, even a sudden change in reporting ratio occurs at time
 t_1 , it would only result in large errors in \mathcal{R}_t at times near t_1 (where the size of this
neighbourhood is determined indirectly by the effective support of $\{p_{t,i}\}$). On the other
hand, time-varying reporting delays would be much more detrimental [34, 35].

2.2 Poisson trend filtering estimator

173

We use the daily confirmed incident cases y_t on day t to estimate the observed infectious cases under the model that y_t , given previous incident cases y_{t-1}, \dots, y_1 and a constant serial interval distribution, follows a Poisson distribution with mean Λ_t . That is,

$$y_t | y_1, \dots, y_{t-1} \sim \text{Poisson}(\Lambda_t), \text{ where } \Lambda_t = \mathcal{R}_t \sum_{i=1}^{t-1} p_i y_{t-i} = \mathcal{R}_t \eta_t. \quad (3)$$

Given a history of n confirmed incident counts $\mathbf{y} = (y_1, \dots, y_n)^\top$, our goal is to estimate \mathcal{R}_t for each $t = 1, \dots, n$. A natural approach is to maximize the likelihood, producing the maximum likelihood estimator (MLE):

$$\begin{aligned} \hat{\mathcal{R}} &= \underset{\mathcal{R} \in \mathbb{R}_+^n}{\operatorname{argmax}} \mathbb{P}(\mathcal{R} | \mathbf{y}, \mathbf{p}) = \underset{\mathcal{R} \in \mathbb{R}_+^n}{\operatorname{argmax}} \prod_{t=1, \dots, n} \frac{(\mathcal{R}_t \eta_t)^{y_t} \exp\{-\mathcal{R}_t \eta_t\}}{y_t!} \\ &= \underset{\mathcal{R} \in \mathbb{R}_+^n}{\operatorname{argmin}} \sum_{t=1}^n \mathcal{R}_t \eta_t - y_t \log(\mathcal{R}_t \eta_t). \end{aligned} \quad (4)$$

This optimization problem, however, is easily seen to yield a one-to-one correspondence between the observation and the estimated instantaneous reproduction number, i.e., $\hat{\mathcal{R}}_t = y_t / \eta_t$, so that the estimated sequence $\hat{\mathcal{R}}$ will have no significant smoothness.

The MLE is an unbiased estimator of the true parameter \mathcal{R}_t , but unfortunately has high variance: changes in y_t result in proportional changes in $\hat{\mathcal{R}}_t$. To avoid this behaviour, and to match the intuition that $\mathcal{R}_t \approx \mathcal{R}_{t-1}$, we advocate enforcing smoothness of the instantaneous reproduction numbers. This constraint will decrease the estimation variance, and hopefully lead to more accurate estimation of \mathcal{R} , as long as the smoothness assumption is reasonable. Smoothness assumptions are common (see e.g., [3, 16]), but the type of smoothness assumption is critical. Cori et al. imposes smoothness indirectly by estimating \mathcal{R}_t with moving windows of past observations. The Kalman filter procedure of [16] would enforce in ℓ_2 -smoothness $(\int_0^n (\hat{\mathcal{R}}''(t))^2 dt < C$ for some constant C), although the computational implementation results in $\hat{\mathcal{R}}$ taking values over a discrete grid. Pascal et al. produces piecewise linear $\hat{\mathcal{R}}_t$, which turns out to be closely related to a special case of our methodology [20]. Smoother estimated curves will provide high-level information about the entire epidemic, obscuring small local changes in $\mathcal{R}(t)$, but may also remove the ability to detect large sudden changes,

such as those resulting from lockdowns or other major containment policies.

To enforce smoothness of $\widehat{\mathcal{R}}_t$, we add a trend filtering penalty [36–39] to Eq (5) .

Because $\mathcal{R}_t > 0$, we explicitly penalize the divided differences (discrete derivatives) of neighbouring values of $\log(\mathcal{R}_t)$. Let $\theta := \log(\mathcal{R}) \in \mathbb{R}^n$, so that $\Lambda_t = \eta_t \exp(\theta_t)$, and $\log(\eta_t \mathcal{R}_t) = \log(\eta_t) + \theta_t$. For evenly spaced incidence data, we write our estimator as the solution to the optimization problem

$$\widehat{\mathcal{R}} = \exp(\widehat{\theta}) \quad \text{where} \quad \widehat{\theta} = \underset{\theta \in \mathbb{R}^n}{\operatorname{argmin}} \eta^\top \exp(\theta) - \mathbf{y}^\top \theta + \lambda \|D^{(k+1)}\theta\|_1, \quad (5)$$

where $\exp(\cdot)$ applies elementwise and $\|\mathbf{a}\|_1 := \sum_{i=1}^n |a_i|$ is the ℓ_1 norm. Here, $D^{(k+1)} \in \mathbb{Z}^{(n-k-1) \times n}$ is the $(k+1)^{\text{th}}$ order divided difference matrix for any $k \in \{0, \dots, n-1\}$ with the convention that $D^{(0)} = \mathbf{0}_{n \times n}$. The divided difference matrix for $k=0$, $D^{(1)} \in \{-1, 0, 1\}^{(n-1) \times n}$, is a sparse matrix with diagonal band of the form:

$$D^{(1)} = \begin{pmatrix} -1 & 1 & & & \\ & -1 & 1 & & \\ & & \ddots & \ddots & \\ & & & -1 & 1 \end{pmatrix}. \quad (6)$$

For $k \geq 1$, $D^{(k+1)}$ can be defined recursively as $D^{(k+1)} := D^{(1)}D^{(k)}$, where $D^{(1)} \in \{-1, 0, 1\}^{(n-k-1) \times (n-k)}$ has the form Eq (6) but with modified dimensions.

The tuning parameter (hyperparameter) λ balances data fidelity with desired smoothness. When $\lambda = 0$, the problem in Eq (5) reduces to the MLE in Eq (4). Larger tuning parameters privilege the regularization term and yield smoother estimates. Finally, there exists λ_{\max} such that any $\lambda \geq \lambda_{\max}$ will result in $D^{(k+1)}\widehat{\theta} = 0$ and $\widehat{\theta}$ will be the Kullback-Leibler projection of \mathbf{y} onto the null space of $D^{(k+1)}$ (see subsection 2.3).

The solution to Eq (5) will result in piecewise polynomials, specifically called discrete splines. For example, 0th-degree discrete splines are piecewise constant, 1st-degree curves are piecewise linear, and 2nd-degree curves are piecewise quadratic. For $k \geq 1$, k^{th} -degree discrete splines are continuous and have continuous discrete differences up to degree $k-1$ at the knots (i.e., changing points between segments). This penalty results in more flexibility compared to the homogeneous smoothness that is created by the

squared ℓ_2 norm. Using different orders of the divided differences results in estimated
instantaneous reproduction numbers with different smoothness properties.

For unevenly spaced data, the spacing between neighbouring parameters varies with
the time between observations, and thus, the divided differences must be adjusted by
the times that the observations occur. Given observation times $\mathbf{x} = (x_1, \dots, x_n)^\top$, for
 $k \geq 1$, define a k^{th} -order diagonal matrix

$$X^{(k)} = \text{diag} \left(\frac{k}{x_{k+1} - x_1}, \frac{k}{x_{k+2} - x_2}, \dots, \frac{k}{x_n - x_{n-k}} \right). \quad (7)$$

Letting $D^{(\mathbf{x},1)} := D^{(1)}$, then for $k \geq 1$, the $(k+1)^{\text{th}}$ -order divided difference matrix for
unevenly spaced data can be created recursively by $D^{(\mathbf{x},k+1)} := D^{(1)} X^{(k)} D^{(\mathbf{x},k)}$. No
adjustment is required for $k = 0$.

Due to the penalty structure, this estimator is locally adaptive, meaning that it can
potentially capture local changes such as the initiation of control measures. Abry et al.
and Pascal et al. considered only the 2nd-order divided difference of \mathcal{R}_t rather than its
logarithm [19, 20]. In comparison to their work, our estimator (i) allows for arbitrary
degrees of temporal smoothness and (ii) avoids the potential numerical issues of
penalizing/estimating positive real values. Furthermore, as we will describe below, our
procedure is computationally efficient for estimation over an entire sequence of penalty
strengths λ and provides methods for choosing how smooth the final estimate should be.

2.3 Solving over a sequence of tuning parameters

We can solve the Poisson trend filtering estimator over an arbitrary sequence of λ that
produces different levels of smoothness in the estimated curves. We consider a
candidate set of M λ -values, $\boldsymbol{\lambda} = \{\lambda_m\}_{m=1}^M$, that is strictly decreasing.

Let $D := D^{(k+1)}$ for simplicity in the remainder of this section. As $\lambda \rightarrow \infty$, the
penalty term $\lambda \|D\theta\|_1$ dominates the Poisson objective, so that minimizing the objective
is asymptotically equivalent to minimizing the penalty term, which results in $\|D\theta\|_1 = 0$.
In this case, the divided differences of θ with order $k+1$ is always 0, and thus, θ must
lie in the null space of D , that is, $\theta \in \mathcal{N}(D)$. The same happens for any λ beyond this
threshold, so define λ_{\max} to be the smallest λ that produces $\theta \in \mathcal{N}(D)$. It turns out
that this value can be written explicitly as $\lambda_{\max} = \|(D^\dagger)^\top (\eta - y)\|_\infty$, where D^\dagger is the

(left) generalized inverse of D satisfying $D^\dagger D = I$ and $\|a\|_\infty := \max_i |a_i|$ is the infinity norm. Therefore, we use $\lambda_1 = \lambda_{\max}$ and choose the minimum λ_M to be $r\lambda_{\max}$ for some $r \in (0, 1)$ (typically $r = 10^{-4}$). Given any $M \geq 3$, we generate a sequence of λ values to be equally spaced on the log-scale between λ_1 and λ_M .

To compute the sequence of solutions efficiently, the model is estimated sequentially by visiting each component of $\boldsymbol{\lambda}$ in order. The estimates produced for a larger λ are used as the initial values (warm starts) for the next smaller λ . By solving through the entire sequence of tuning parameters, we improve computational efficiency and also enable one to trade between bias and variance, resulting in improved accuracy relative to procedures examining a single fixed tuning parameter.

2.4 Choosing a final λ

We estimate model accuracy over the candidate set through K -fold cross validation (CV) to choose the best tuning parameter. Specifically, we divide \mathbf{y} (except the first and last observations) roughly evenly and randomly into K folds, estimate \mathcal{R}_t for all $\boldsymbol{\lambda}$ leaving one fold out, and then predict the held-out observations. An alternative splitting of observations is regular splitting, where we assign every k^{th} observation into the same fold. Note that our approach is most closely related to non-parametric regression rather than time series forecasting. That said, under some conditions, one can guarantee that K -fold is valid for risk estimation in time series. The sufficient conditions are quite strong, but the guarantees are also stronger than would be required for model selection consistency [40].

Model accuracy can be measured by multiple metrics such as mean squared error $\text{MSE}(\hat{y}, y) = n^{-1} \|\hat{y} - y\|_2^2$ or mean absolute error $\text{MAE}(\hat{y}, y) = n^{-1} \|\hat{y} - y\|_1$, but we prefer to use the (average) deviance, to mimic the likelihood in Eq (4):

$$D(y, \hat{y}) = n^{-1} \sum_{i=1}^n 2(y_i \log(y_i) - y_i \log(\hat{y}_i) - y_i + \hat{y}_i),$$
 with the convention that $0 \log(0) = 0$. Note that for any K and any M , we will end up estimating the model $(K+1)M$ times rather than once.

2.5 Approximate confidence bands

276

We also provide empirical confidence bands of the estimators with approximate coverage. Consider the related estimator $\tilde{\mathcal{R}}_t$ defined as

$$\tilde{\mathcal{R}} = \exp(\tilde{\theta}) \quad \text{where} \quad \tilde{\theta} = \underset{\theta \in \mathbb{R}^n}{\operatorname{argmin}} \eta^\top \exp(\theta) - \mathbf{y}^\top \theta + \lambda \|D\theta\|_2^2. \quad (8)$$

Let $\tilde{\mathbf{y}} = \eta \circ \tilde{\mathcal{R}}$, and then it can be shown (for example, Theorem 2 in [41]) that an estimator for $\operatorname{Var}(\tilde{\mathbf{y}})$ is given by $(\operatorname{diag}(\tilde{\mathbf{y}}^{-2}) + \lambda D^\top D)^\dagger$. Finally, an application of the delta method shows that $\operatorname{Var}(\tilde{\mathbf{y}}_t)/\eta_t^2$ is an estimator for $\operatorname{Var}(\tilde{\mathcal{R}}_t)$ for each $t = 1, \dots, n$. We therefore use $(\operatorname{diag}(\hat{\mathbf{y}}^{-2}) + \lambda D^\top D)_t^\dagger/\eta_t^2$ as an estimator for $\operatorname{Var}(\hat{\mathcal{R}}_t)$. An approximate $(1 - \alpha)\%$ confidence interval then can be written as $\hat{\mathcal{R}}_t \pm s_t \times T_{\alpha/2, n-\text{df}}$, where s_t is the square-root of $\operatorname{Var}(\hat{\mathcal{R}}_t)$ for each $t = 1, \dots, n$ and df is the number of changepoints in $\hat{\theta}$ plus $k + 1$ [37]. An approximate confidence interval of $\hat{\mathbf{y}}$ can be computed similarly.

2.6 Bayesian perspective

287

Unlike many other methods for \mathcal{R}_t estimation, our approach is frequentist rather than Bayesian. Nonetheless, it has a corresponding Bayesian interpretation: as a state-space model with Poisson observational noise, autoregressive transition equation of degree $k \geq 0$, e.g., $\theta_{t+1} = 2\theta_t - \theta_{t-1} + \varepsilon_{t+1}$ for $k = 1$, and Laplace transition noise $\varepsilon_{t+1} \sim \text{Laplace}(0, 1/\lambda)$. Compared to **EpiFilter** [16], we share the same observational assumptions, but our approach has a different transition noise. **EpiFilter** estimates the posterior distribution of \mathcal{R}_t , and thus it can provide credible interval estimates as well. Our approach produces the maximum *a posteriori* estimate via an efficient convex optimization, obviating the need for MCMC sampling. But the associated confidence bands are created differently.

3 Results

298

Implementation of our approach is provided in the R package **rtestim**. All computational experiments are conducted on the Cedar cluster provided by Compute Canada with R 4.3.1. The R packages used for simulation and real-data application are

EpiEstim 2.2-4 [42], EpiLPS 1.2.0 [43], and rtestim 0.0.4. The R scripts for
 302
EpiFilter are used [44].
 303

3.1 Synthetic experiments

3.1.1 Design for the synthetic data

We simulate four scenarios of the time-varying instantaneous reproduction number,
 304 intended to mimic different epidemics. The first two scenarios are rapidly controlled by
 305 intervention, where the $\mathcal{R}(t)$ consists of one discontinuity and two segments. Scenario 1
 306 has constant $\mathcal{R}(t)$ before and after an intervention, while Scenario 2 grows exponentially,
 307 then decays. The other two scenarios are more complicated, where more waves are
 308 involved. Scenario 3 has four linear segments with three discontinuities, which reflect
 309 the effect of an intervention, resurgence to rapid transmission, and finally suppression of
 310 the epidemic. Scenario 4 involves sinusoidal waves throughout the epidemic. The first
 311 three scenarios and the last scenario are motivated by [16] and [17] respectively. We
 312 name the four scenarios as (1) *piecewise constant*, (2) *piecewise exponential*, (3)
 313 *piecewise linear*, and (4) *periodic* lines or curves respectively.
 314

In all cases, the times of observation are regular, and epidemics are of length
 315
 $n = 300$. Specifically, in Scenario 1, $\mathcal{R}_t = 2, 0.8$ before and after $t = 120$. In Scenario 2,
 316 \mathcal{R}_t increases and decreases exponentially with rates 0.01, 0.005 pre and post $t = 100$. In
 317 Scenario 3, \mathcal{R}_t is piecewise linear with four discontinuous segments following
 318

$$\begin{aligned} \mathcal{R}(t) = & \left(2.5 - \frac{0.5}{74} (t - 1) \right) \mathbf{1}_{[1,76)}(t) + \left(0.8 - \frac{0.2}{74} (t - 76) \right) \mathbf{1}_{[76,151)}(t) \\ & + \left(1.7 + \frac{0.3}{74} (t - 151) \right) \mathbf{1}_{[151,226)}(t) + \left(0.9 - \frac{0.4}{74} (t - 226) \right) \mathbf{1}_{[226,300]}(t), \end{aligned} \quad (9)$$

where $\mathbf{1}_A(t) = 1$, if $t \in A$, and $\mathbf{1}_A(t) = 0$ otherwise. In Scenario 4, \mathcal{R}_t is realization of
 321 the continuous, periodic curve generated by the function
 322

$$\mathcal{R}(t) = 0.2 \left((\sin(\pi t/12) + 1) + (2 \sin(5\pi t/12) + 2) + (3 \sin(5\pi t/6) + 3) \right), \quad (10)$$

evaluated at equally spaced points $t \in [0, 10]$. These \mathcal{R}_t scenarios are illustrated in Fig 2.
 323
 We compute the expected incidence Λ_t using the renewal equation, and generate the
 324 incident infections from the Poisson distribution with mean $\mathbb{E}[y_t] = \Lambda_t$. To verify the
 325

326 performance of our model under violations of the model's distributional assumption, we
327 also generate incident cases using the negative binomial distribution with dispersion
328 parameter $\rho = 5$ such that the mean is $\mathbb{E}[y_t] = \Lambda_t$ and the variance is
329 $\text{Var}[y_t] = \Lambda_t(1 + \Lambda_t/\rho)$ (following, for example, [17]). Because, $(1 + \Lambda_t/\rho) > 1$ for any
330 $\rho \geq 0$, this parameterization results in overdispersion relative to the Poisson
331 distribution, with smaller values of ρ leading to greater overdispersion. For context on
332 the actual dispersion of these synthetic experiments, Figure A.2.1 in the Supplement
333 displays the ratio of the time-varying standard deviation to the mean.
334

We use serial interval (SI) distributions of measles (with mean 14.9 and standard
334 deviation 3.9) at Hagelloch, Germany in 1861 [45] and SARS (with mean 8.4 and
335 standard deviation 3.8) at Hong Kong in 2003 [46], inspired by [10], to generate
336 synthetic epidemics. We initialize all epidemics with $y_1 = 2$ cases and generate for
337 $t = 2, \dots, 300$. The synthetic measles epidemics have smaller incident cases in general,
338 and the SARS epidemics have larger incidence. The intuition behind this is a smaller
339 mean of serial interval with a similar standard deviation leads to an averaged shorter
340 period of the onsets of symptoms between the primary and secondary infected
341 individuals, which results in a greater growth of incidence within the same period of
342 time. We also consider shorter flu epidemics with 50 timepoints with piecewise linear
343 \mathcal{R}_t (Scenario 3) considering both incidence distributional assumptions. The motivation
344 is to compare our method and other alternatives with EpiNow2 which takes much
345 longer time to converge for long epidemics (almost 2 hours to converge for a measles
346 epidemic with 300 timepoints) than other methods. Besides using the correct SI
347 distributions to estimate \mathcal{R}_t , we also consider the scenarios where SI is mildly or
348 majorly misspecified. More details on experimental settings and results for shorter
349 epidemics and misspecification of SI distributions are given in Sections A.2.1 and A.3 in
350 the supplementary document respectively.
351

For each problem setting (including a SI distribution, an \mathcal{R}_t scenario, and an
352 incidence distribution), we generate 50 random samples, resulting in 800 total synthetic
353 epidemics. An example of measles and SARS epidemics for each instantaneous
354 reproduction number scenario with an incidence distribution is displayed in Fig 2.
355

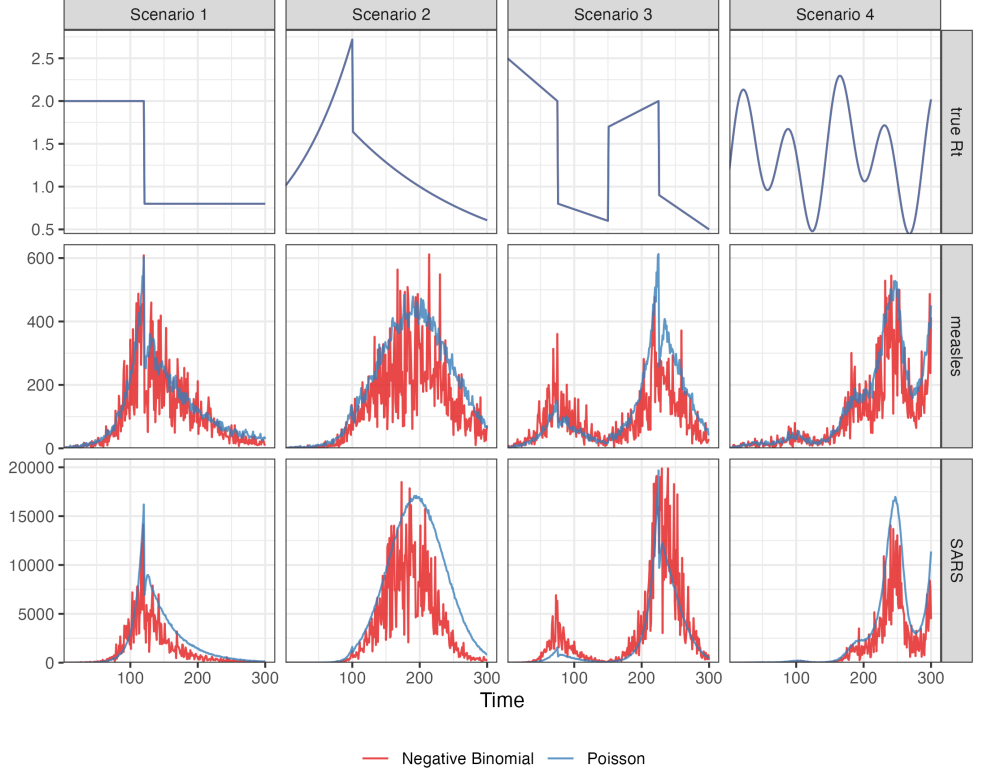


Fig 2. The instantaneous reproduction numbers for four \mathcal{R}_t scenarios (in the top row). The synthetic measles (in the middle row) and SARS (in the bottom row) incident cases drawn from Poisson (in blue curves) or negative binomial (in red curves) distribution across 4 \mathcal{R}_t scenarios (in four columns respectively).

3.1.2 Algorithmic choices

We compare **RtEstim** to **EpiEstim**, **EpiLPS**, and **EpiFilter**. **EpiEstim** estimates the posterior distribution of the instantaneous reproduction number given a Gamma prior and Poisson distributed observations over a trailing window, under the assumption that the instantaneous reproduction number is constant during that window. A larger window averages out more fluctuations, leading to smoother estimates, whereas, a shorter sliding window is more responsive to sudden spikes or declines. We tried the weekly sliding window, as well as a monthly window. However, since neither considerably outperforms the other across all scenarios, we defer the monthly results to the supplementary document. **EpiLPS** is another Bayesian approach that estimates P-splines based on the Laplace approximation to the conditional posterior with negative binomial likelihood. **EpiFilter** is also a Bayesian approach that filters \mathcal{R}_t at each timepoint given all using only incidence prior to t , using a particle filtering procedure on

a discrete grid of possible \mathcal{R}_t values.

In each setting, we apply `RtEstim` with four choices of $k = 0, 1, 2, 3$ resulting in different shapes of the estimated \mathcal{R}_t —piecewise constant, piecewise linear, piecewise quadratic, and piecewise cubic—respectively. We use 10-fold cross validation (CV) to choose the parameter λ that minimizes out-of-sample prediction risk from a candidate set of size 50, i.e., $\boldsymbol{\lambda} = \{\lambda_1, \dots, \lambda_{50}\}$, for long epidemics, and 5-fold CV for short epidemics (results for this case are deferred to Sections A.3.2 and A.4.2 in the Supplementary). Specifically, we divide all samples (except the first and last entries) into 10 folds evenly and randomly, and build models on each subset of samples by leaving a fold out using each choice of the tuning parameter. We select the tuning parameter that gives the lowest averaged deviance between the estimated incidence and the held-out samples averaged over all folds.

For the alternative methods, we generally use those that were applied to their own experimental settings. We consider both weekly and monthly sliding windows in `EpiEstim`. `EpiLPS` uses 40 P -spline basis functions and optimizes using the Nelder-Mead procedure. For `EpiFilter`, we specify a grid with 2000 cells, use 0.1 for the size of the diffusion noise, and use the “smoothed” \mathcal{R}_t (conditional on all data) as the final estimate.

For the \mathcal{R}_t estimation using all models for each problem, we use the same serial interval distribution, that was used to generate synthetic data. Taking different hyperparameters into consideration, we solve each problem using 8 methods including `EpiEstim` with weekly or monthly sliding windows, `EpiLPS`, `EpiFilter`, and `RtEstim` with piecewise constant, linear, quadratic, or cubic curves.

The choice of k explicitly controls the function space to which the solution will belong [38], providing the analyst with a mathematical understanding of the result. When faced with real data, the choice of k for `RtEstim` should be done either (1) based on the analyst’s preference for the result structure (e.g., “I want to find large jumps, so $k = 0$ ”) or (2) in a data-driven manner, as a component of the estimation process. Our software enables both cases, and the second case can be implemented by simply fitting for different k and choosing the set k, λ that has smallest CV score. Thus, all necessary choices can be accomplished based solely on the data, a departure from existing methods in that we both allow this choice and provide simple data-driven methods to

accomplish it.

401

3.1.3 Accuracy measurement

402

To measure estimation accuracy, we compare the estimated $\widehat{\mathcal{R}}$ to “true” \mathcal{R} using the Kullback-Leibler (KL) divergence. KL is useful in this context for a few reasons. First, it correctly handles the non-negativity constraint on \mathcal{R} . Second, KL matches the negative log-likelihood used in Eq (4). Third, it captures the curved geometry of the probability spaces implied by the Poisson distribution accurately. And fourth, as in the equation below, it has a convenient functional form depending only on \mathcal{R} and η . For the Poisson distribution (summed across all t) the KL divergence is defined as

$$D_{KL}(\mathcal{R} \parallel \widehat{\mathcal{R}}) = \sum_{t=1}^N \eta_t \left(\mathcal{R}_t \log \left(\frac{\mathcal{R}_t}{\widehat{\mathcal{R}}_t} \right) + \widehat{\mathcal{R}}_t - \mathcal{R}_t \right), \quad (11)$$

where $\mathcal{R} = \{\mathcal{R}_t\}_{t=1}^N$ and η_t is the total infectiousness. We use the average KL divergence: $\overline{D}_{KL}(\mathcal{R} \parallel \widehat{\mathcal{R}}) := D_{KL}(\mathcal{R} \parallel \widehat{\mathcal{R}})/N$. Details on the derivation of the KL divergence in Eq (11) is provided in Section A.1 in the supplementary document. To fairly compare across methods, we drop the first week of data, for a few reasons. Estimates from `EpiEstim` are not available until $t = 8$ (using a weekly sliding window). Additionally, some procedures purposely impose strong priors that R_1 is larger than 1 to avoid over confidently asserting that an epidemic is under control. The effect of these priors will persist for days or weeks, but one would hope for accurate estimates as early in the outbreak as possible.

410

411

412

413

414

415

416

417

418

419

420

421

422

423

3.2 Results for synthetic data

424

`RtEstim` overall outperforms the other competitors in the experimental study. Fig 3 and Fig 4 visualize the KL divergence across the seven methods. For low incidence in measles epidemics, `RtEstim` is the most accurate for all \mathcal{R}_t scenarios given both Poisson

425

426

427

and negative binomial incidence. The best performance of **RtEstim** has the lowest
 median and has low or no overlap with other methods. For Scenario 1, **EpiFilter** is a
 competitive alternative given Poisson incidence, which has similar median to the best
 performance of our **RtEstim** and with a small variation. While given negative binomial
 incidence, **EpiFilter** loses its advantage and even has the largest medians in Scenarios 1
 and 2. The large incidence in SARS epidemics imposes more difficulty of \mathcal{R}_t estimation
 for all methods. The best performance of our method is quite robust in the scale of
 incidence given Poisson data, since the KL values are of the similar scale for two types
 of epidemics. Given negative binomial incidence, **EpiLPS** shows robustness in the scale
 of incident cases in Scenarios 2 and 4. Our **RtEstim** has similar KL divergence values as
EpiLPS, where the counterpart boxes overlap to a large degree. We will examine a single
realization of each experiment to investigate these global conclusions in more detail.

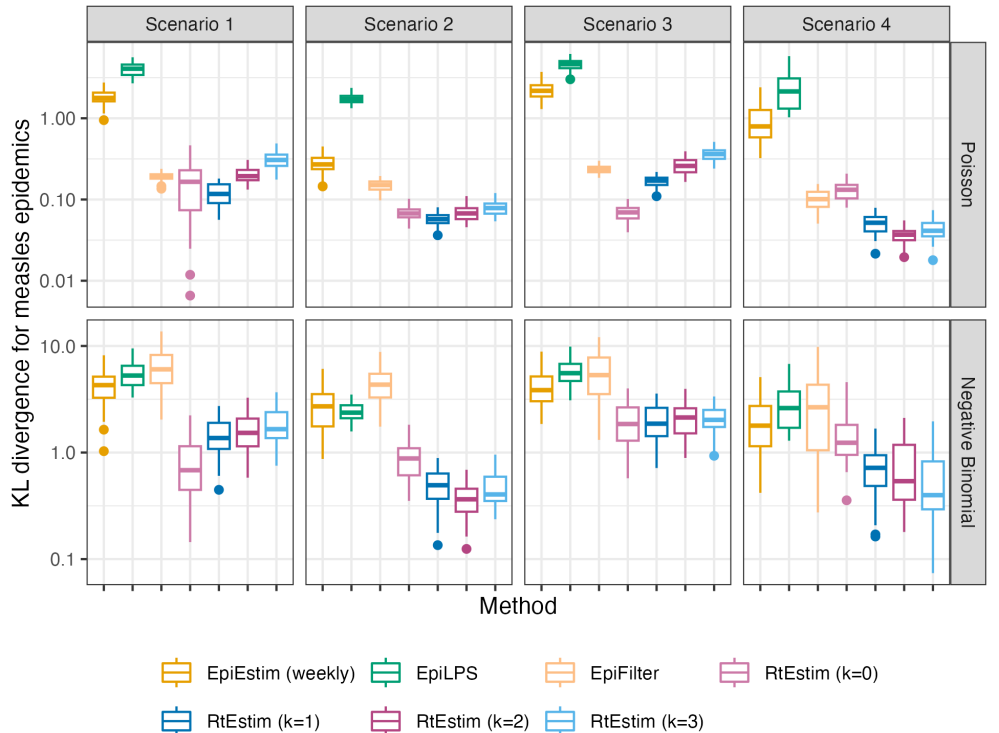


Fig 3. Boxplot of mean KL divergence between the estimated $\widehat{\mathcal{R}}_t$ and the true \mathcal{R}_t across 50 synthetic **measles** epidemics for each approach given Poisson incidence (*in top panels*) and negative binomial incidence (*in bottom panels*) respectively. The mean KL divergence ignores the first weeks in all experiments, since EpiEstim with the weekly sliding window does not provide estimates for the first week. Outliers beyond $1.5 \times \text{IQR}$ of each box are excluded, and full illustration in provided in the Figure A.3.1 in the supplementary document.

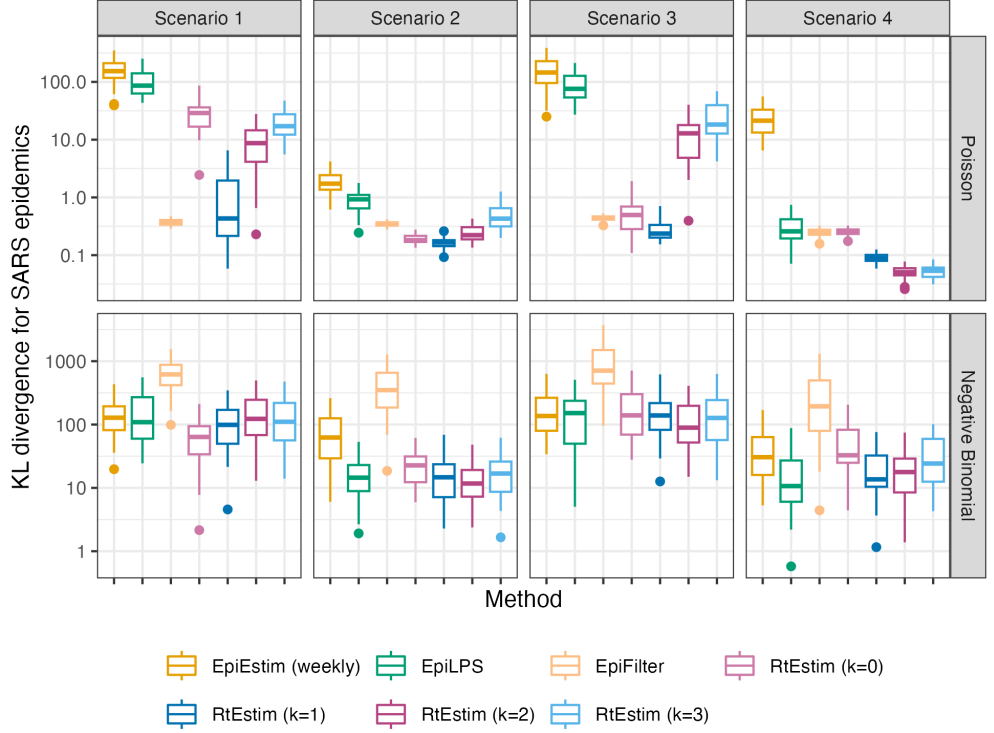


Fig 4. Boxplot of mean KL divergence between the estimated $\hat{\mathcal{R}}_t$ and the true \mathcal{R}_t across 50 synthetic **SARS** epidemics for each approach given Poisson incidence (*in top panels*) and negative binomial incidence (*in bottom panels*) respectively. The mean KL divergence ignores the first weeks in all experiments, since EpiEstim with the weekly sliding window does not provide estimates for the first week. Outliers beyond $1.5 \times \text{IQR}$ of each box are excluded, and full illustration in provided in the Figure A.3.1 in the supplementary document.

Fig 5 shows one realization for the estimated instantaneous reproduction number under the Poisson generative model in measles synthetic epidemics for all four scenarios. An expanded visualization with each estimated \mathcal{R}_t curve displayed in a separate panel is provided in Figure A.6.1 in the supplementary document. Ignoring the start of the epidemics, all methods look accurate and recover the underlying curves quite well, except EpiEstim with monthly sliding windows, where the trajectories are shifted to the right. Compared to EpiEstim and EpiLPS, which have rather severe difficulties at the beginning of the time series with extremely large estimates at the beginning and decreases rapidly, RtEstim and EpiFilter estimates are more accurate without suffering from the initialization problem. The edge problem in EpiEstim and EpiLPS might be due to the parameters used in their priors, say the prior mean of \mathcal{R}_t is initialized to be large, and the incidence data could not correct it during the beginning

of the epidemic. **RtEstim** can also have edge problem though, it is less severe in lower
452 orders. Besides the edge problem, **EpiEstim** (especially, with the monthly sliding
453 window) and **EpiLPS** produce “smooth” estimated curves that are continuous at the
454 changepoints in Scenarios 1-3, which results in large mistakes in these neighbourhoods.
455 Since the piecewise constant **RtEstim** estimator does not force any smoothness in \mathcal{R}_t , it
456 easily captures the sharp change and nearly overlaps with the true values in Scenario 1,
457 and **RtEstim** with other degrees also well capture the correct changepoints. Similar as
458 other methods, **RtEstim** also suffers from the difficulty to estimate the first few
459 timepoints, especially in the periodic scenario, where all methods miss to capture the
460 first peak with an accurate value. **EpiFilter** recover the \mathcal{R}_t curves well in general, but
461 are more wiggly than other methods.
462

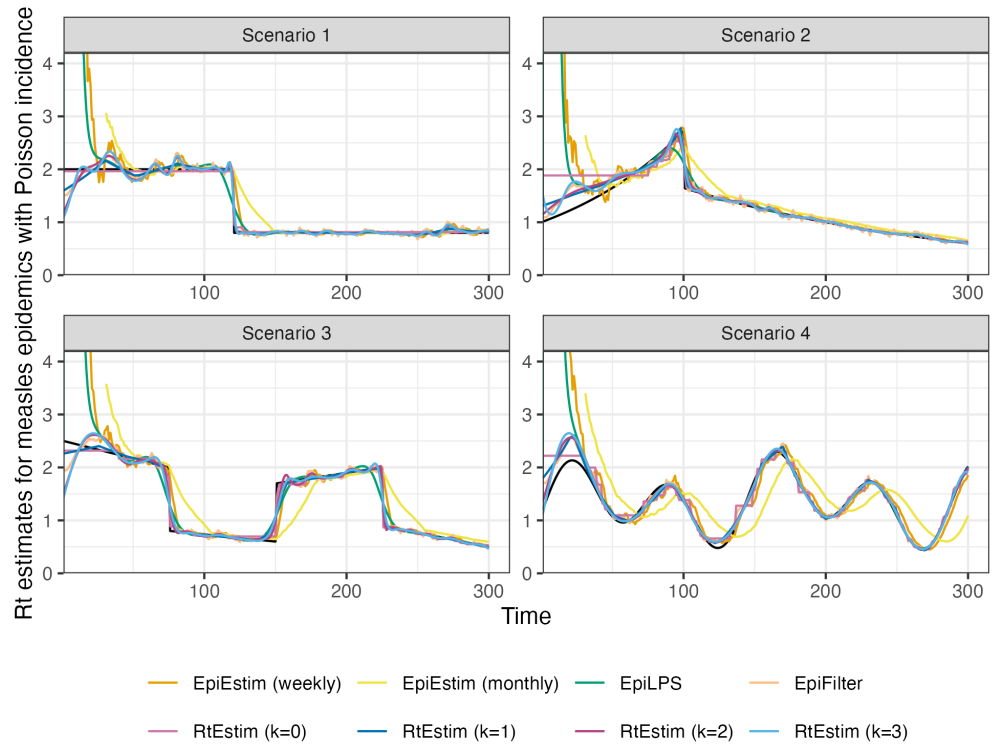


Fig 5. Example of instantaneous reproduction number estimation for **measles** epidemics with **Poisson** observations. An expanded visualization with each estimated \mathcal{R}_t curve displayed in a separate panel is provided in Figure A.6.1 in the supplementary document.

Fig 6 shows a realization of the estimated \mathcal{R}_t given negative binomial incidence in
463 SARS epidemics for each setting. An expanded visualization with each estimated \mathcal{R}_t
464 curve displayed in a separate panel is provided in Figure A.6.4 in the supplementary
465

document. Compared to the measles epidemics with Poisson data, all methods perform worse overall for SARS epidemics with negative binomial incidence due to two possible reasons, larger incidence and overdispersed data. The challenges to recover the start of epidemics are even harder in this setting for all methods. **EpiFilter** has much more wiggly estimates in this setting than the estimates of other methods compared to the setting in Fig 5. Our **RtEstim** estimates are close to the best performance in the first three \mathcal{R}_t scenarios, while face the challenge to recover the curve in the periodic scenario.

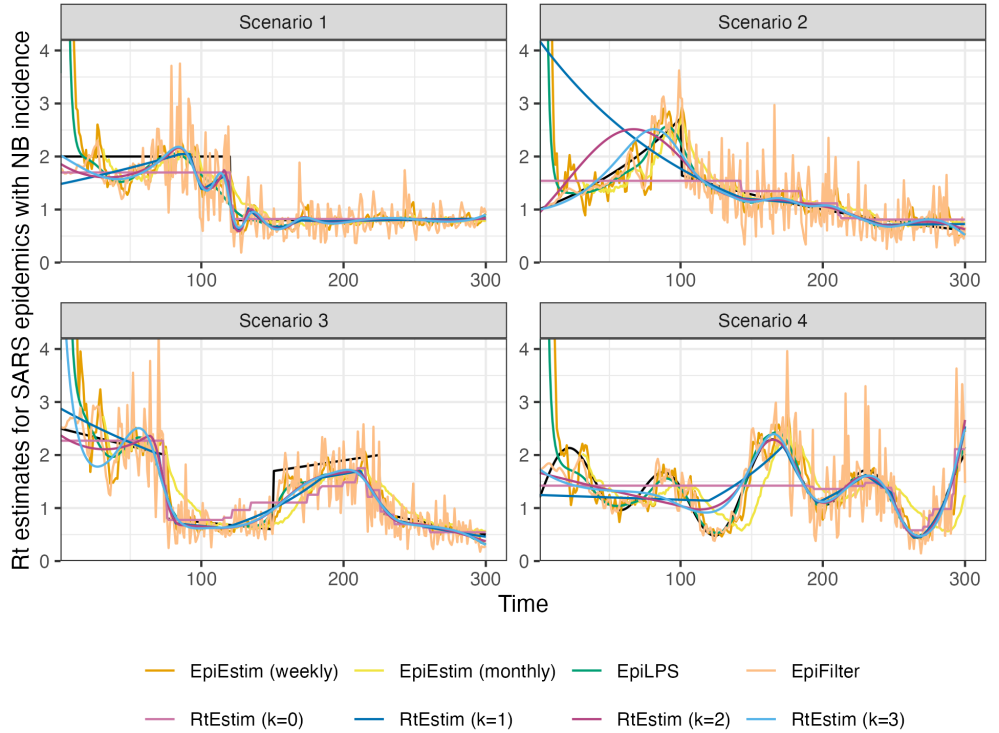


Fig 6. Example of instantaneous reproduction number estimation for **SARS** epidemics with **negative binomial** observations. An expanded visualization with each estimated \mathcal{R}_t curve displayed in a separate panel is provided in Figure A.6.4 in the supplementary document.

Finally, it is important to provide a brief comparison of the running times of all three models across the 8 experimental settings. We find that almost all models across all experiments complete within 10 seconds. **RtEstim** generally takes the longest, due to a relatively large number of estimates—50 values of λ and 10 folds of cross validation require 550 estimates—while other models run only a single time for a fixed setting of hyperparameters per experiment. Additional results on timing comparisons are deferred to the supplementary document.

3.3 Real-data results: Covid-19 incident cases in Canada

We implement `RtEstim` on Covid-19 confirmed incident cases in Canada (visualized in Fig 1). We use the weighted probabilities of serial interval distributions of four dominant variants used in Fig 1 as the serial interval distribution here for the comparison with other methods, which cannot incorporate time-varying serial interval distributions. We compute their percentages of days that they dominated throughout the pandemic as the weights in computation, specifically Ancestral lineage (32.6%), Alpha (8.5%), Delta (16.0%), and Omicron(42.9%) with sum 1. The estimates of our method is displayed in Fig 7, and the estimates of all competitors are deferred to Figures A.8.1 and A.8.2 in the supplementary document.

Considering the first, second, and third polynomial degrees, $\widehat{\mathcal{R}}_t$ for Covid-19 in Canada is always less than 2 except at the very early stage, which means that one distinct infected individual on average infects less than two other individuals in the population. Examining three different settings for k , the temporal evolution of $\widehat{\mathcal{R}}$ (across all regularization levels λ) are similar near the highest peak around the end of 2021 before dropping shortly thereafter. Throughout the estimated curves, the peaks and troughs of the instantaneous reproduction numbers precede the growth and decay cycles of confirmed cases, as expected. We also visualize 95% confidence bands for the point estimates with λ chosen by minimizing cross-validated KL divergence in Fig 7.

The estimated instantaneous reproduction numbers are relatively unstable before April, 2022. The highest peak coincides with the emergence and global spread of the Omicron variant. The estimated instantaneous reproduction numbers fall below 1 during a few time periods, where the most obvious troughs are roughly from April 2021 to July 2021 and from January, 2022 to April 2022. The first trough coincides with the introduction of Covid-19 vaccines in Canada. The second trough, shortly after the largest peak may be due to variety of factors resulting in the depletion of the susceptible population such as increased self-isolation in response to media coverage of the peak or immunity incurred via recent infection. Since April 2022, the estimated instantaneous reproduction number has remained relatively stable (fluctuating around one) corresponding to low reported cases, though reporting behaviours also changed significantly since the Omicron wave.

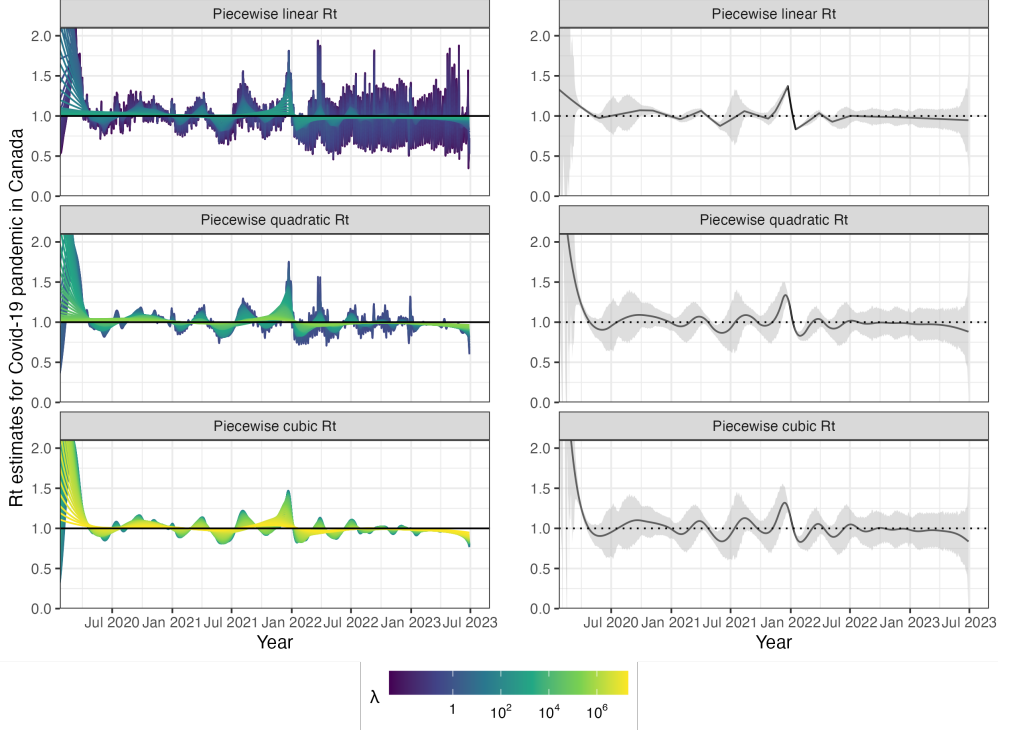


Fig 7. Estimated instantaneous eproduction number based on Covid-19 daily confirmed incident cases between January 23rd, 2020 and June 28th, 2023 in Canada. The left panels show estimates corresponding to 50 tuning parameters. The right panels show the CV-tuned estimate along with approximate 95% confidence bands. The top, middle and bottom panels show the estimated \mathcal{R}_t using the Poisson trend filtering in Eq (5) with degrees $k = 1, 2, 3$ respectively. All estimates are fitted using a constant serial interval distribution, which is the weighted sum of probabilities of the 4 dominant variants per timepoint used in Fig 1. All panels are truncated in y-axes for better illustration. The CV-tuned \mathcal{R}_t estimates rapidly decrease at the early stage from 3.37, 5.16 in \mathcal{R}_t curves with $k = 2, 3$ respectively.

3.4 Real-data results: influenza in Baltimore, Maryland, 1918

We also apply `RtEstim` to daily reported influenza cases in Baltimore, Maryland occurring during the world-wide pandemic of 1918 from September to November [47]. The data, shown in Fig 8, is included in the `EpiEstim` R package. We use the serial interval distribution provided by the `EpiEstim` R package for this pandemic in modelling. The 1918 influenza outbreak, caused by the H1N1 influenza A virus, was unprecedentedly deadly with case fatality rate over 2.5%, infecting almost one-third of the population across the world [48]. The CV-tuned piecewise cubic estimates in Fig 9 better capture the growth at the beginning of the pandemic in Fig 8. The estimated \mathcal{R}_t curve suggests that the transmissibility of the pandemic grew rapidly over the first 30

days before declining below one after 50 days. However, it also suggests an increase in
521 infectiousness toward the end of the period. With this data, it is difficult to determine if
522 there is a second wave or a steady decline ahead. The CV-tuned piecewise constant and
523 linear estimates in Fig 9 both suggest a steady decline. This conclusion is supported by
524 the fact that incident cases decline to zero at the end of the period and matches \mathcal{R}
525 estimates in [10], which are all lower than one. The estimation using alternatives is
526 deferred to Figures A.8.3 and A.8.4 in the supplementary document.
527

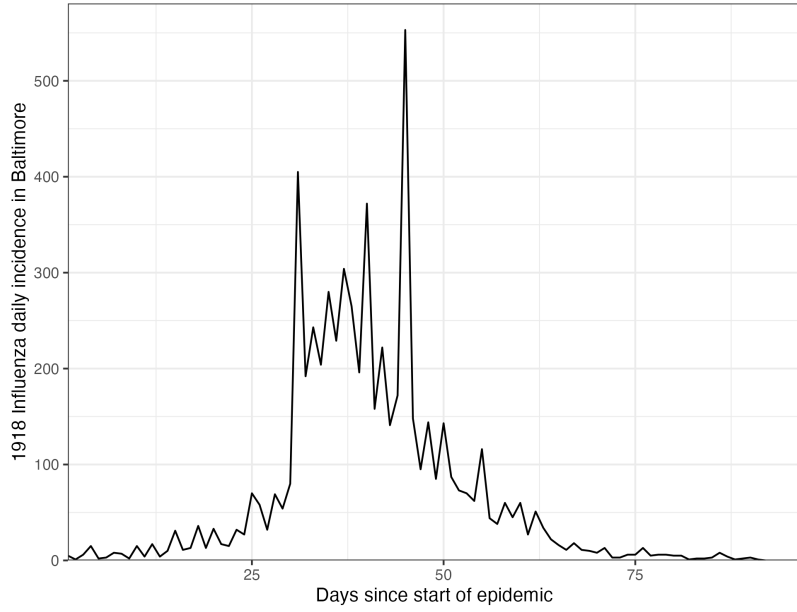


Fig 8. Daily incident influenza cases in Baltimore, Maryland between September and November in 1918.

4 Discussion

The `RtEstim` methodology provides a locally adaptive estimator using Poisson trend filtering on univariate data. It captures the heterogeneous smoothness of instantaneous reproduction numbers given observed incidence data rather than resulting in global
528 smoothness. This is a nonparametric regression model which can be written as a convex
529 optimization (minimization) problem. Minimizing the distance (KL divergence across
530 all coordinates) between the estimators and (functions of) observations guarantees data
531 fidelity while the penalty on divided differences between pairs of neighbouring
532 parameters imposes smoothness. The ℓ_1 -regularization results in sparsity of the divided
533 parameters.
534

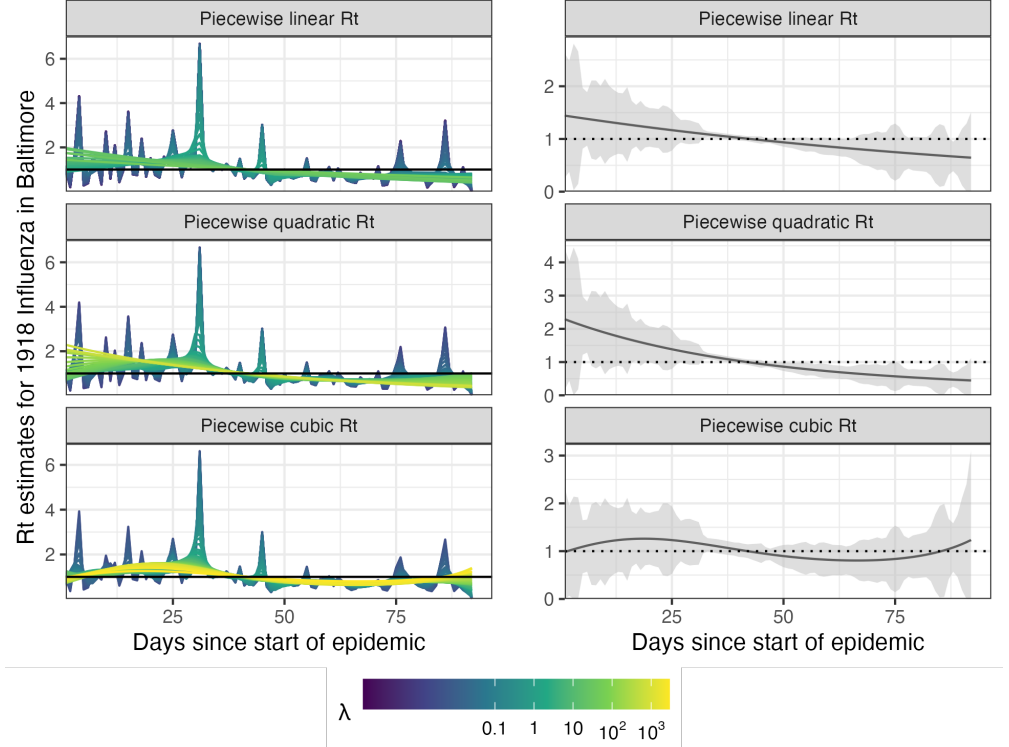


Fig 9. Estimated instantaneous reproduction numbers for influenza in Baltimore, Maryland in 1918. The left panels show estimates for a set of 50 tuning parameters. The right column displays the CV-tuned estimates with approximate 95% confidence bands. The rows (top to bottom) show estimated instantaneous reproduction numbers (\mathcal{R}_t) using the Poisson trend filtering in Eq (5) with $k = 1, 2, 3$ respectively.

differences, which leads to heterogeneous smoothness across time. 537

The property of local adaptivity (heterogenous smoothness) is useful to 538 automatically distinguish, for example, seasonal outbreaks from outbreaks driven by 539 other factors (behavioural changes, foreign introduction, etc.). Given a well-chosen 540 polynomial degree, the growth rates can be quickly detected, potentially advising public 541 health authorities to implement policy changes. The instantaneous reproduction 542 numbers can be estimated retrospectively to examine the efficacy of such policies, 543 whether they result in \mathcal{R}_t falling below 1 or the speed of their effects. The smoothness 544 of \mathcal{R}_t curves (including the polynomial degrees and tuning parameters) should be 545 chosen based on the purpose of the study in practice. 546

Our method `RtEstim` provides a natural way to deal with missing data, for example, 547 on weekends and holidays or due to changes in reporting frequency. While solving the 548 convex optimization problem, our method can easily handle uneven spacing or irregular 549

reporting. Computing the total primary infectiousness is also easily generalized to
irregular reporting by modifying the discretization of the serial interval distribution.
There are many other aspects to be considered in choosing the delay distribution to
improve accuracy [35]. Additionally, because the ℓ_1 penalty introduces sparsity
(operating like a median rather than a mean), this procedure is relatively insensitive to
spurious outliers compared to ℓ_2 regularization. Another natural extension is to
distinguish imported cases from the local cases in the procedure, following the
suggestions of [11]. By including imported cases only in η_t rather than in both y_t and
 η_t , we exclude individuals who were infected elsewhere, lowering \mathcal{R}_t , but correctly
reflecting the number of new primary infectees.

There are a number of limitations that may influence the quality of \mathcal{R}_t estimation.
While our model is generic for incidence data rather than tailored to any specific
disease, it does assume that the generation interval is short relative to the period of
data collection. More specialized methodologies would be required for diseases with long
incubation periods such as HIV or Hepatitis. Our approach, does not explicitly model
imported cases, nor distinguish between subpopulations that may have different mixing
behaviour. While the Poisson assumption is common, it does not handle overdispersion
(observation variance larger than the mean). The negative binomial distribution is a
good alternative, but more difficult to estimate in this context. As described in
[section 1](#), the expression for \mathcal{R} assumes that a relatively constant proportion of true
infections is reported. However, if this proportion varies with time (say, due to changes
in surveillance practices or testing recommendations), the estimates may be biased over
this window. A good example is in early January 2022, during the height of the
Omicron wave, Canada moved from testing all symptomatic individuals to testing only
those in at-risk groups. The result was a sudden change that would render \mathcal{R}_t estimates
on either side of this timepoint incommensurable.

Our `RtEstim` implementation can take a fixed serial interval throughout the period
of study (as implemented in simulation and in the real epidemics) or use time-varying
serial interval distributions (as implemented in [Fig 1](#) for Covid-19 data in Canada). In
reality, the serial interval may vary due to changes in the factors such as population
immunity [12]. One issue regarding the serial interval distribution relates to equating
serial and generation intervals (also mentioned above). The serial interval distribution is

generally wider than that of the generation interval, because the serial interval involves
582
the convolution of two distributions, and is unlikely to actually follow a named
583 distribution like Gamma, though it may be reasonably well approximated by one. Our
584 implementation allows for an arbitrary distribution to be used, but requires the user to
585 specify the discretization explicitly, requiring more nuanced knowledge than is typically
586 available. Pushing this analysis further, to accommodate other types of incidence data
587 (hospitalizations or deaths), a modified generation interval distribution would be
588 necessary, and further assumptions would be required as well. Or else, one would first
589 need to deconvolve deaths to infection onset before using our software.
590

Accurate statistical coverage of a function is a difficult problem, and the types of
591 (frequentist) guarantees that can be made are not always what one would want [49]. We
592 examine the coverage of our approximate confidence interval in simulation. (Details are
593 deferred to Section A.6 in the supplementary document). Empirically, our observations
594 for our method, as well as all others we have seen, follow a similar (undesirable) pattern:
595 when \mathcal{R}_t is stable, they over cover dramatically (even implausibly narrow intervals have
596 100% coverage); but when \mathcal{R}_t changes abruptly, they under cover. Theoretically,
597 whether these intervals should be expected to provide $(1 - \alpha)\%$ coverage simultaneously
598 over all time while being narrow enough to provide useful uncertainty quantification is
599 neither easy nor settled.
600

Nonetheless, our methodology is implemented in a lightweight R package **rtestim**
601 and computed efficiently, especially for large-scale data, with a proximal Newton solver
602 coded in C++. Given available incident case data, prespecified serial interval distribution,
603 and a choice of degree k , **RtEstim** is able to produce accurate estimates of
604 instantaneous reproduction number and provide efficient tuning parameter selection via
605 cross validation.
606

Acknowledgments

This research was enabled in part by support provided by BC DRI group who manages
608 Cedar cloud (<https://docs.alliancecan.ca/wiki/Cedar>) and the Digital Research Alliance
609 of Canada (alliancecan.ca).
610

References

1. Nishiura H, Chowell G. The effective reproduction number as a prelude to statistical estimation of time-dependent epidemic trends. Mathematical and statistical estimation approaches in epidemiology. 2009; p. 103–121.
2. Fraser C. Estimating individual and household reproduction numbers in an emerging epidemic. PloS one. 2007;2(8):e758.
3. Gostic KM, McGough L, Baskerville EB, Abbott S, Joshi K, Tedijanto C, et al. Practical considerations for measuring the effective reproductive number, R_t . PLoS Computational Biology. 2020;16(12):e1008409.
4. Anderson RM, May RM. Infectious diseases of humans: dynamics and control. Oxford university press; 1991.
5. Wallinga J, Teunis P. Different epidemic curves for severe acute respiratory syndrome reveal similar impacts of control measures. American Journal of epidemiology. 2004;160(6):509–516.
6. Hao X, Cheng S, Wu D, Wu T, Lin X, Wang C. Reconstruction of the full transmission dynamics of COVID-19 in Wuhan. Nature. 2020;584(7821):420–424.
7. Goldstein IH, Parker DM, Jiang S, Minin VM. Semiparametric inference of effective reproduction number dynamics from wastewater pathogen surveillance data. arXiv preprint arXiv:230815770. 2023;.
8. Goldstein IH, Wakefield J, Minin VM. Incorporating testing volume into estimation of effective reproduction number dynamics. Journal of the Royal Statistical Society Series A: Statistics in Society. 2024;187(2):436–453.
9. Cori A, Cauchemez S, Ferguson NM, Fraser C, Dahlqwist E, Demarsh PA, et al.. EpiEstim: estimate time varying reproduction numbers from epidemic curves; 2020.
10. Cori A, Ferguson NM, Fraser C, Cauchemez S. A new framework and software to estimate time-varying reproduction numbers during epidemics. American Journal of Epidemiology. 2013;178(9):1505–1512.

11. Thompson RN, Stockwin JE, van Gaalen RD, Polonsky JA, Kamvar ZN, Demarsh PA, et al. Improved inference of time-varying reproduction numbers during infectious disease outbreaks. *Epidemics*. 2019;29:100356.
12. Nash RK, Bhatt S, Cori A, Nouvellet P. Estimating the epidemic reproduction number from temporally aggregated incidence data: A statistical modelling approach and software tool. *PLoS Computational Biology*. 2023;19(8):e1011439.
13. Abbott S, Hellewell J, Thompson RN, Sherratt K, Gibbs HP, Bosse NI, et al. Estimating the time-varying reproduction number of SARS-CoV-2 using national and subnational case counts. *Wellcome Open Research*. 2020;5:112.
14. Abbott S, Funk S, Hickson J, Badr HS, Monticone P, Ellis P, et al.. epiforecasts/EpiNow2: 1.4.0 release; 2023.
15. Lison A, Abbott S, Huisman J, Stadler T. Generative Bayesian modeling to nowcast the effective reproduction number from line list data with missing symptom onset dates. *PLoS Computational Biology*. 2024;20(4):e1012021.
16. Parag KV. Improved estimation of time-varying reproduction numbers at low case incidence and between epidemic waves. *PLoS Computational Biology*. 2021;17(9):e1009347.
17. Gressani O, Wallinga J, Althaus CL, Hens N, Faes C. EpiLPS: A fast and flexible Bayesian tool for estimation of the time-varying reproduction number. *PLoS Computational Biology*. 2022;18(10):e1010618.
18. Trevisin C, Bertuzzo E, Pasetto D, Mari L, Miccoli S, Casagrandi R, et al. Spatially explicit effective reproduction numbers from incidence and mobility data. *Proceedings of the National Academy of Sciences*. 2023;120(20):e2219816120.
19. Abry P, Pustelnik N, Roux S, Jensen P, Flandrin P, Gribonval R, et al. Spatial and temporal regularization to estimate COVID-19 reproduction number $R(t)$: Promoting piecewise smoothness via convex optimization. *PLoS ONE*. 2020;15(8):e0237901.
20. Pascal B, Abry P, Pustelnik N, Roux S, Gribonval R, Flandrin P. Nonsmooth convex optimization to estimate the Covid-19 reproduction number space-time

- evolution with robustness against low quality data. *IEEE Transactions on Signal Processing*. 2022;70:2859–2868.
21. Pircalabelu E. A spline-based time-varying reproduction number for modelling epidemiological outbreaks. *Journal of the Royal Statistical Society Series C: Applied Statistics*. 2023;72(3):688–702.
 22. Ho F, Parag KV, Adam DC, Lau EH, Cowling BJ, Tsang TK. Accounting for the Potential of Overdispersion in Estimation of the Time-varying Reproduction Number. *Epidemiology*. 2023;34(2):201–205.
 23. Azmon A, Faes C, Hens N. On the estimation of the reproduction number based on misreported epidemic data. *Statistics in Medicine*. 2014;33(7):1176–1192.
 24. Gressani O, Faes C, Hens N. An approximate Bayesian approach for estimation of the instantaneous reproduction number under misreported epidemic data. *Biometrical Journal*. 2022;65(6):2200024.
 25. Jin S, Dickens BL, Lim JT, Cook AR. EpiMix: A novel method to estimate effective reproduction number. *Infectious Disease Modelling*. 2023;8(3):704–716.
 26. Hettinger G, Rubin D, Huang J. Estimating the instantaneous reproduction number with imperfect data: a method to account for case-reporting variation and serial interval uncertainty. *arXiv preprint arXiv:230212078*. 2023;.
 27. Berry I, O'Neill M, Sturrock SL, Wright JE, Acharya K, Brankston G, et al. A sub-national real-time epidemiological and vaccination database for the COVID-19 pandemic in Canada. *Scientific Data*. 2021;8(1). doi:10.1038/s41597-021-00955-2.
 28. Coronavirus Variants Rapid Response Network Computational Analysis M, Group EOC. CoVaRR-NET/duotang: Release for Zenodo Archive; 2023. Available from: <https://doi.org/10.5281/zenodo.10367461>.
 29. Xu X, Wu Y, Kummer AG, Zhao Y, Hu Z, Wang Y, et al. Assessing changes in incubation period, serial interval, and generation time of SARS-CoV-2 variants of concern: a systematic review and meta-analysis. *BMC medicine*. 2023;21(1):374.

30. Park SW, Sun K, Champredon D, Li M, Bolker BM, Earn DJ, et al. Forward-looking serial intervals correctly link epidemic growth to reproduction numbers. *Proceedings of the National Academy of Sciences*. 2021;118(2):e2011548118.
31. Pitzer VE, Chitwood M, Havumaki J, Menzies NA, Perniciaro S, Warren JL, et al. The impact of changes in diagnostic testing practices on estimates of COVID-19 transmission in the United States. *American Journal of Epidemiology*. 2021;190(9):1908–1917.
32. Hitchings MD, Dean NE, García-Carreras B, Hladish TJ, Huang AT, Yang B, et al. The usefulness of the test-positive proportion of severe acute respiratory syndrome coronavirus 2 as a surveillance tool. *American Journal of Epidemiology*. 2021;190(7):1396–1405.
33. Pellis L, Scarabel F, Stage HB, Overton CE, Chappell LH, Fearon E, et al. Challenges in control of COVID-19: short doubling time and long delay to effect of interventions. *Philosophical Transactions of the Royal Society B*. 2021;376(1829):20200264.
34. Eales O, Riley S. Differences between the true reproduction number and the apparent reproduction number of an epidemic time series. *Epidemics*. 2024;46:100742. doi:<https://doi.org/10.1016/j.epidem.2024.100742>.
35. Park SW, Akhmetzhanov AR, Charniga K, Cori A, Davies NG, Dushoff J, et al. Estimating epidemiological delay distributions for infectious diseases. *medRxiv*. 2024; p. 2024–01.
36. Kim SJ, Koh K, Boyd S, Gorinevsky D. ℓ_1 trend filtering. *SIAM Review*. 2009;51(2):339–360.
37. Tibshirani RJ. Adaptive piecewise polynomial estimation via trend filtering. *The Annals of Statistics*. 2014;42(1):285–323.
38. Tibshirani RJ. Divided differences, falling factorials, and discrete splines: Another look at trend filtering and related problems. *Foundations and Trends® in Machine Learning*. 2022;15(6):694–846.

39. Sadhanala V, Bassett R, Sharpnack J, McDonald DJ. Exponential family trend filtering on lattices. *Electronic Journal of Statistics*. 2024;18(1):1749–1814.
40. Bergmeir C, Hyndman RJ, Koo B. A note on the validity of cross-validation for evaluating autoregressive time series prediction. *Computational Statistics & Data Analysis*. 2018;120:70–83. doi:<https://doi.org/10.1016/j.csda.2017.11.003>.
41. Vaiter S, Deledalle C, Fadili J, Peyré G, Dossal C. The degrees of freedom of partly smooth regularizers. *Annals of the Institute of Statistical Mathematics*. 2017;69:791–832.
42. Cori A, Kamvar Z, Stockwin J, Jombart T, Dahlgquist E, FitzJohn R, et al.. EpiEstim v2.2-4: A tool to estimate time varying instantaneous reproduction number during epidemics; 2022. <https://github.com/mrc-ide/EpiEstim>.
43. Gressani O. EpiLPS: A Fast and Flexible Bayesian Tool for Estimating Epidemiological Parameters.; 2021. <https://epilps.com/>.
44. Parag KV. EpiFilter; 2020.
<https://github.com/kpzoo/EpiFilter?tab=readme-ov-file>.
45. Groendyke C, Welch D, Hunter DR. Bayesian inference for contact networks given epidemic data. *Scandinavian Journal of Statistics*. 2011;38(3):600–616.
46. Lipsitch M, Cohen T, Cooper B, Robins JM, Ma S, James L, et al. Transmission dynamics and control of severe acute respiratory syndrome. *science*. 2003;300(5627):1966–1970.
47. Frost WH, Sydenstricker E. Influenza in Maryland: preliminary statistics of certain localities. *Public Health Reports (1896-1970)*. 1919; p. 491–504.
48. Taubenberger JK, Morens DM. 1918 Influenza: the mother of all pandemics. *Emerging Infectious Diseases*. 2006;17(1):69–79.
49. Genovese C, Wasserman L. Adaptive confidence bands. *The Annals of Statistics*. 2008;36(2):875 – 905. doi:10.1214/07-AOS500.

Supplementary details on experiments of effective reproduction number estimation with trend filtering

Jiapeng Liu, Zhenglun Cai, Paul Gustafson, and Daniel J. McDonald

A.1 Derivation of Kullback Leibler divergence for accuracy comparison

We provide the detailed derivation of the Kullback Leibler (KL) divergence in (11) that is used to compare the accuracy of the estimated effective reproduction number with the true ones. Given the total infectiousness η , we compare the distance between the Poisson distributions $f_1(y; \eta, \hat{\mathcal{R}}) = Pois(\eta\hat{\mathcal{R}})$ and $f_0(y; \eta, \mathcal{R}) = Pois(\eta\mathcal{R})$, where $y, \mathcal{R} \in \mathbb{N}_0^n$ are natural numbers including 0, $\eta \in \mathbb{R}^n$, $f_0(y) = \prod_{t=1}^n \frac{(\eta_t \mathcal{R}_t)^{y_t} e^{-\eta_t \mathcal{R}_t}}{y_t!}$, $f_1(y) = \prod_{t=1}^n \frac{(\eta_t \hat{\mathcal{R}}_t)^{y_t} e^{-\eta_t \hat{\mathcal{R}}_t}}{y_t!}$, $y_t \in \mathbb{N}_0 = \{0, 1, 2, \dots\}$. Then, the KL divergence between them is defined as

$$\begin{aligned}
D_{KL}(\mathcal{R} || \hat{\mathcal{R}}) &= D_{KL}(f_0(y) || f_1(y)) \\
&= \sum_{y \in \mathbb{N}_0^n} f_0(y) \log \frac{f_0(y)}{f_1(y)} \\
&= \sum_{y \in \mathbb{N}_0^n} \prod_{t=1}^n \frac{(\eta_t \mathcal{R}_t)^{y_t} e^{-\eta_t \mathcal{R}_t}}{y_t!} \log \prod_{t=1}^n \frac{\mathcal{R}_t^{y_t} e^{-\eta_t \mathcal{R}_t}}{\hat{\mathcal{R}}_t^{y_t} e^{-\eta_t \hat{\mathcal{R}}_t}} \\
&= \sum_{y_n=0}^{\infty} \dots \sum_{y_1=0}^{\infty} \prod_{t=1}^n \frac{(\eta_t \mathcal{R}_t)^{y_t} e^{-\eta_t \mathcal{R}_t}}{y_t!} \sum_{t=1}^n \left(y_t \log \frac{\mathcal{R}_t}{\hat{\mathcal{R}}_t} - \eta_t (\mathcal{R}_t - \hat{\mathcal{R}}_t) \right) \text{ for independent } y_t, t = 1, \dots, n \\
&= \sum_{y_n=0}^{\infty} \frac{(\eta_n \mathcal{R}_n)^{y_n} e^{-\eta_n \mathcal{R}_n}}{y_n!} \dots \sum_{y_1=0}^{\infty} \frac{(\eta_1 \mathcal{R}_1)^{y_1} e^{-\eta_1 \mathcal{R}_1}}{y_1!} \left(y_1 \log \frac{\mathcal{R}_1}{\hat{\mathcal{R}}_1} + \sum_{t=2}^n y_t \log \frac{\mathcal{R}_t}{\hat{\mathcal{R}}_t} - \sum_{t=1}^n \eta_t (\mathcal{R}_t - \hat{\mathcal{R}}_t) \right) \\
&= \sum_{y_n=0}^{\infty} \frac{(\eta_n \mathcal{R}_n)^{y_n} e^{-\eta_n \mathcal{R}_n}}{y_n!} \dots \sum_{y_2=0}^{\infty} \frac{(\eta_2 \mathcal{R}_2)^{y_2} e^{-\eta_2 \mathcal{R}_2}}{y_2!} \left(\eta_1 \mathcal{R}_1 \log \frac{\mathcal{R}_1}{\hat{\mathcal{R}}_1} + \sum_{t=2}^n y_t \log \frac{\mathcal{R}_t}{\hat{\mathcal{R}}_t} - \sum_{t=1}^n \eta_t (\mathcal{R}_t - \hat{\mathcal{R}}_t) \right) \\
&= \sum_{y_n=0}^{\infty} \frac{(\eta_n \mathcal{R}_n)^{y_n} e^{-\eta_n \mathcal{R}_n}}{y_n!} \left(\sum_{t=1}^{n-1} \eta_t \mathcal{R}_t \log \frac{\mathcal{R}_t}{\hat{\mathcal{R}}_t} + y_n \log \frac{\mathcal{R}_n}{\hat{\mathcal{R}}_n} - \sum_{t=1}^n \eta_t (\mathcal{R}_t - \hat{\mathcal{R}}_t) \right) \\
&= \sum_{t=1}^n \eta_t \left(\mathcal{R}_t \log \frac{\mathcal{R}_t}{\hat{\mathcal{R}}_t} + \hat{\mathcal{R}}_t - \mathcal{R}_t \right),
\end{aligned}$$

where

$$\begin{aligned}
& \sum_{y_1=0}^{\infty} \frac{(\eta_1 \mathcal{R}_1)^{y_1} e^{-\eta_1 \mathcal{R}_1}}{y_1!} \left(y_1 \log \frac{\mathcal{R}_1}{\hat{\mathcal{R}}_1} + \sum_{t=2}^n y_t \log \frac{\mathcal{R}_t}{\hat{\mathcal{R}}_t} - \sum_{t=1}^n \eta_t (\mathcal{R}_t - \hat{\mathcal{R}}_t) \right) \\
&= \left(\sum_{y_1=0}^{\infty} \frac{(\eta_1 \mathcal{R}_1)^{y_1-1} e^{-\eta_1 \mathcal{R}_1}}{(y_1-1)!} \eta_1 \mathcal{R}_1 \log \frac{\mathcal{R}_1}{\hat{\mathcal{R}}_1} \right) + \sum_{t=2}^n y_t \log \frac{\mathcal{R}_t}{\hat{\mathcal{R}}_t} - \sum_{t=1}^n \eta_t (\mathcal{R}_t - \hat{\mathcal{R}}_t) \\
&= \eta_1 \mathcal{R}_1 \log \frac{\mathcal{R}_1}{\hat{\mathcal{R}}_1} + \sum_{t=2}^n y_t \log \frac{\mathcal{R}_t}{\hat{\mathcal{R}}_t} - \sum_{t=1}^n \eta_t (\mathcal{R}_t - \hat{\mathcal{R}}_t).
\end{aligned}$$

We use mean KL divergence (denoted, $\overline{D_{KL}}(\mathcal{R}||\hat{\mathcal{R}}) := D_{KL}(\mathcal{R}||\hat{\mathcal{R}})/n$, which is the KL divergence divided by the sequence length) in experiments for accuracy comparison.

A.2 Supplementary details on experimental settings

We compare the accuracy of the estimated effective reproduction numbers using the mean Kullback Leibler (KL) divergence (with Poisson distributional assumption on incidence) in (10) across our **RtEstim** and several alternative methods including **EpiEstim** with weekly and monthly sliding windows, **EpiLPS**, **EpiFilter**, **EpiNow2**, and **RtEstim** with degrees $k=0,1,2,3$, which yields 9 methods in total. We consider two lengths of epidemics with $n = 50$ or $n = 300$ timepoints respectively. Since **EpiNow2** runs too long (specifically, for a long **measles** epidemic, it takes almost 2 hours (115 minutes computed on Cedar cluster provided by Compute Canada), we only compare it with other methods for short epidemics.

We consider serial interval (SI) distributions of **measles** and **SARS** to generate long synthetic epidemics, and **flu** for short epidemics, inspired by Cori et al. (2013). The means and standard deviations of SI distributions are estimated by existing literatures; specifically, (14.9, 3.9) for **measles** (Groendyke, Welch, and Hunter (2011)), (8.4, 3.8) for **SARS** (Lipsitch et al. (2003)), and (2.6, 1.5) for **flu** (Ferguson et al. (2005), Boëlle et al. (2011)). Incident cases in synthetic **measles** epidemics are relatively low (within 1000 at the peak overall), and **SARS** incident cases are relatively large (between 15000 and 20000 at the peak overall). We consider a reasonably large overdispersion level of negative Binomial incidence with size 5. Figure A.2.1 displays the ratio of standard deviation over mean (called, sigma to mean ratio) of incidence across different settings using the same set of sample epidemics in Fig 5, Fig 6, and all figures in section A.6.1. Compared to the counterpart of Poisson incidence (which decreases quickly to 0 and remains to be under 0.25) per \mathcal{R}_t scenario for each epidemic, the negative Binomial incidence appears to have an apparently larger sigma to mean ratio (staying at around 0.5 or above), which implies a distinguishable overdispersion level.

In model fitting, we use both true and misspecified serial interval (SI) distributions to test the robustness of our method, compared to other alternatives. The misspecification of serial interval distributions are either mild or major, where, in the major misspecification, we use a completely different pair of SI parameters, e.g., we use SI of **SARS** to solve measles epidemics, and SI of measles to solve short **flu** epidemics. While, in the mild SI misspecification, we consider slightly adjusted parameters for both **measles** and **flu** epidemics, where the mean is decreased by 2 for **measles** and increased by 2 for **flu** and the standard deviation is increased by 10, denoted as **adj_flu** and **adj_measles** respectively. These settings result in 7 pairs of SI distributions (for epidemic generating, model fitting), i.e., (**measles**, **measles**), (**SARS**, **SARS**), (**measles**, **adj_measles**), (**measles**, **SARS**) for long epidemics and (**flu**, **flu**), (**flu**, **adj_flu**), (**flu**, **measles**) for short

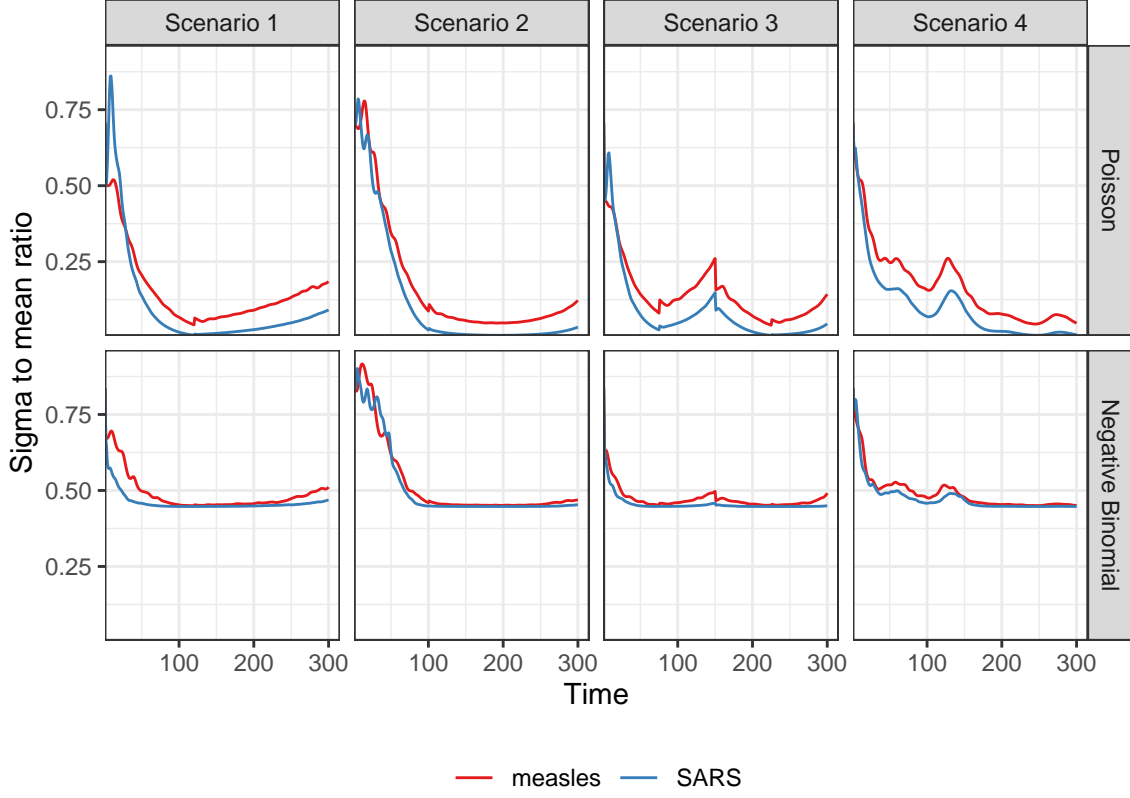


Figure A.2.1: Dispersion level of incidence of sample epidemics

Table 1: Summary of experimental setting on accuracy comparison

Length	SI	Rt scenario	Incidence	SI for modelling	Method
300	measles	1-4	Poisson, NB	measles, adj_measles, SARS	8 methods
300	SARS	1-4	Poisson, NB	SARS	8 methods
50	flu	3	Poisson, NB	flu, adj_flu, measles	9 methods

epidemics. Figure A.2.2 displays all SI distributions (`measles`, `adj_measles`, `SARS`, `flu`, and `adj_flu`) used in the experiments.

Table 1 summarizes the aforementioned experimental setting for accuracy comparison. Poisson and negative Binomial (NB) distributions for incidence and 4 \mathcal{R}_t scenarios are used for all long epidemics. We only consider one \mathcal{R}_t scenario for short epidemics. Each experimental setting is replicated for 50 times, which yields 12800 experiments for long epidemics and 2700 for short epidemics.

We visualize the selected key results of the accuracy comparison using long synthetic epidemics in Section 3.2. Other main experimental results are displayed in Section A.3.

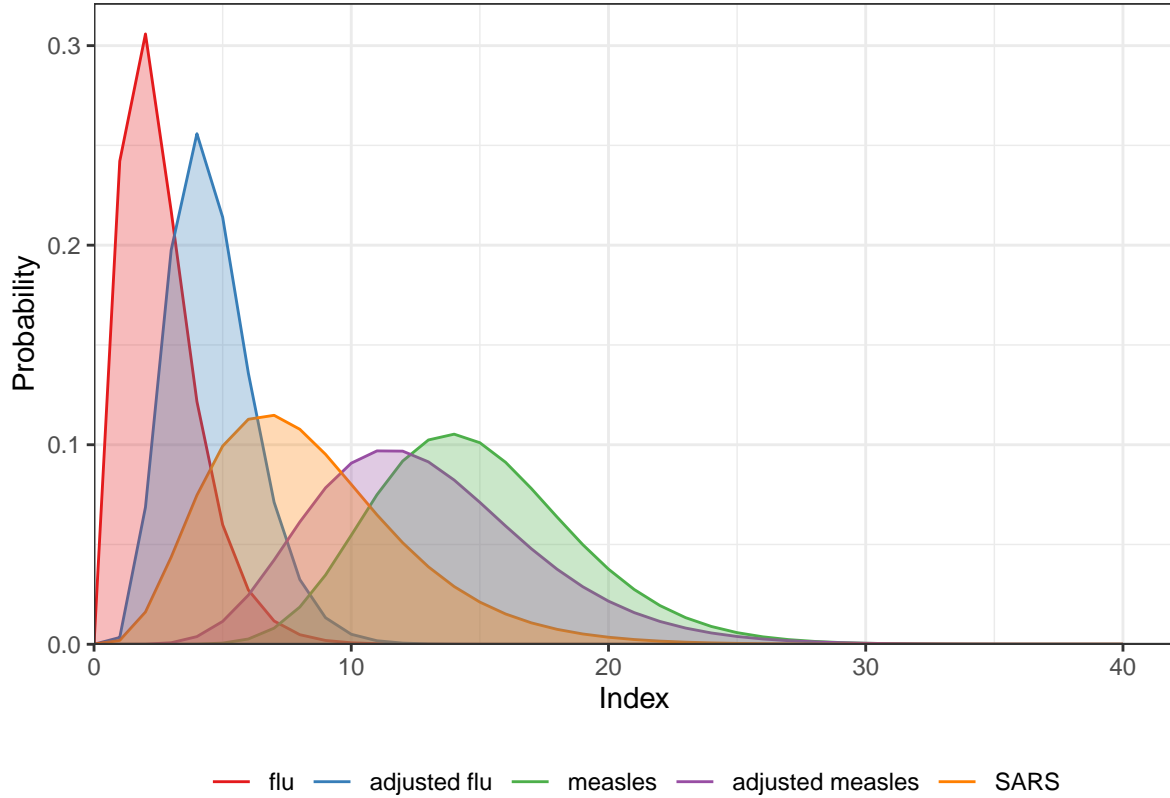


Figure A.2.2: Density curves of serial interval distributions used in the experiments

A.3 Supplementary experimental results on accuracy comparison

A.3.1 Long epidemics

We display the accuracy of all methods (where **EpiEstim** uses weekly sliding window) for measles and SARS sample epidemics (by excluding the first weeks in computing KL divergence) in Fig 3 and Fig 4, where we exclude the outliers. A full visualization is in A.3.1.

Figure A.3.2 compares **EpiEstim** with *monthly* sliding windows with other methods. We average the KL divergence per coordinate excluding the timepoints in the first months for all approaches, since **EpiEstim** estimates with the monthly sliding windows are not available until the second months. The *y*-axis is displayed on a logarithmic scale for a better visualization, since a few values are much larger than others.

The relative performance of **EpiEstim** with monthly sliding windows, in general, is not as good as its weekly sliding window based on the relative positions of its boxes and the counterparts of the other methods, except for the Scenario 2 with negative Binomial incidence. It can be explained by **EpiEstim** with longer sliding windows assume similarity of neighbouring \mathcal{R}_t across longer periods, and thus, is smoother and less accurate compared to the one with shorter sliding windows.

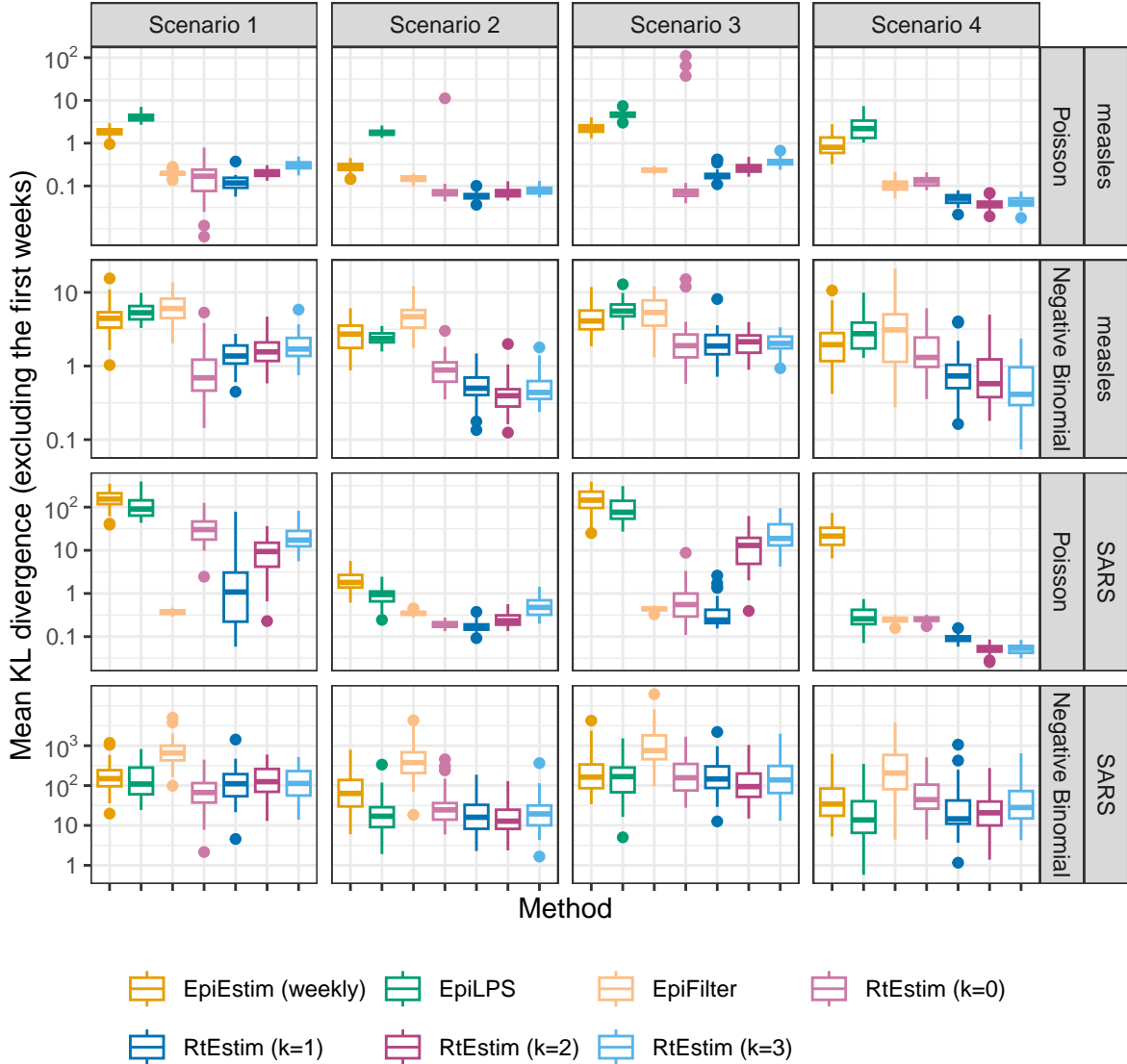


Figure A.3.1: Mean KL divergence excluding the first weeks for measles and SARS epidemics, since EpiEstim with the weekly sliding window does not provide estimates for the first week. Y-axis is on a logarithmic scale.

A.3.2 Short epidemics

Figures A.3.3 and A.3.4 display the KL divergence for short epidemics aggregated over per coordinate excluding the first weeks and months respectively.

A.4 Experimental results on accuracy under misspecification of serial interval distributions

A.4.1 SI misspecification for long epidemics

Figures A.4.1 and A.4.2 display KL divergence (excluding first weeks and months respectively) for all 8 methods with mild misspecification (shaped and scaled **measles** SI parameters) and major misspecification

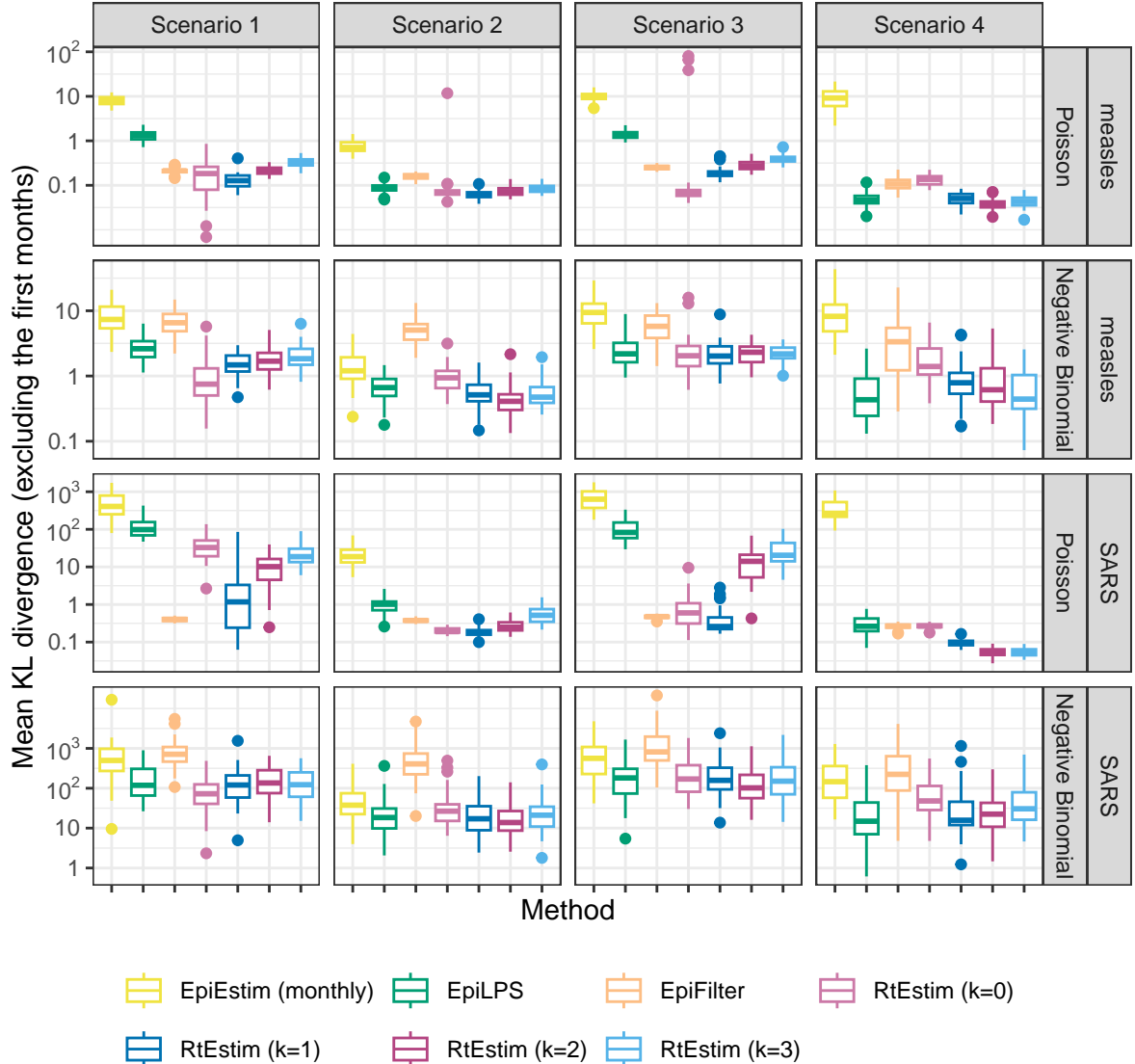


Figure A.3.2: Mean KL divergence excluding the first months for measles and SARS epidemics, since EpiEstim with the monthly sliding window does not provide estimates for the first month. Y-axis is on a logarithmic scale.

(SARS SI parameters) for long `measles` epidemics across all settings.

A.4.2 SI misspecification for short epidemics

Figures A.4.3 and A.4.4 display KL divergence (excluding first weeks and months respectively) for all 9 methods with minor misspecification (shaped and scaled `flu` SI parameters) and major misspecification (measles parameters) for short `flu` epidemics across all settings.

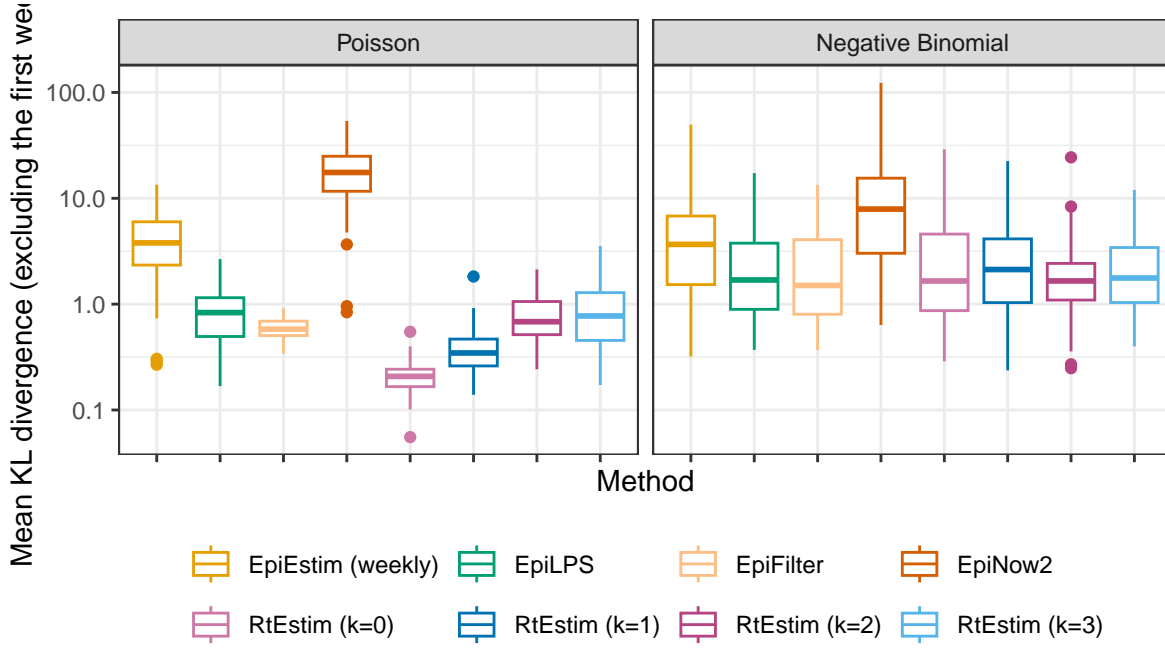


Figure A.3.3: Mean KL divergence excluding the first weeks for flu epidemics, since EpiEstim with the weekly sliding window does not provide estimates for the first week. Y-axis is on a logarithmic scale.

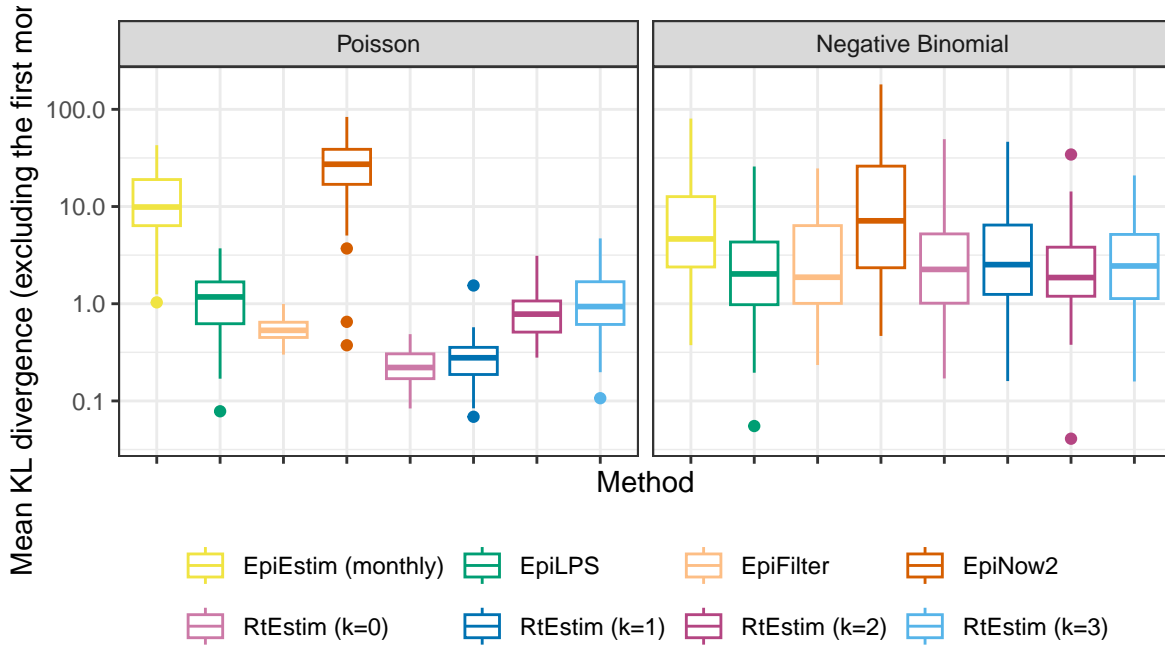


Figure A.3.4: Mean KL divergence excluding the first months for flu epidemics, since EpiEstim with the monthly sliding window does not provide estimates for the first month. Y-axis is on a logarithmic scale.

A.5 Time comparisons of all methods

Figures A.5.1 show the time comparisons across all methods for long (measles and SARS) epidemics. **EpiEstim** with both weekly and monthly sliding windows are very fast and converge in less than 0.1 seconds. Piecewise

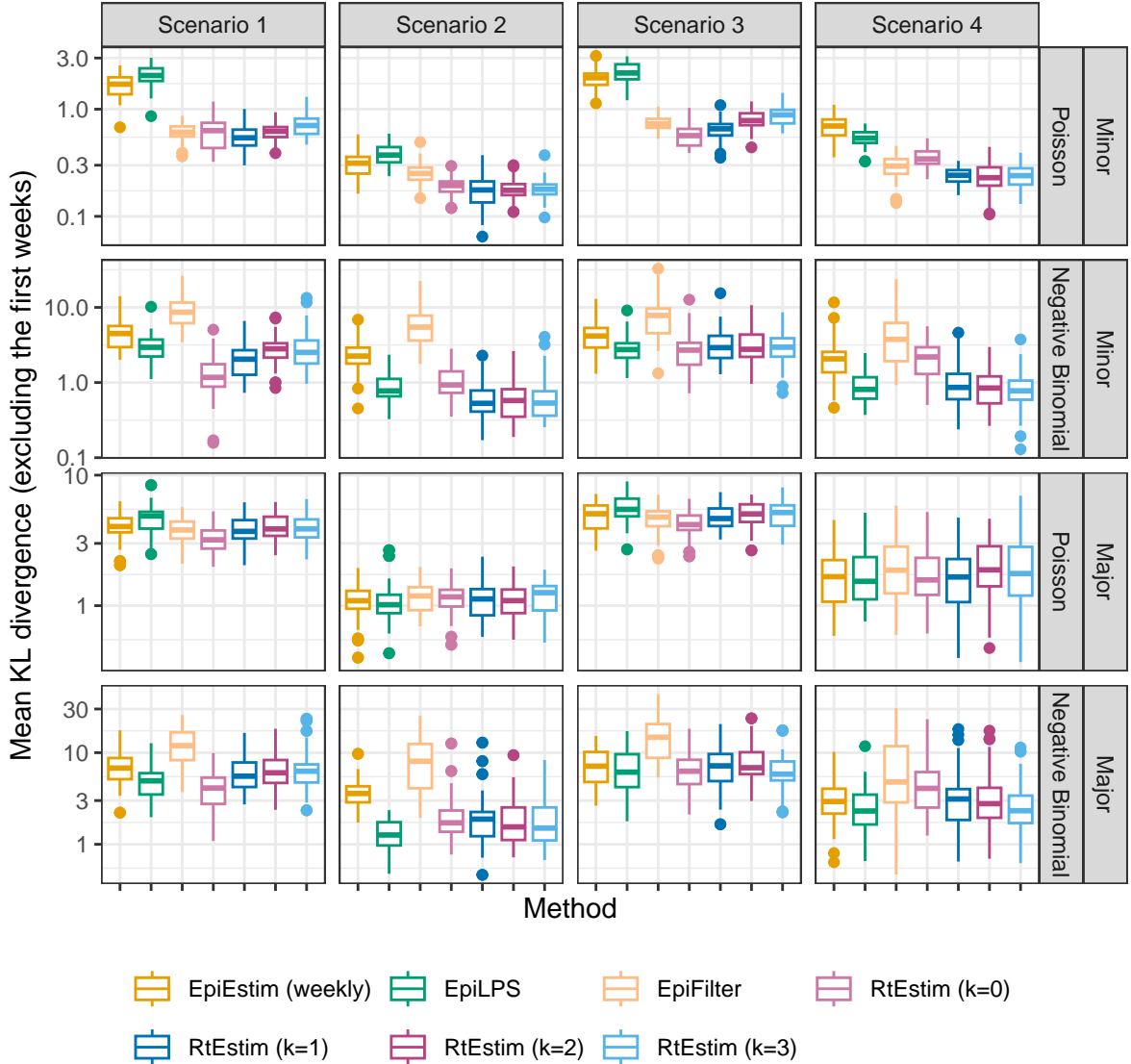


Figure A.4.1: Mean KL divergence excluding the first weeks for measles epidemics with SI misspecification, since EpiEstim with the weekly sliding window does not provide estimates for the first week. Y-axis is on a logarithmic scale.

constant **RtEstim** (with $k=0$) estimates can be generated within 0.1 seconds as well. **EpiLPS** is slightly slower, but still very fast and within 1 second for all experiments. Piecewise linear and cubic **RtEstim** (with $k = 1$ and $k = 3$ respectively) are slower, but mostly within 10 seconds.

It is remarkable that our **RtEstim** computes 50 lambda values with 10-fold CV for each experiment, which results in 550 times of modelling per experiment (including modelling for all folds). The running times are no more than 10 seconds for most of the experiments, which means the running time for each time of modelling is very fast, and on average can be less than 0.02 seconds. The other two methods only run once for a fixed set of hyperparameters for each experiment.

We visualize the running times of each case in separate panels in Figures A.5.2 and A.5.3 for measles and SARS epidemics respectively. Similar results as in Figure A.5.1 are found in each setting.

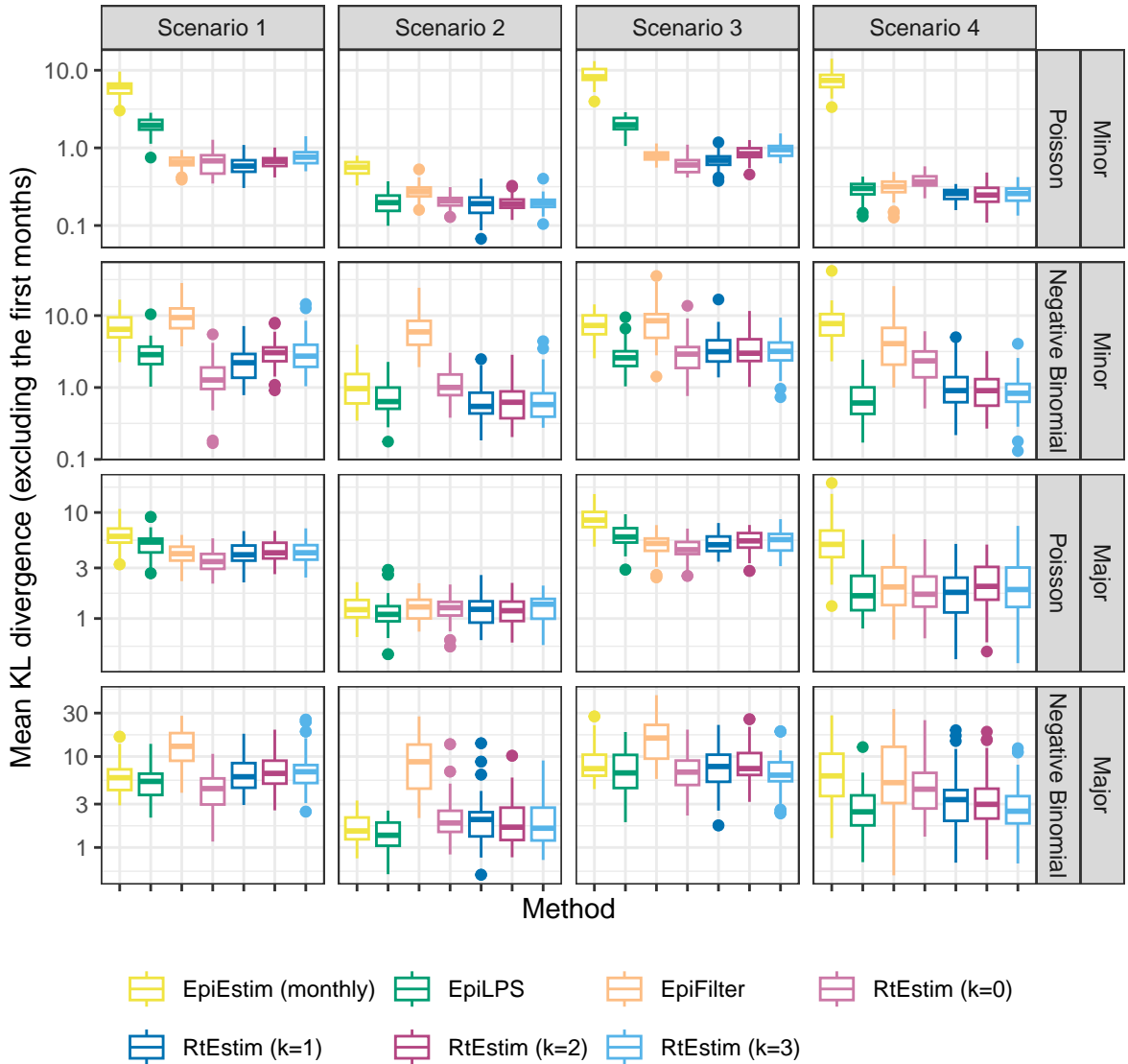


Figure A.4.2: Mean KL divergence excluding the first months for measles epidemics with SI misspecification, since EpiEstim with the monthly sliding window does not provide estimates for the first month. Y-axis is on a logarithmic scale.

Figure A.5.4 displays the running times of all methods for short (flu) epidemics. Figure A.5.5 displays the running times for each setting separately, and finds similar results as in the overall running time comparison.

A.6 Confidence interval coverage

A.6.1 Display estimates and confidence intervals for sample epidemics

Let's take a clearer view of the estimated \mathcal{R}_t with 95% confidence intervals for the sample long epidemics by all methods in Fig 5 and Fig 6 in Figures A.6.1 and A.6.4 respectively. The full view of other example epidemics are visualized in Figures A.6.2 and A.6.3 as follows.

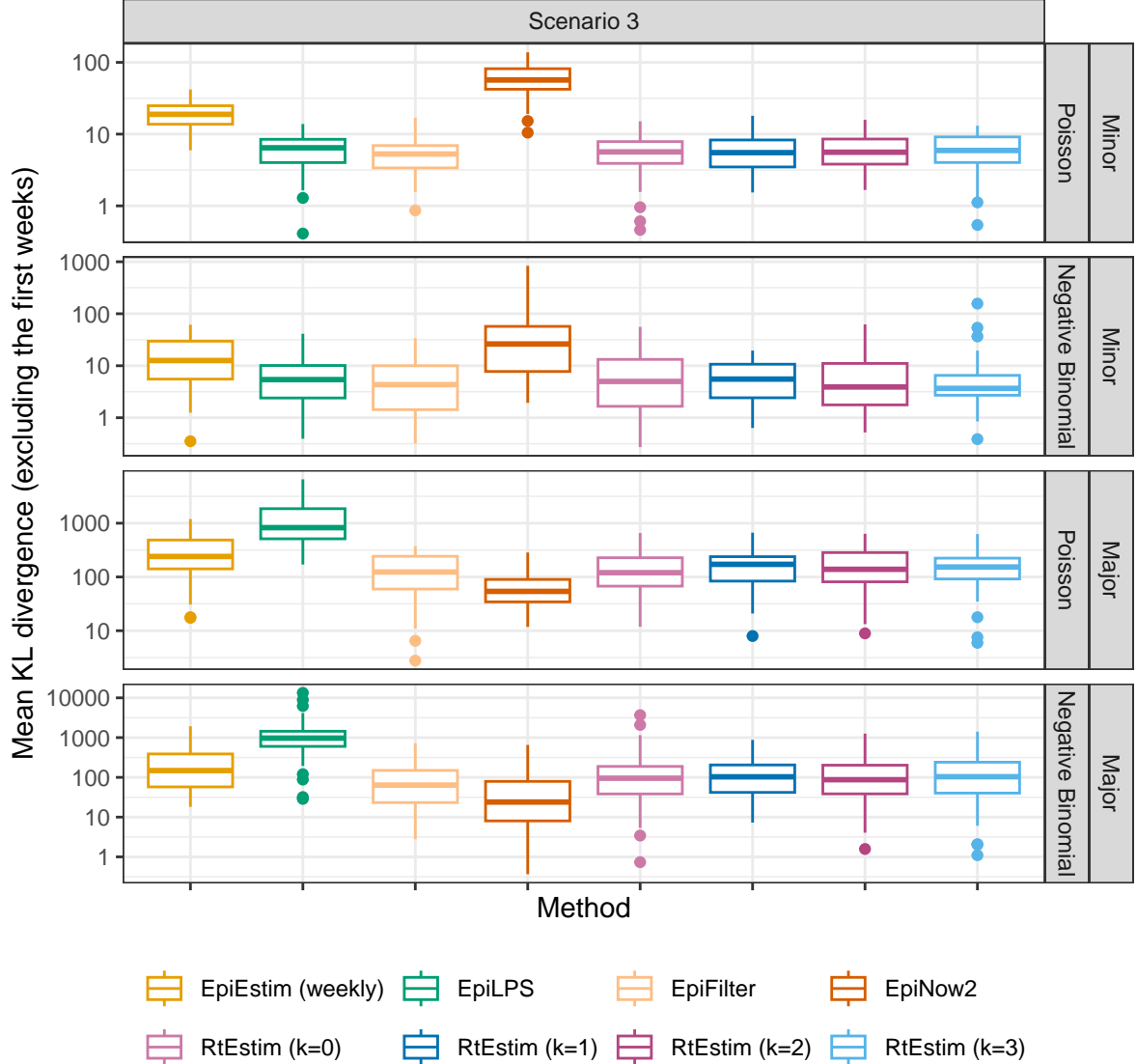


Figure A.4.3: Mean KL divergence excluding the first weeks for flu epidemics with SI misspecification, since EpiEstim with the weekly sliding window does not provide estimates for the first week. Y-axis is on a logarithmic scale.

A.6.2 Experimental settings on coverage level comparison of confidence intervals

We focus on a specific \mathcal{R}_t scenario, the piecewise linear case, and only long epidemics to compare the coverage of 95% confidence intervals across all 8 methods. We use the true serial interval distributions in modelling. Table 2 summarizes the experimental settings.

A.6.3 Experimental results on interval coverage comparison

Figures A.6.5 and A.6.6 displays the percentages of coverage of 95% CI per coordinate over 50 random samples for measles and SARS epidemics respectively.

Figures A.6.7 and A.6.8 displays the percentages of coverage of 95% CI across all timepoints averaged over 50 random measles and SARS epidemics respectively.

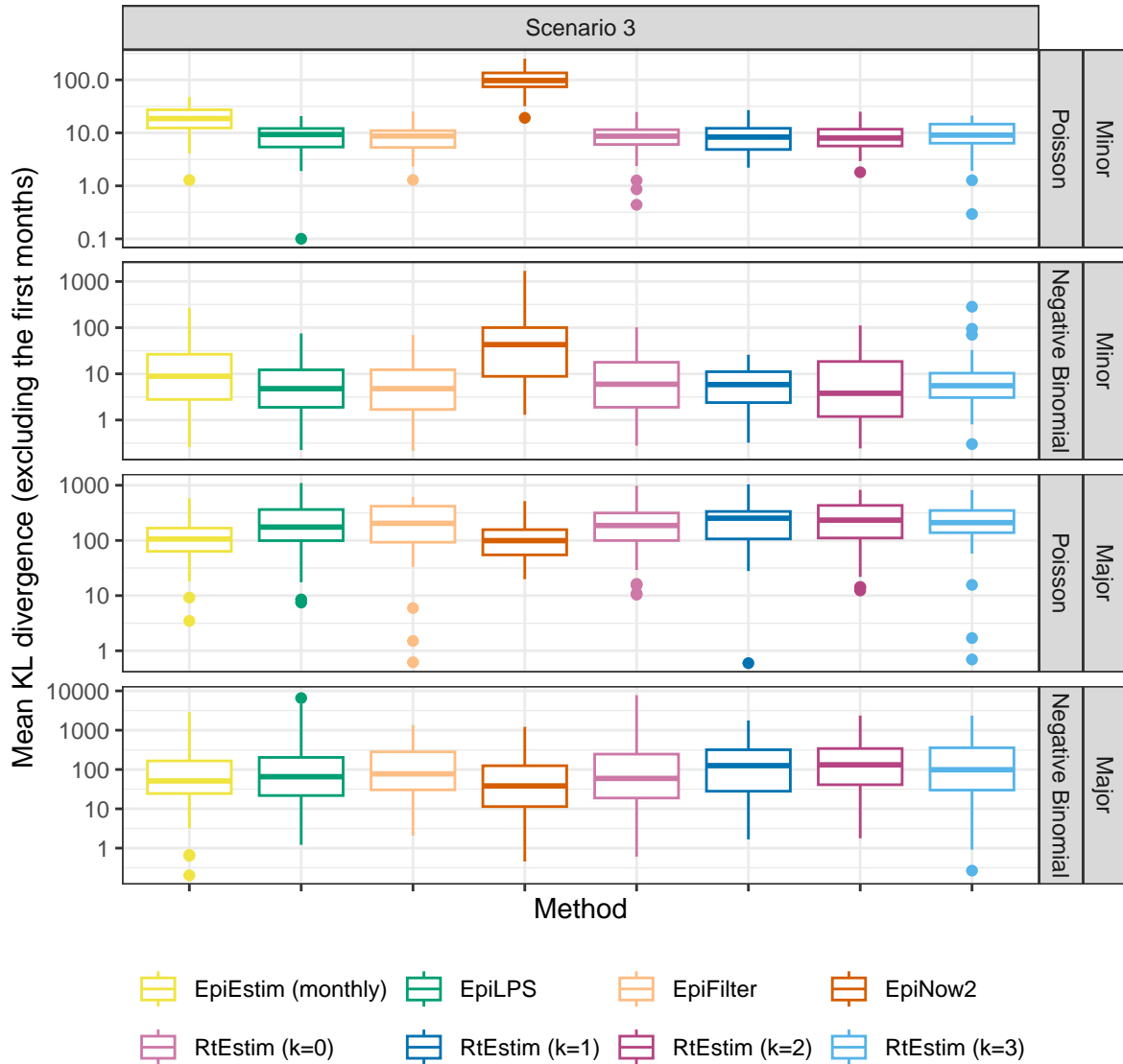


Figure A.4.4: Mean KL divergence excluding the first months for flu epidemics with SI misspecification, since EpiEstim with the monthly sliding window does not provide estimates for the first month. Y-axis is on a logarithmic scale.

We output a vector of the CI coverage for each timepoint per experiment, the percentage of coverage of all timepoints, and the interval score

$$score_{\alpha}(\mathcal{R}, u, l) = \frac{1}{n} \sum_{t=1}^n (u_t - l_t) + \frac{2}{\alpha} (l_t - \mathcal{R}_t) \mathbf{1}_{(\mathcal{R}_t < l_t)} + \frac{2}{\alpha} (\mathcal{R}_t - u_t) \mathbf{1}_{(\mathcal{R}_t > u_t)}$$

, where $\alpha = 0.05$ is the significance level, l, u are the lower and upper bounds, \mathcal{R}_t is the true effective reproduction number, and $\mathbf{1}_X$ is the indicator function of the condition X . (Bracher et al. 2021). Figures A.6.9 and A.6.10 displays the interval scores of 95% CI averaged over 50 random measles and SARS epidemics respectively.

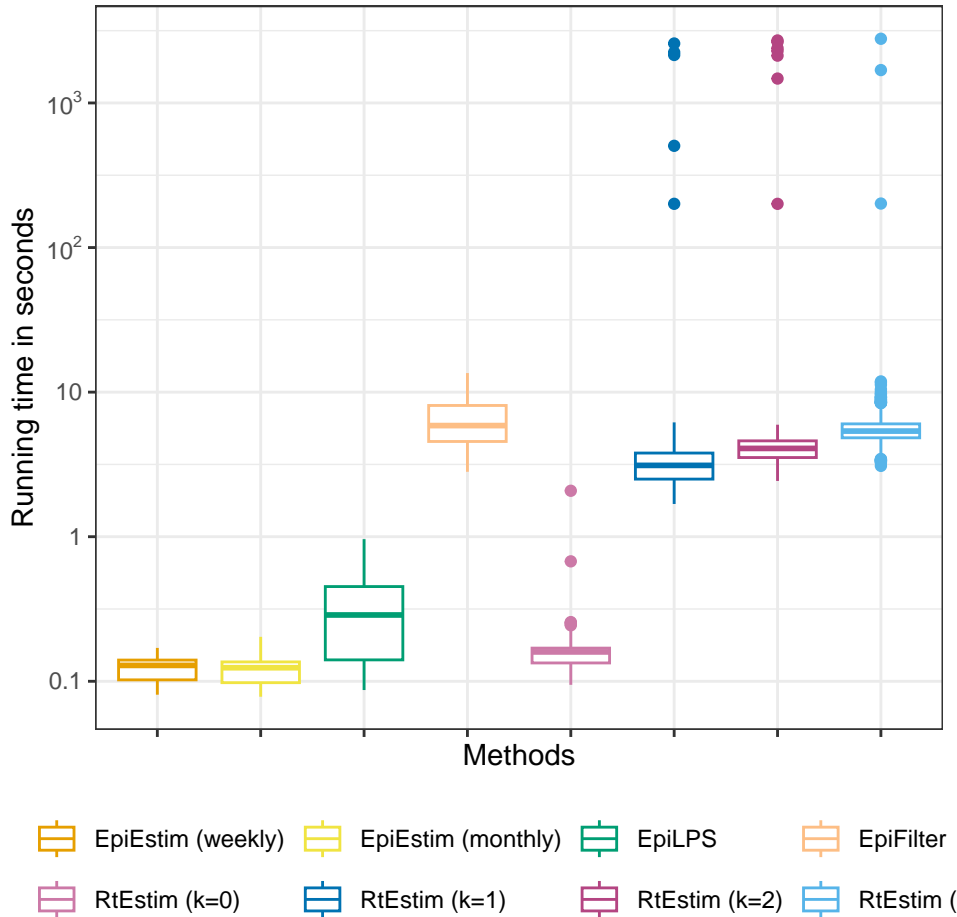


Figure A.5.1: Time comparisons of all methods for long (measles and SARS) epidemics across all cases. Y-axis is on a logarithmic scale.

A.7 Data examples and alternative visualizations of Figs 5 and 6

A.7.1 More visualization of example epidemics

We generate measles and SARS epidemics using Poisson and negative Binomial incidence distributions for each experimental settings. The condensed display of estimates for measles with Poisson incidence and SARS with negative Binomial incidence are provided in Fig 5 and Fig 6. A full visualization of each case is provided in Section A.6.1. The condensed visualization of other cases is provided below in Figures A.7.1 and A.7.2.

Table 2: Summary of experimental setting on coverage of confidence intervals

Length	SI	Rt scenario	Incidence	SI for modelling	Method
300	measles		3	Poisson, NB	measles
300	SARS		3	Poisson, NB	SARS

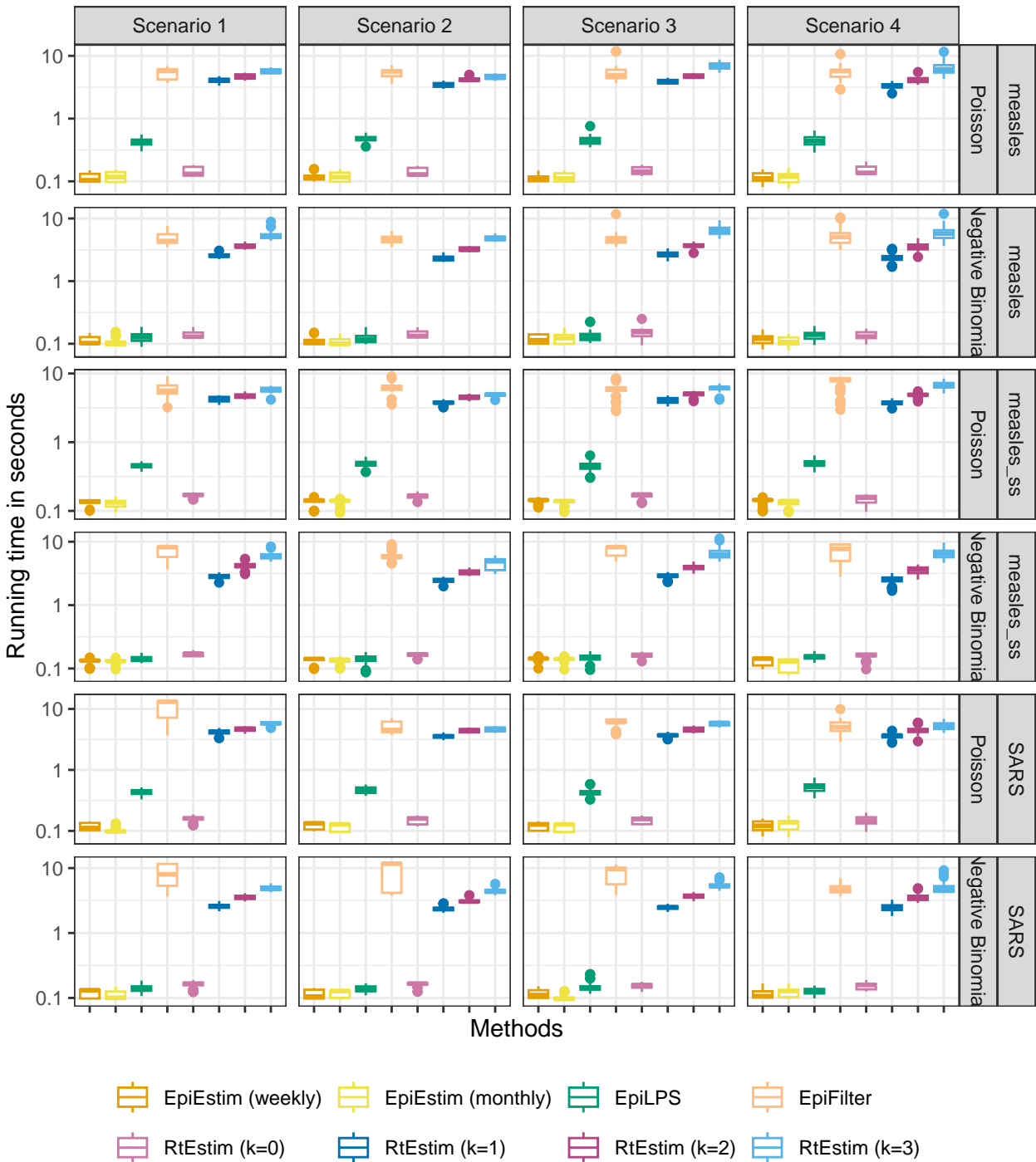


Figure A.5.2: Time comparisons of all methods for measles epidemics with each choice of SI parameter for modelling per incidence distribution per Rt scenario (excluding outliers for better illustration). Y-axis is on a logarithmic scale.

A.7.2 Alternative view of difference between fitted and true Rt estimates

Here, we also provide an alternative view of Fig 5 & Fig 6 by plotting $\mathcal{R}_t - \hat{\mathcal{R}}_t$ per coordinate t in A.7.3 and A.7.4 respectively. Figures A.7.5 and A.7.6 provide the alternative view of A.7.1 and A.7.2 respectively.

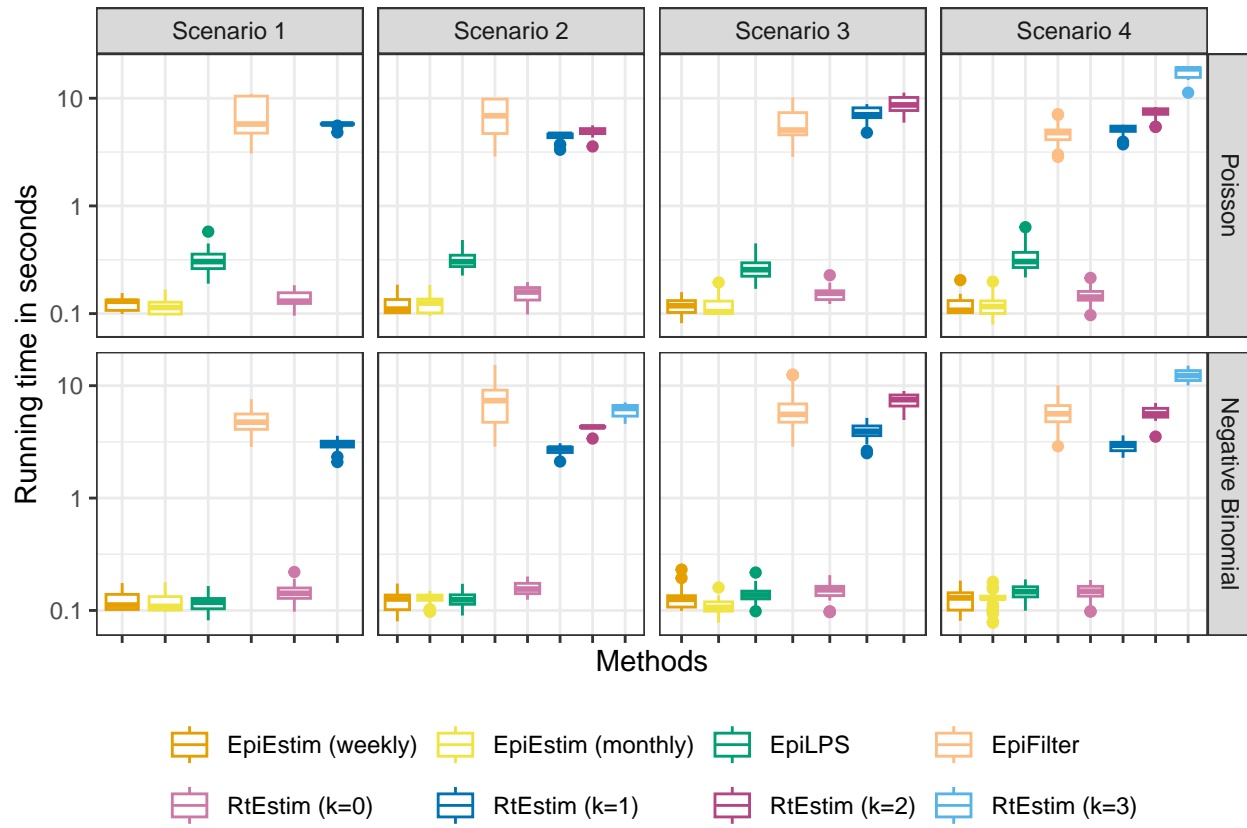


Figure A.5.3: Time comparisons of all methods for SARS epidemics with each choice of SI parameter for modelling per incidence distribution per Rt scenario (excluding outliers for better illustration). Y-axis is on a logarithmic scale.

A.8 Application of RtEstim and all competitors on real epidemics

We apply all methods on Covid19 incidence in BC, and the estimated are displayed in ???. An alternative display which plot all estimated curves in one panel for an easier comparison is provided in ???.

We also apply all methods on Flu in 1918 as well. The results are visualized in Figures A.8.3 and A.8.4.

Boëlle, Pierre-Yves, Severine Ansart, Anne Cori, and Alain-Jacques Valleron. 2011. “Transmission Parameters of the a/H1N1 (2009) Influenza Virus Pandemic: A Review.” *Influenza and Other Respiratory Viruses* 5 (5): 306–16.

Bracher, Johannes, Evan L. Ray, Tilmann Gneiting, and Nicholas G. Reich. 2021. “Evaluating Epidemic Forecasts in an Interval Format.” Edited by Virginia E. Pitzer. *PLoS Computational Biology* 17 (2): e1008618. <https://doi.org/10.1371/journal.pcbi.1008618>.

Cori, Anne, Neil M Ferguson, Christophe Fraser, and Simon Cauchemez. 2013. “A New Framework and Software to Estimate Time-Varying Reproduction Numbers During Epidemics.” *American Journal of Epidemiology* 178 (9): 1505–12.

Ferguson, Neil M, Derek AT Cummings, Simon Cauchemez, Christophe Fraser, Steven Riley, Aronrag Meeyai, Sopon Iamsirithaworn, and Donald S Burke. 2005. “Strategies for Containing an Emerging Influenza Pandemic in Southeast Asia.” *Nature* 437 (7056): 209–14.

Groendyke, Chris, David Welch, and David R Hunter. 2011. “Bayesian Inference for Contact Networks Given

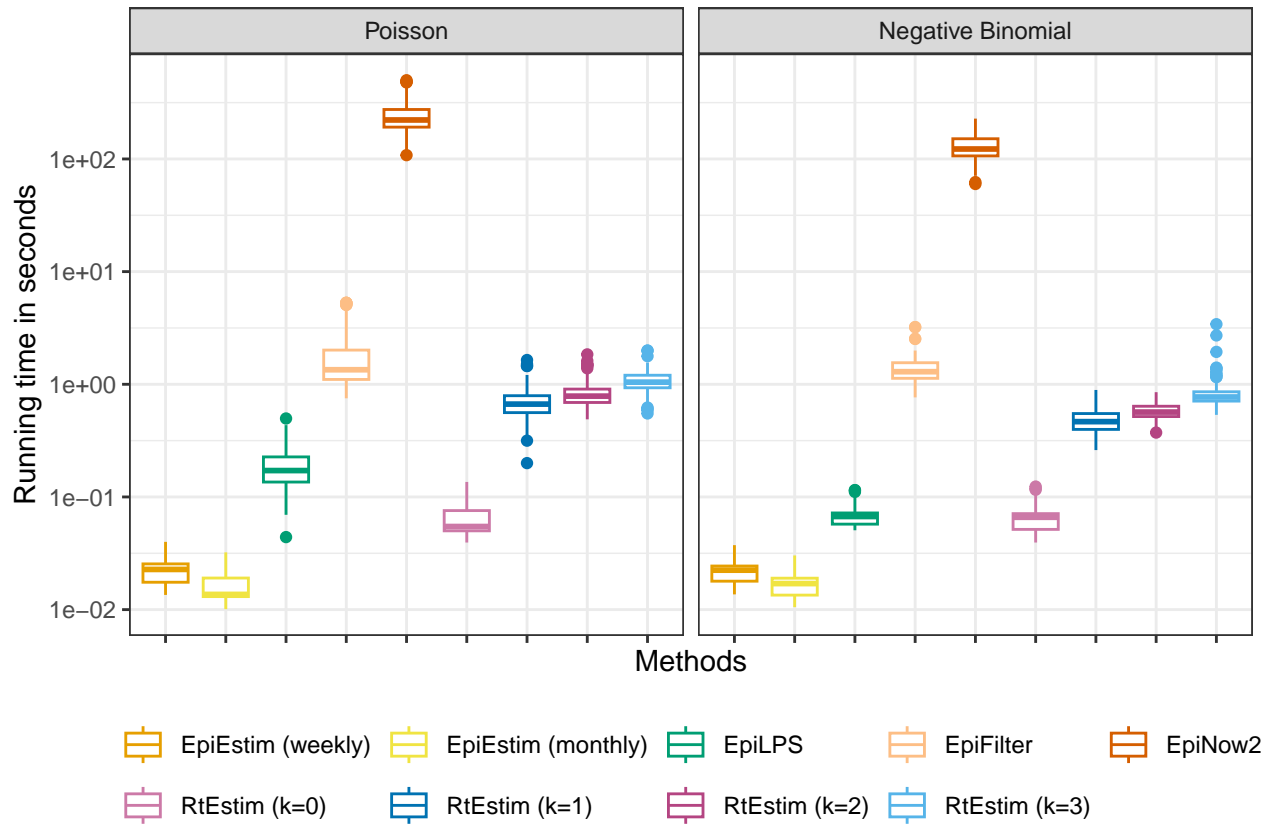


Figure A.5.4: Time comparisons of methods for short (flu) epidemics across all cases. Y-axis is on a logarithmic scale.

Epidemic Data.” *Scandinavian Journal of Statistics* 38 (3): 600–616.

Lipsitch, Marc, Ted Cohen, Ben Cooper, James M Robins, Stefan Ma, Lyn James, Gowri Gopalakrishna, et al. 2003. “Transmission Dynamics and Control of Severe Acute Respiratory Syndrome.” *Science* 300 (5627): 1966–70.

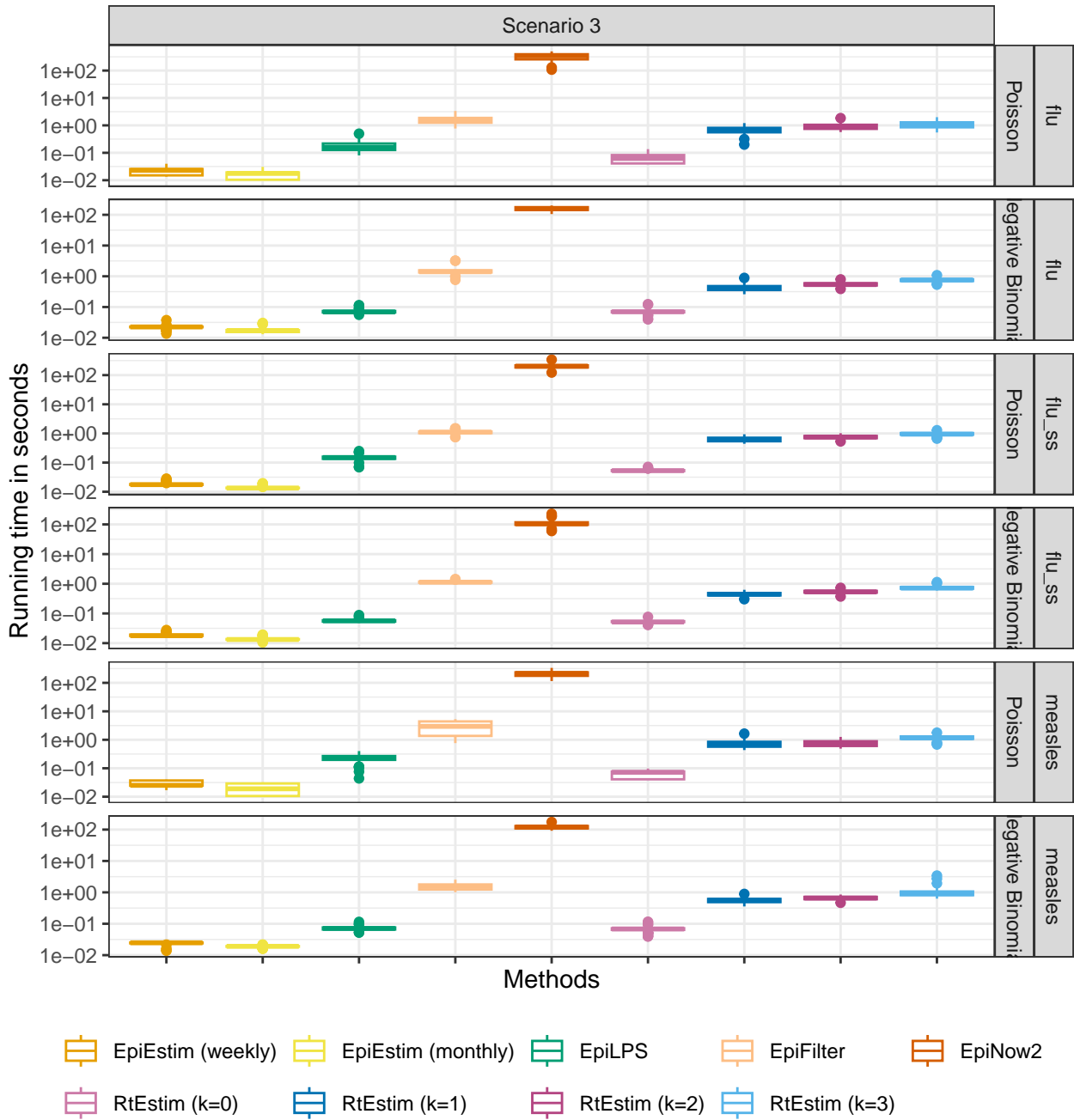


Figure A.5.5: Time comparisons of methods for short (flu) epidemics with different cases in different panels. Y-axis is on a logarithmic scale.

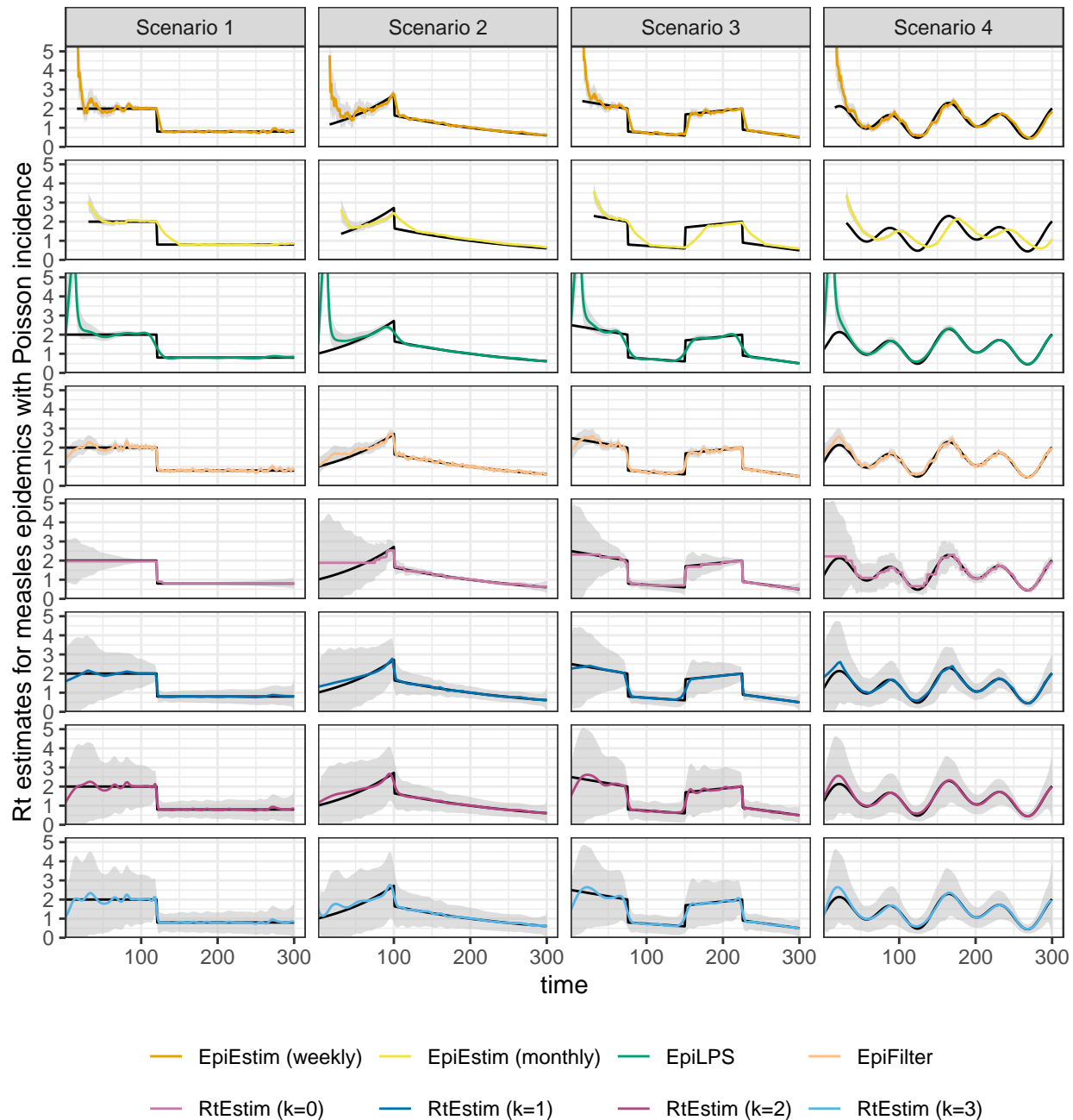


Figure A.6.1: Example measles epidemics with Poisson incidence.

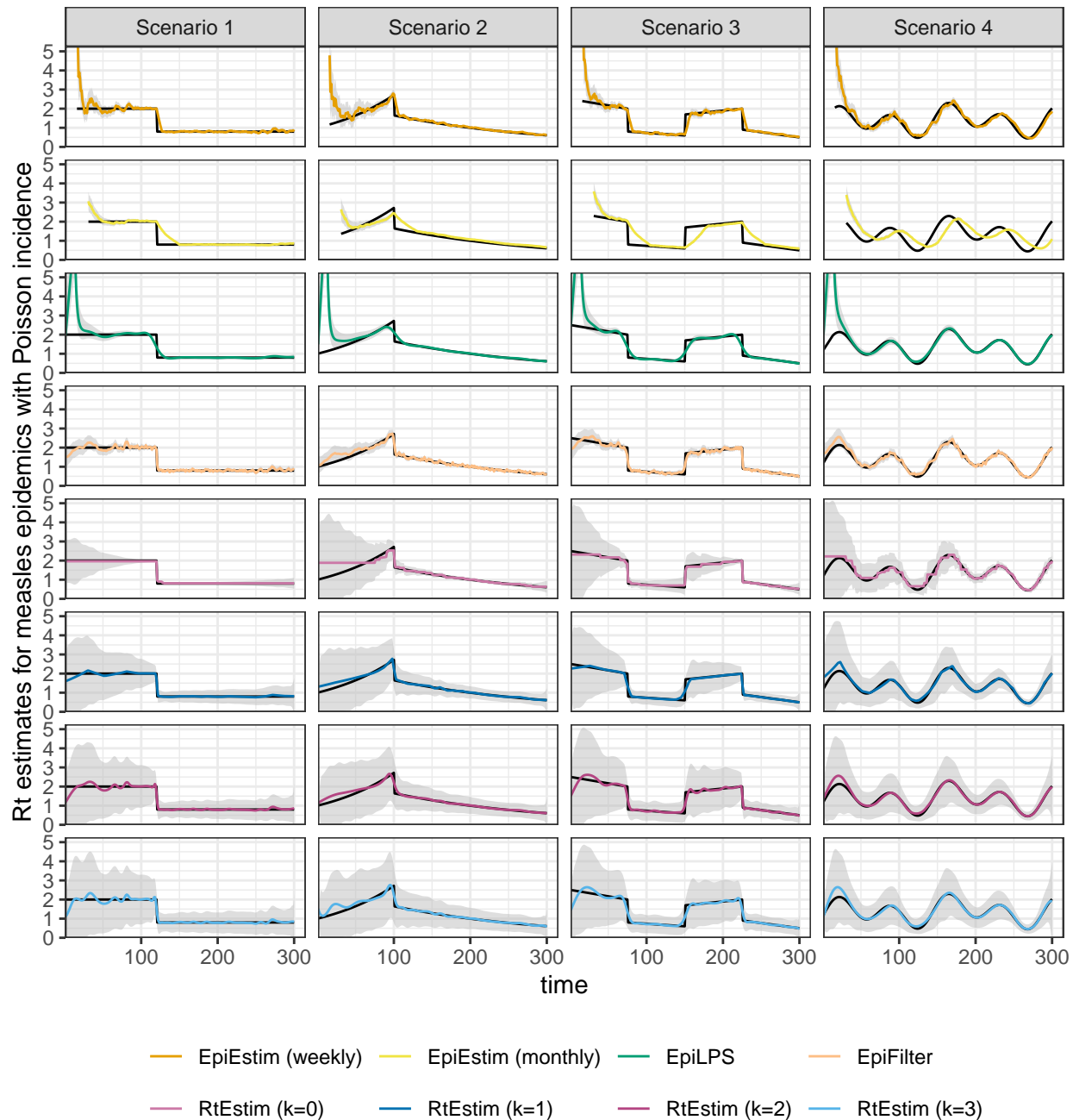


Figure A.6.2: Example measles epidemics with negative Binomial incidence.

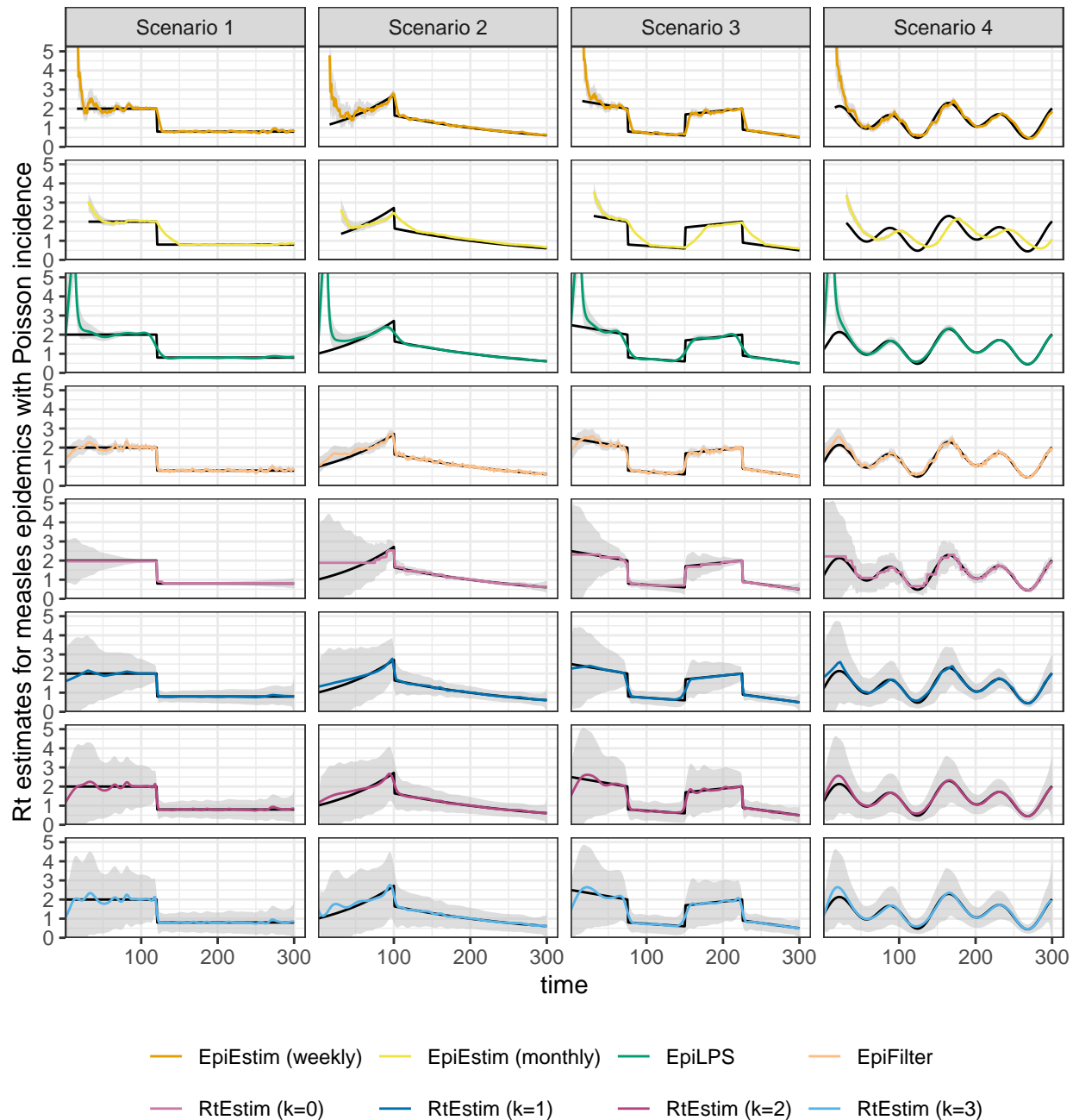


Figure A.6.3: Example SARS epidemics with Poisson incidence.

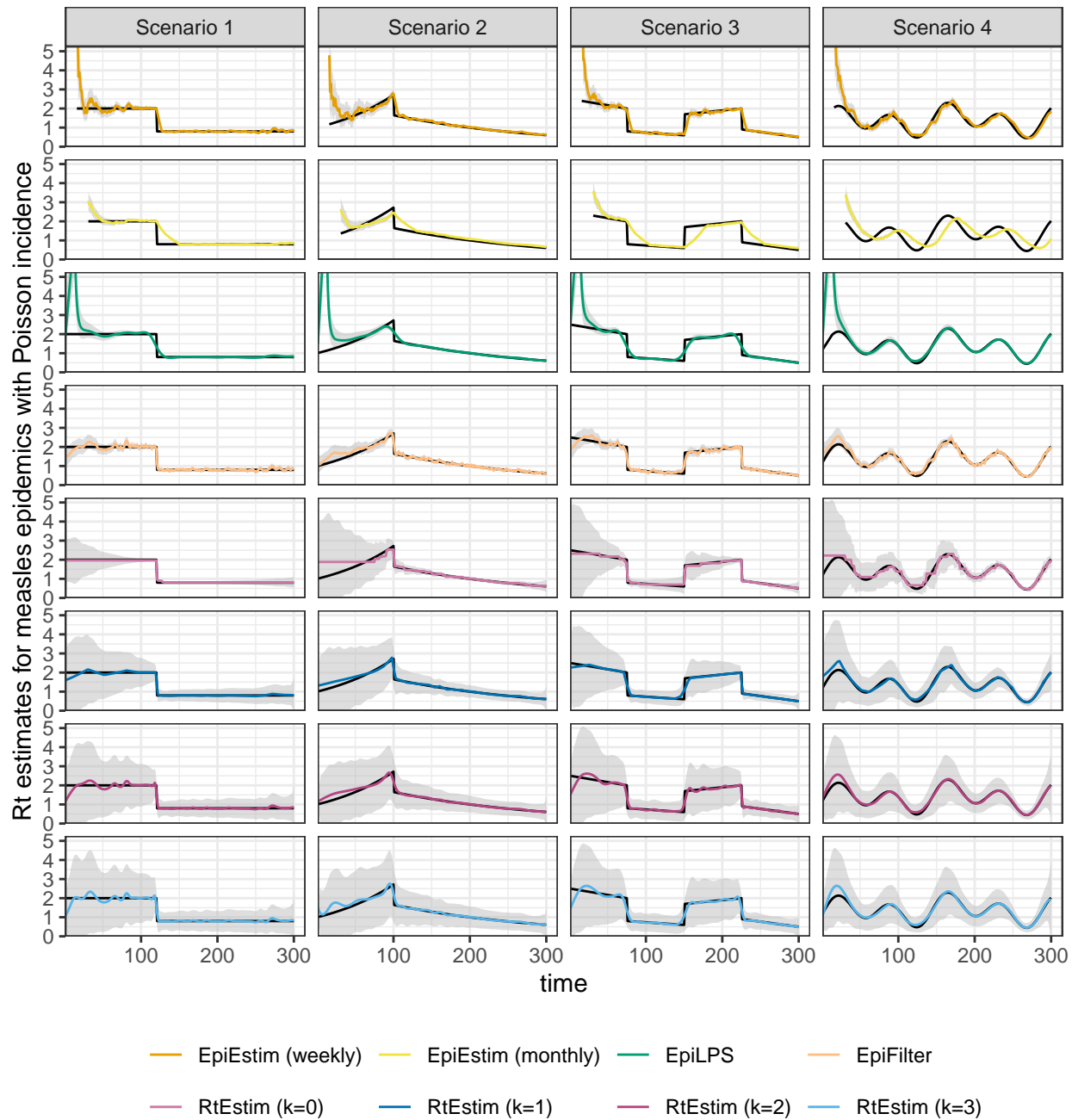


Figure A.6.4: Example SARS epidemics with negative Binomial incidence.

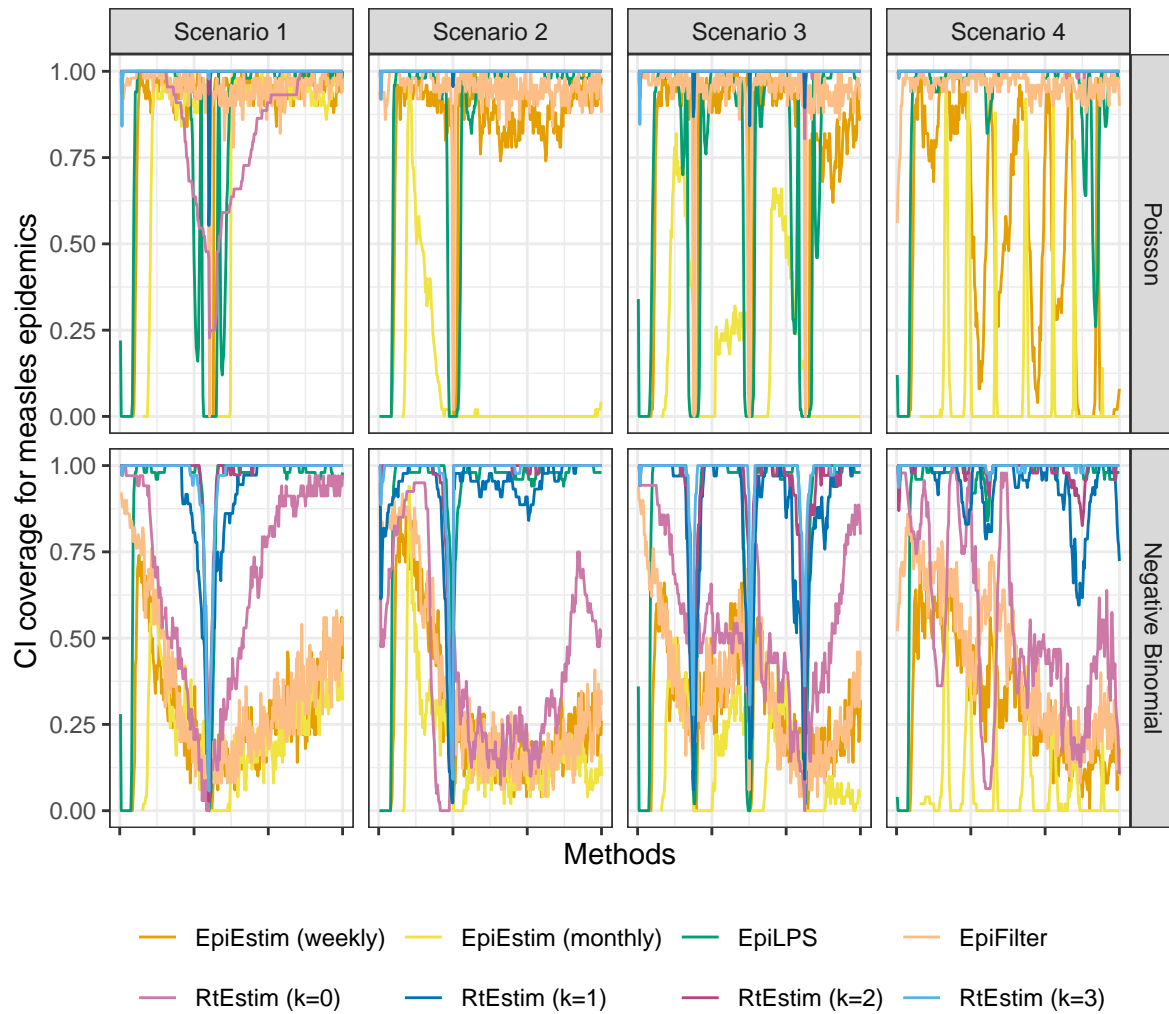


Figure A.6.5: Averaged coverage of CI per coordinate with measles epidemics.

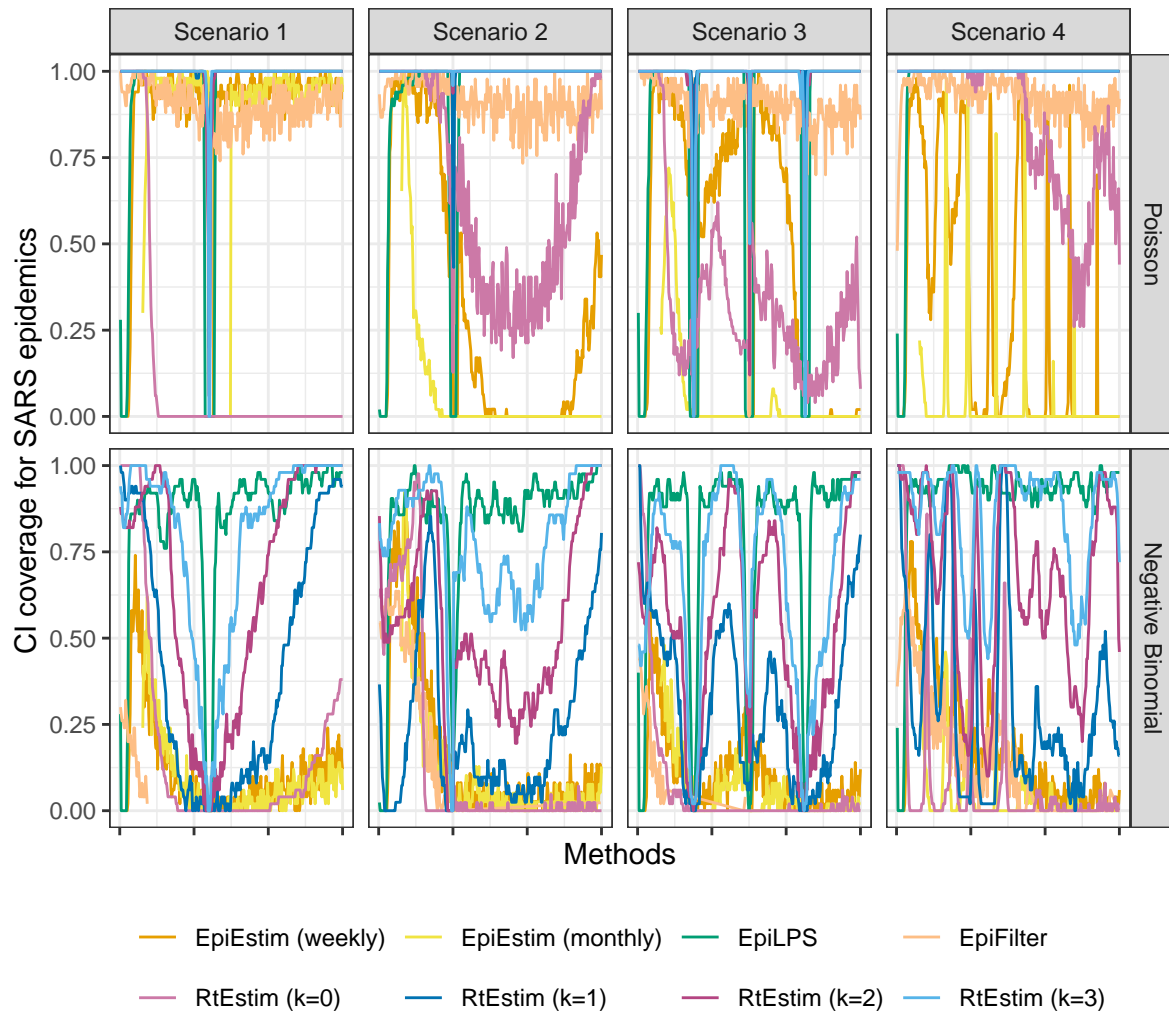


Figure A.6.6: Averaged coverage of CI per coordinate with SARS epidemics.

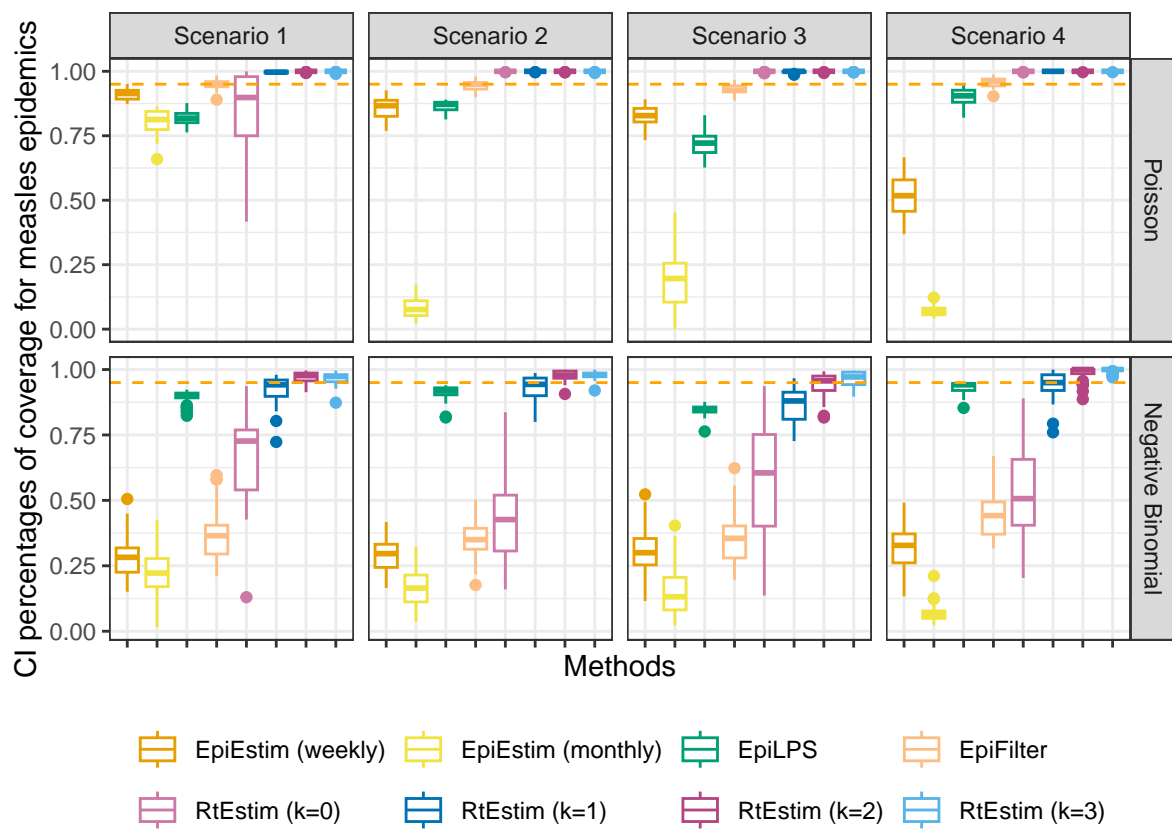


Figure A.6.7: Averaged percentages of CI coverage with measles epidemics.

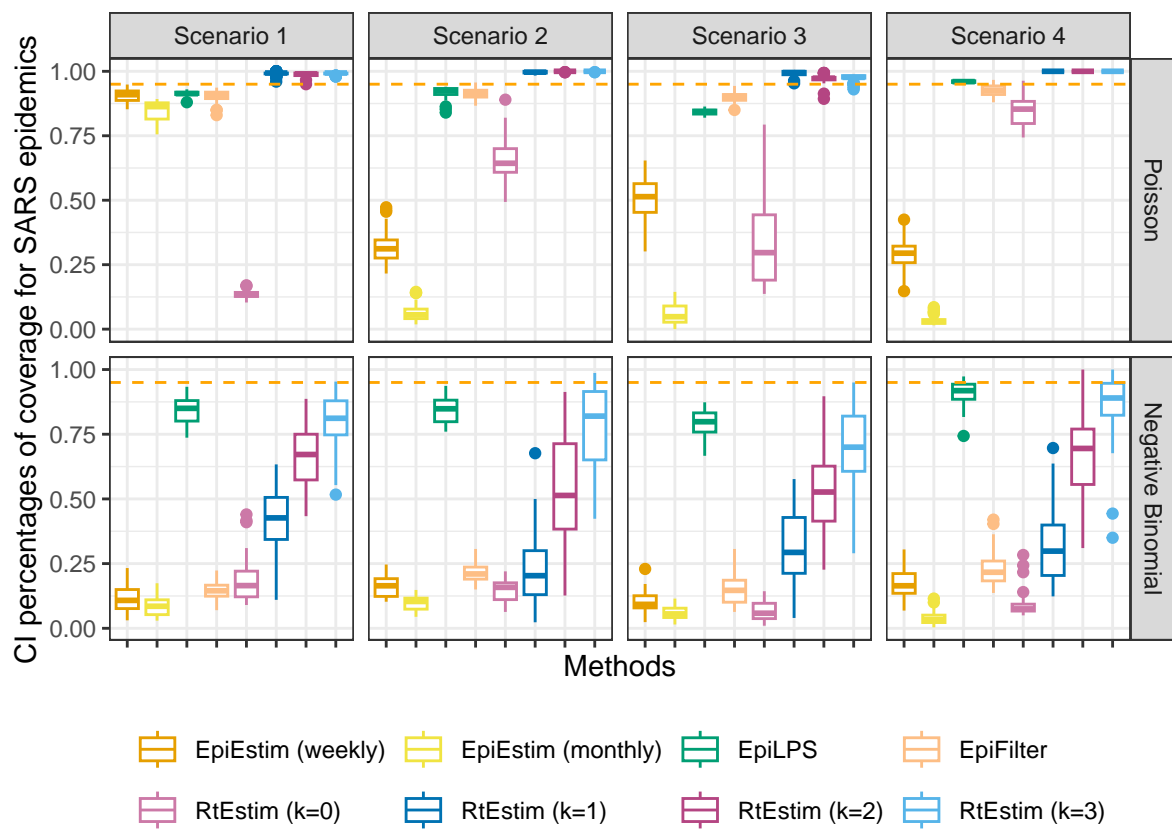


Figure A.6.8: Averaged percentages of CI coverage with SARS epidemics.

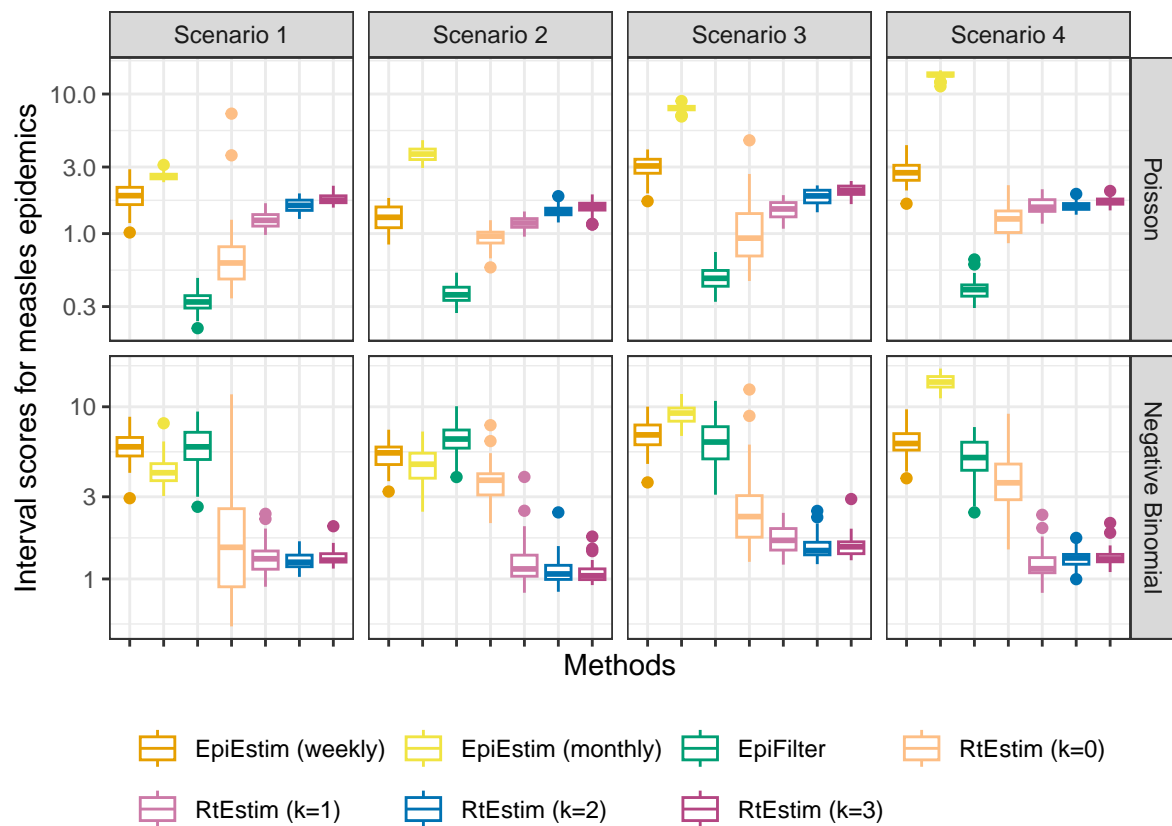


Figure A.6.9: Averaged interval scores with measles epidemics. EpiLPS is excluded, since it's scores are always larger than 100.

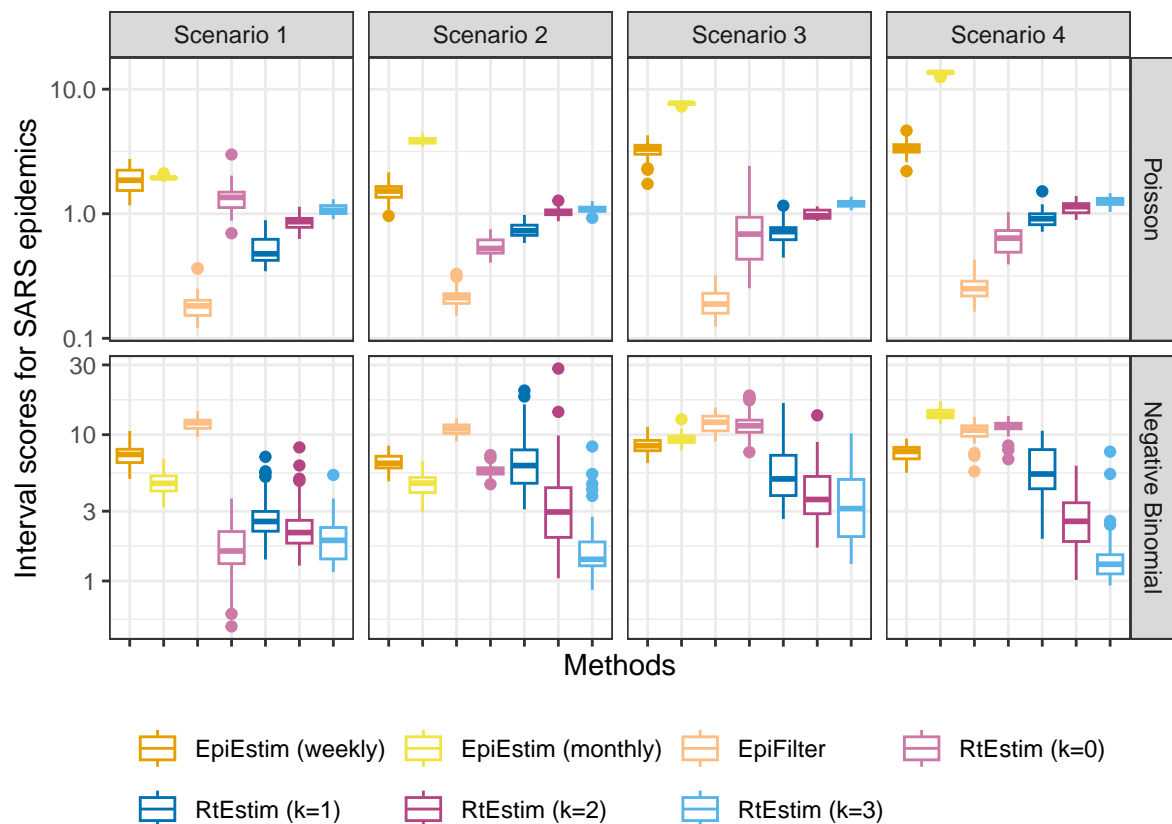


Figure A.6.10: Averaged interval scores with SARS epidemics. EpiLPS is excluded, since it's scores are always larger than 100.

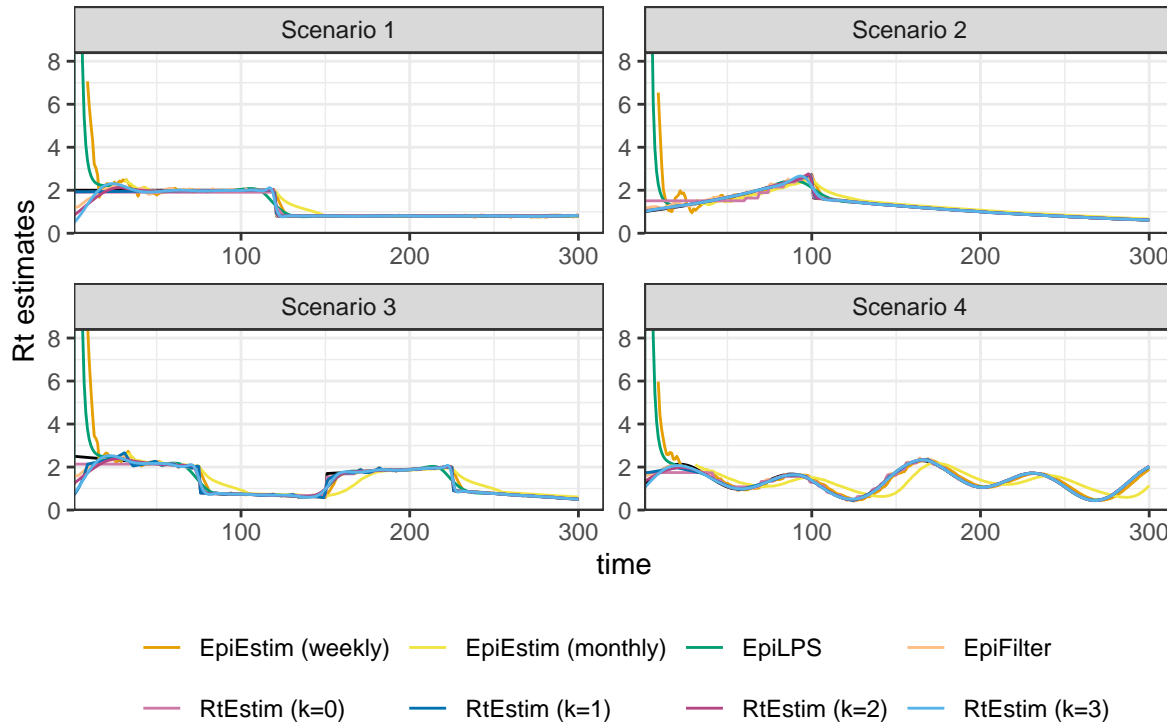


Figure A.7.1: Example of effective reproduction number estimation for SARS epidemics with Poisson observations.

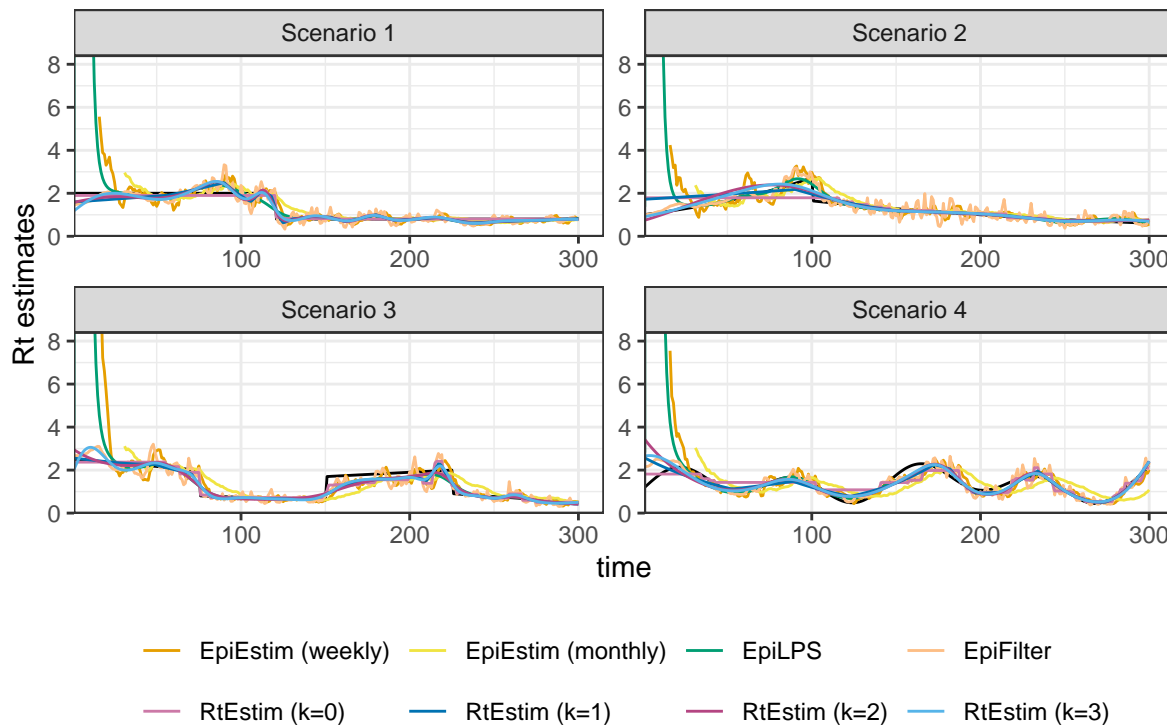


Figure A.7.2: Example of effective reproduction number estimation for measles epidemics with negative Binomial observations.

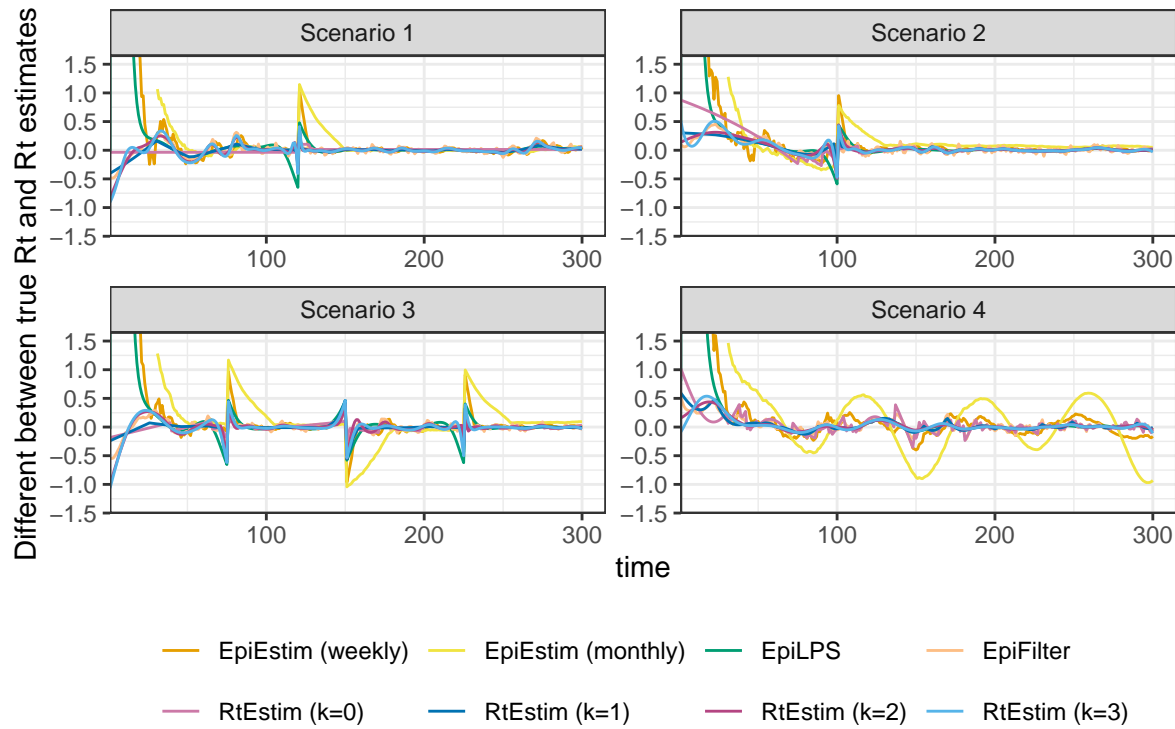


Figure A.7.3: Difference between of the true effective reproduction number and its estimation for measles epidemics with Poisson observations.

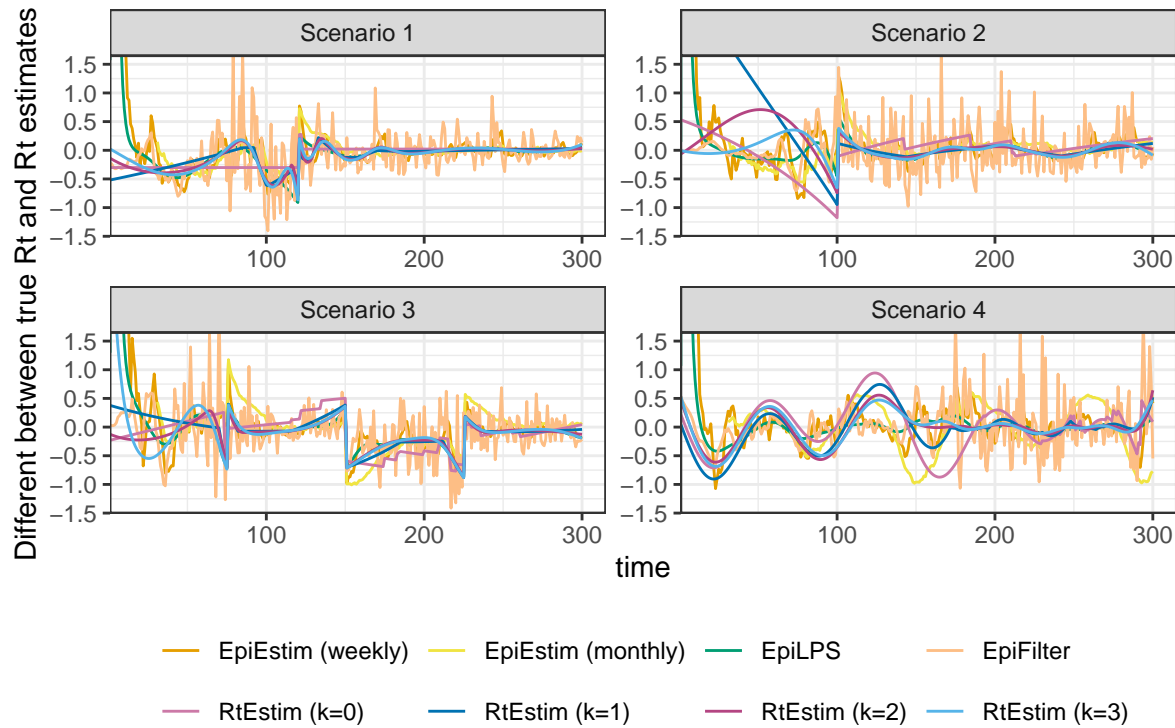


Figure A.7.4: Difference between of the true effective reproduction number and its estimation for SARS epidemics with negative Binomial observations.

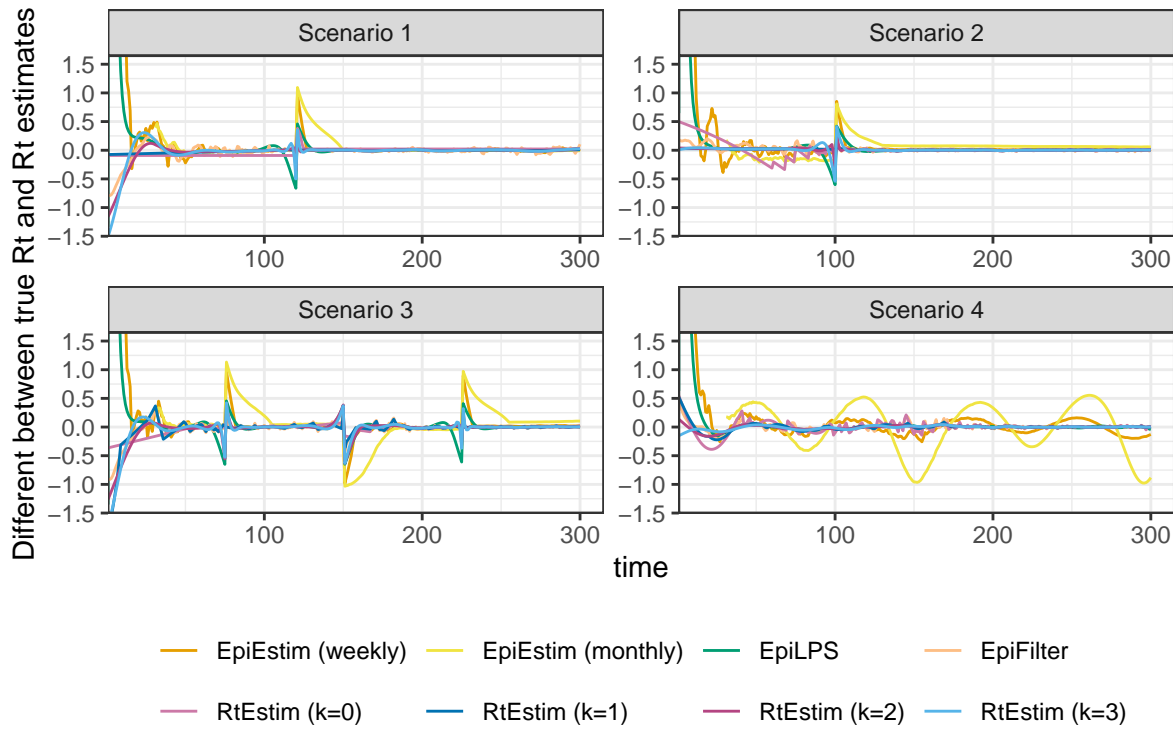


Figure A.7.5: Difference between of the true effective reproduction number and its estimation for SARS epidemics with Poisson observations.

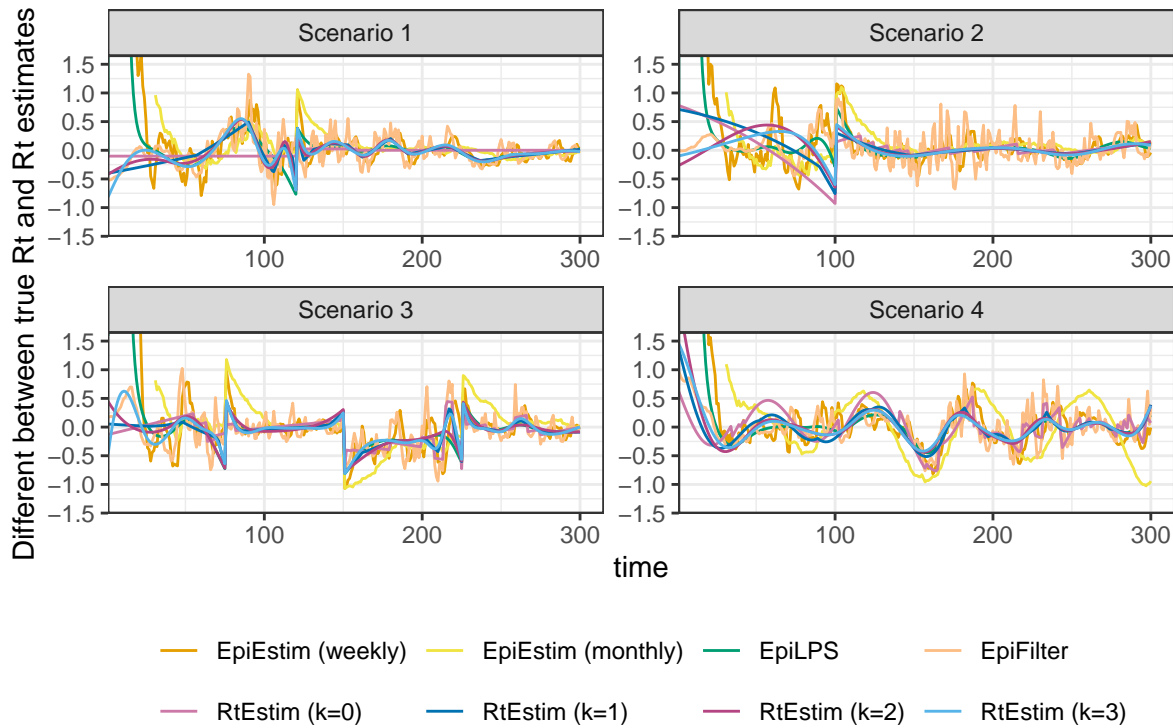


Figure A.7.6: Difference between of the true effective reproduction number and its estimation for measles epidemics with negative Binomial observations.

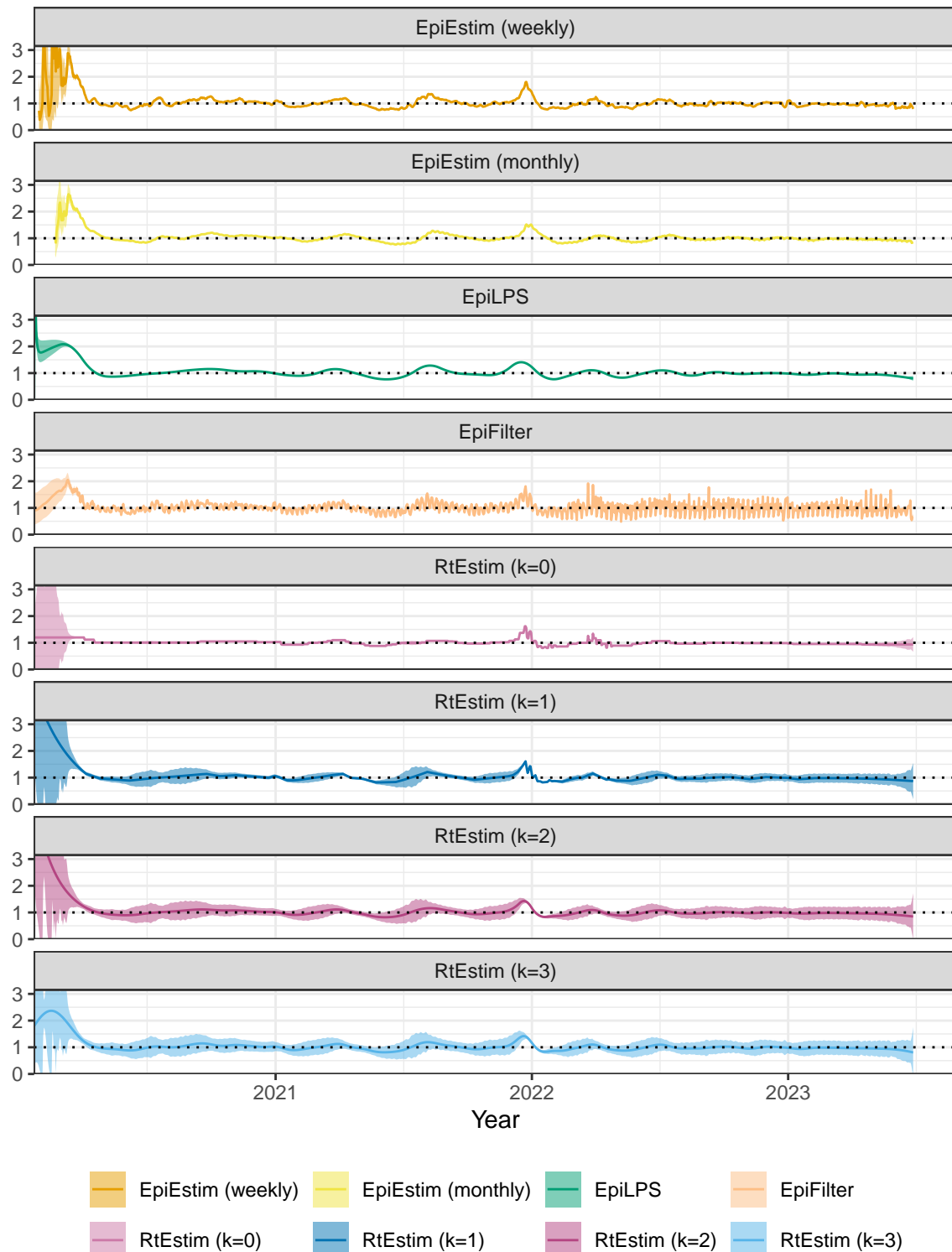


Figure A.8.1: Rt estimates with CIs for Covid19.

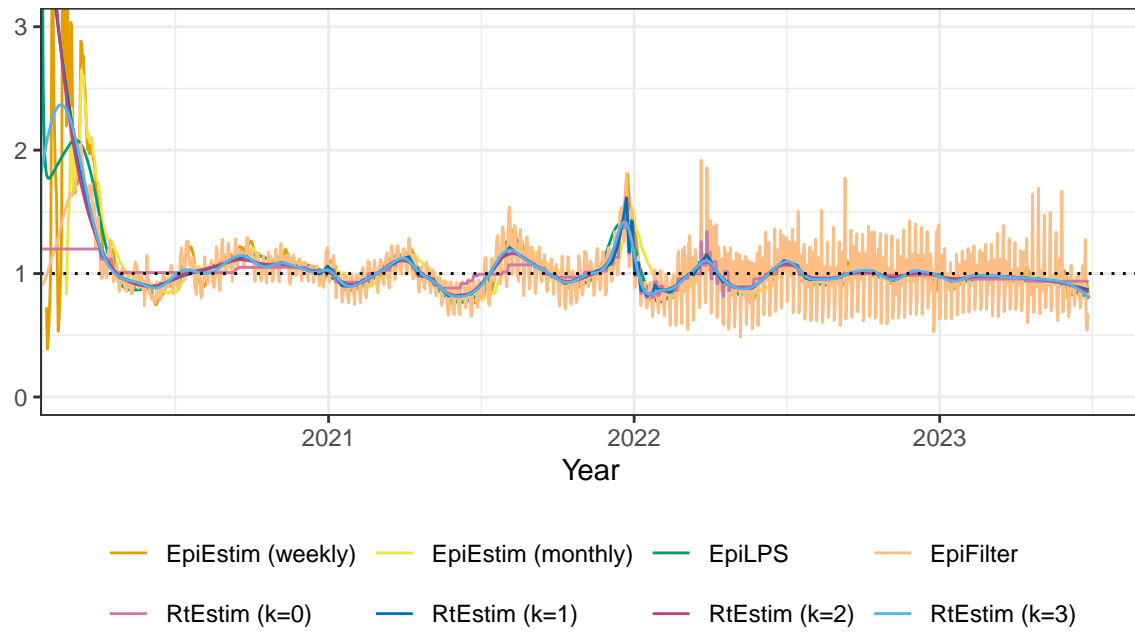
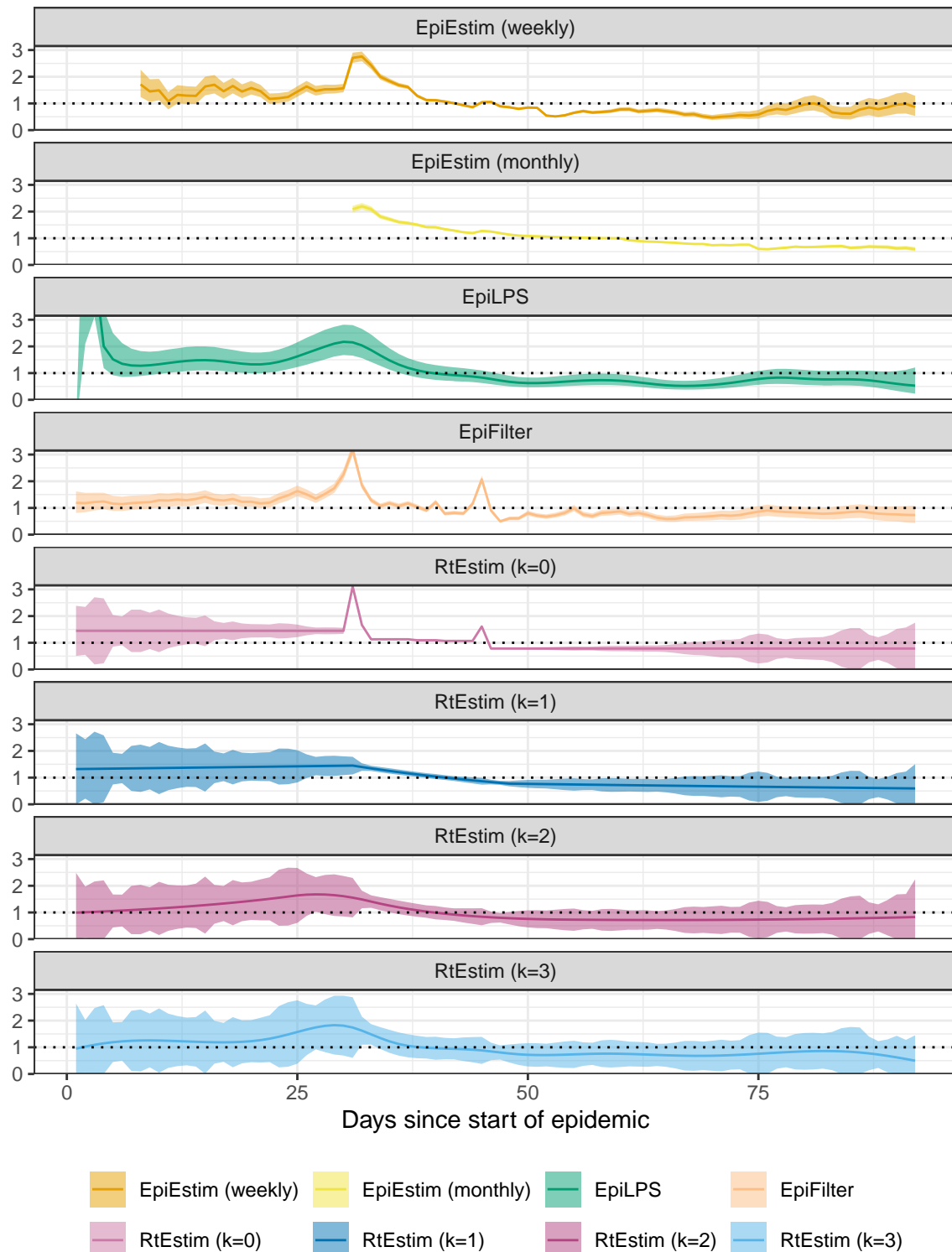


Figure A.8.2: Rt estimates for Covid19.


Figure A.8.3: R_t estimates with CIs for Flu 1918.

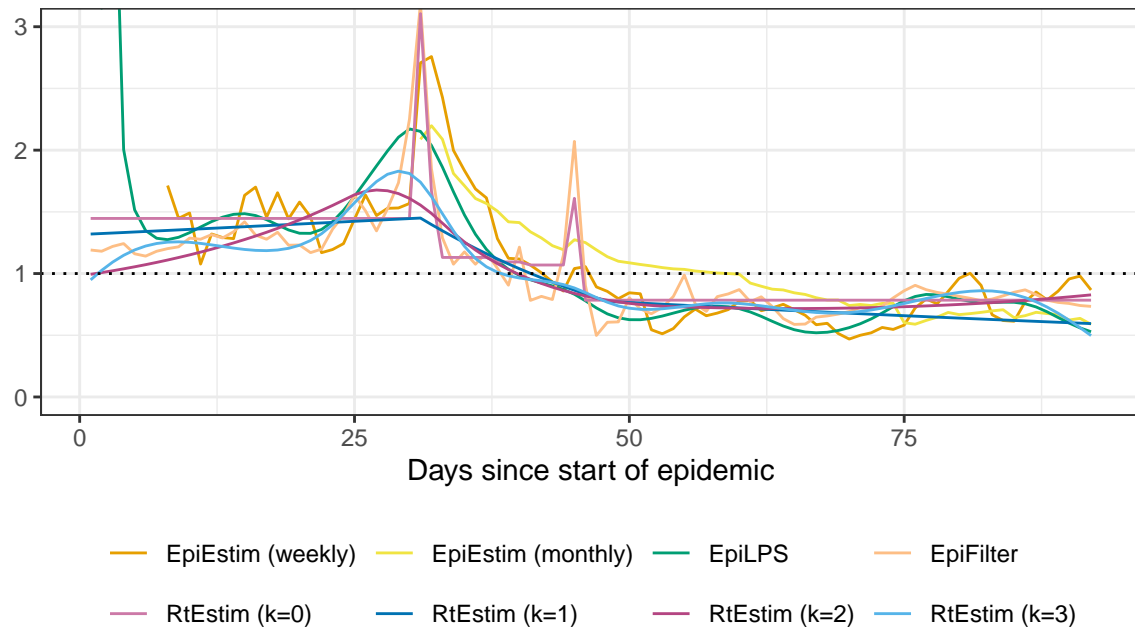


Figure A.8.4: R_t estimates for Flu 1918.